The Henryk Niewodniczański
Institute of Nuclear Physics
Polish Academy of Sciences
in Krakow, Poland

Doctoral dissertation

Application of Monte Carlo methods in transport modelling of the therapeutic proton beam

Magdalena Kłodowska

Supervisor:
prof. dr hab. Paweł Olko
dr Leszek Grzanka

Krakow 2018

It is not enough to be busy. So are the ants.
The question is: What are we busy about?

Henry David Thoreau

Acknowledgements

This work was made possible with help of many people who I would like to cordially thank. Especially I would like to acknowledge the following persons:

prof. Paweł Olko for his constant and valuable support on the scientific path;

Leszek Grzanka, PhD, for his supervision in all-about Monte Carlo world issues;

whole CCB team, especially members of PDKJ, PTO and PPL units for sharing the data and their dosimetric knowledge crucial for Monte Carlo beam model validation;

Katarzyna Krzempek, **Małgotrzata Liszka** and **Natalia Mojżeszek, PhD,** for endless stimulating discussions on protons.

I would also like to thank for the financial support from Marian Smoluchowski Scientific Consortium KNOW.

This research was supported in part by PL-Grid Infrastructure.

Contents

List of acronyms

BP	Bragg peak
BPC	Bragg Peak Chamber
BPM	Beam Profile Monitor
CCU	Common Control Unit
CT	Computed Tomography
CSDA	continuous-slowing-down approximation
DDD	Depth-Dose Distribution
DFO	distal fall-off
ELTR	eye-line treatment room of CCB
ESS	energy selection system
FWHM	full-width at half-maximum
GTR	gantry treatment room of CCB
IAEA	International Atomic Energy Agency
IBA	Ion Beam Applications, Inc.
IC	ionisation chamber
ICRU	International Commission on Radiation Units and Measurements, Inc.
IDD	Integral Depth-Dose
IFJ PAN	Institute of Nuclear Physics Polish Academy of Sciences
IGE	Ion Guide End
LET	Linear Energy Transfer
MC	Monte Carlo
MCS	multiple Coulomb scattering
MU	monitor unit
PBS	Pencil Beam Scanning
PDD	Percent Depth-Dose
PDKJ	Pracownia Dozymetrii i Kontroli Jakości (*Engl.* Dosimetry and Quality Control Unit)
PET	Positron Emission Tomography
PPL	Pracownia Planowania Leczenia (*Engl.* Treatment Planning Unit)
PT	proton radiotherapy
PTO	Pracownia Terapii Oka (*Engl.* Eye Therapy Unit)
QA	Quality Assurance
RBE	relative biological effectiveness
RM	range modulator
RS	range shifter
SD	standard deviation
SOBP	spread-out Bragg peak
TLD	thermoluminescence detector
TPS	Treatment Planning System
WER	Water Equivalent Ratio
WET	Water Equivalent Thickness

Streszczenie

Korzystny rozkład dawki cechujący terapię jonową spowodował wzrost liczby centrów terapii hadronowej, głównie protonowych. Techniki z użyciem wiązek protonowych wymagają bardziej zaawansowanych procedur zapewnienia jakości w zakresie dozymetrii i planowania leczenia. Dlatego zastosowanie metod Monte Carlo (MC) stało się nieodłącznym standardem stosowanym w ośrodkach terapii protonowej jako równoległe narzędzie, cechujące się wysoką precyzją i szerokim wachlarzem zastosowań.

W Centrum Cyklotronowym Bronowice (CCB), wyposażonym w nowy cyklotron Proteus C-235, oddano do użytku stanowisko z wiązką poziomą dedykowane do radioterapii protonowej czerniaka gałki ocznej (*ang.* ELTR) i dwa pomieszczenia z obracanym ramieniem tzw. stanowiska gantry (*ang.* GTR) do napromieniania guzów o innej lokalizacji. Celem pracy było zbudowanie komputerowych modeli wiązki stanowisk ELTR i GTR, przydatnych we wdrażanniu stanowisk w procesie leczenia. Zadaniem modelu wiązki ELTR była optymalizacja układu pasywnego rozpraszania wiązki spełniającego kliniczne wymogi napromieniań pacjentów z nowotworami gałki ocznej. Celem skonstruowania modelu wiązki GTR było uzyskanie poprawek do mierzonych rozkładów dawki, potrzebnych do właściwego skonfigurowania i weryfikacji systemu planowania leczenia (*ang.* TPS commissioning).

Modele wiązki ELTR i GTR zostały przygotowane w kodzie MC FLUKA służącym do obliczeń transportu cząstek. Symulacje były uruchamiane na klastrach obliczeniowych dostępnych w Infrastrukturze PL-Grid. Weryfikacja charakterystycznych parametrów wiązki: zasięgu wiązki, szerokości dystalnego spadku dawki, szerkości połówkowej piku Bragga, stosunku dawki maksymalnej do wlotowej czy poprzecznych rozmiarów wiązki ołówkowej (śladu wiązki *ang.* spot) prowadzona była w oparciu o zmierzone rozkłady dawki głębokiej i poprzeczne profile wiązki protonowej.

Wykorzystując model ELTR, analizie poddano układy formowania wiązki złożone z folii tantalowych jako rozpraszaczy o zmiennej grubości i promieniu. Z 87 przeanalizowanych układów, wybrano optymalne trzy spełniające kliniczne wymogi wiązki rozproszonej dotyczące szerokości półcieni, płaskości poprzecznej pola i szerokości poprzecznej pola. Układy te to: układ z pojedynczą folią 60 μm *Ta*, układ z dwiema foliami 25 μm i 60 μm *Ta* oraz układ podwójnego pierścienia (*ang.* dual ring) zawierający wewnętrzny dysk *Ta* o promieniu $r = 6$ mm i grubości 80 μm wraz z pierścieniem PMMA o grubości 1 mm. Układ podwójnego rozpraszania cechowała dawka do 28%

wyższa w porównianiu do pozostałych dwóch układów pojedynczego rozpraszania, i o 33% wyższa od obecnego systemu pojedynczego rozpraszania w ELTR.

By uwzględnić wkład do rozkładu dawki wynikający z dalekozasięgowych reakcji jądrowych wiązki protonowej w ośrodku na stanowisku gantry, zasymulowany został detektor o promieniu $r = 20\ cm$, umożliwiający obliczenie scałkowanego rozkładu dawki głębokiej (*ang.* Integral Depth-Dose distribution, IDD) z wykorzystaniem skonstruowanego modelu wiązki GTR. Obliczone krzywe IDD pozwoliły na korekcję danych pomiarowych zmierzonych komorą Bragga (*ang.* Bragg Peak Chamber), sięgające 8.8% dla najwyższej energii wiązki 226.08 MeV. Wyliczone krzywe IDD zostały wzięte jako dane wsadowe wymagane do skonfigurowania systemu planowania leczenia Eclipse ver. 13.6. Od 2016, model wiązki w systemie planowania leczenia Eclipse, uzyskany w oparciu o skorygowane rozkłady dawki jest wykorzystywany do przygotowania planów pacjentów w CCB.

Kod MC FLUKA okazał się przydatnym narzędziem do modelowania transportu terapeutycznych wiązek protonowych w CCB. Analiza poprzecznych i głębokościowych rozkładów dawki pozwoliła na wyselekcjonowanie kluczowych parametrów wiązki, koniecznych do weryfikacji obu komputerowych modeli wiązek. W przypadku ELTR, zastosowanie metod MC przy optymalizacji układu rozpraszania pozwoliło na ograniczenie prac ekperymentalnych. W przypadku uzyskanego modelu wiązki GTR, użycie metod MC umożliwiło pokonanie ograniczeń związanych z rozmiarem detektora, w efekcie owocując poprawkami rozkładów dawki o wysokiej precyzji, umożliwiającymi dokładniejsze planowanie terapii. Załączone przykładowe pliki kodu FLUKA z uproszczonymi modelami wiązek dla ELTR i GTR, wraz z podanymi parametrami modelu wiązki GTR3 pozwalają na podjęcie symulacji wykorzystujących wiązki protonowe CCB np. przy planowaniu eksperymentów z dziedziny fizyki medycznej czy radiobiologii.

Abstract

Favourable dose distribution in light ion therapy has led to a growing number of hadron therapy facilities, mainly proton sites. While the usage of proton beams requires more complex quality assurance procedures in terms of dosimetry and treatment planning, application of the Monte Carlo (MC) methods has become an inherent standard of proton facilities as a complementary, high-precision and multi-purpose dosimetry tool.

At the Cyclotron Centre Bronowice (CCB) with a new cyclotron Protecus C-235 three treatment rooms have been developed for proton radiotherapy: one with a horizontal line for eye melanoma treatments (ELTR) and two gantry rooms (GTRs) with a rotating beam for other tumour sites. The aim of this work was to develop beam models for each beam line separately. The role of the ELTR beam model was to optimise the passive scattering system to fulfil clinical requirements concerning eye melanoma patient irradiation. The GTR beam model was developed to derive corrections of the dose distribution resulting from the limited size of the Bragg Peak Chamber (BPC). Calculation of the corrected dose distribution was needed for the proper commissioning of the treatment planning system (TPS).

The ELTR and GTR beam models were developed with the FLUKA particle transport MC code and simulations were run on clusters available within the PL-Grid Infrastructure. Measured depth-dose distributions and lateral dose profiles of the proton beam were used as a reference for the verification of the characteristic beam parameters: beam range, dose distal fall-off, Bragg peak width, maximum to entrance dose ratio and lateral spot size.

The ELTR beam model was applied to optimise the beam forming elements, with tantalum foils defined as scatterers with variable scatterer thickness and radius. From 87 analysed set-ups, the final three were selected fulfilling clinical requirements of the scattered beam parameters lateral penumbrae, lateral field flatness and lateral field width. These were: a single foil of 60 μm Ta, two foils of 25 μm and 60 μm Ta and a dual ring of $r = 6$ mm 80 μm Ta disk with 1 mm PMMA ring. The double scattering geometry resulted in up to 28% higher dose at the isocentre with reference to the remaining two single scattering set-ups, and a 33% higher dose when compared to the single scattering set-up currently applied at the ELTR.

The GTR beam model enabled the calculation of the Integral Depth-Dose (IDD) distribution with a detector radius of $r = 20$ cm, sufficient to account for low-dose envelope surrounding single pencil beam. The maximum obtained dose difference, when compared with the Bragg Peak Chamber measurements, reached 8.8% for 226.08 MeV beam energy. The calculated IDD curves were taken as input in the commissioning

of the Eclipse ver. 13.6 TPS. Since 2016 the TPS is used for treatment planning at CCB.

The FLUKA MC code was found useful for proton transport modelling of the CCB therapeutic beams. Lateral and depth-dose distribution analysis allowed the selection of the crucial beam parameters required for MC beam model verification. In the case of ELTR, the MC modelling facilitated scattering system optimisation, saving beam-time and man power. The GTR MC-based beam model enabled detector size limitations to be overcome, delivering corrections of the dose distributions for treatment planning. The attached exemplary FLUKA files with a simplified ELTR and GTR beam model, together with the given GTR beam model parameters, allow for free access in simulations with CCB proton beams, *e.g.* in planning new experiments in medical physics and radiobiology.

Introduction

The discovery of X-rays by Wilhelm Röntgen [Röntgen, 1895], radioactivity by Henri Becquerel and radium by Pierre Curie and Maria Skłodowska-Curie in the 1890s rapidly led to the usage of radiation in medical applications. Already in 1896, the first attempts to treat cancer patients with X-rays were undertaken [Grubbé, 1933]. In the following years, the techniques of using ionising radiation to treat malign and benign tissues were developed based on the experience gained from the observations on the radiation effects in biological tissues.

Depending on the radiation quality, different depth-dose distributions (DDDs) are observed. **Figure I.1** shows schematically the depth-dose distributions of photons, protons and carbon ions in water - a medium considered as a good dosimetric approximation of a biological tissue. Megavoltage X-rays interacting with the medium produce electrons, thus in the entrance region a dose raise is observed before reaching secondary electron equilibrium. The character of MV X-ray interactions is favourable for skin sparing, however is followed by a non-zero dose at even larger depths (*i.e.* the exit dose behind the tumour). For heavy charged particles such as protons and heavy ions, the lower their kinetic energy the higher is the cross section for interactions with matter and thus for energy transfer to the surrounding matter. This is valid for energies higher than about 0.25 MeV/u. These particles demonstrate enhanced energy deposition just before they stop, a so-called Bragg peak (BP) [Bragg and Kleeman, 1905]. This peak distinguishes hadron radiotherapy from conventional photon techniques and is applied by the adjustment of the beam energy to deposit a maximal dose within the tumour region, with almost a zero dose for healthy tissues localised behind it. For protons the BP is followed only by a negligible neutron dose [Schneider et al., 2002], whereas for particles heavier than protons also a dose "tail" from the ion fragmentation is observed (cf. **Figure I.1**).

The continuous development of radiotherapy techniques has been aimed at lowering the dose to healthy tissues while preserving the tumour dose. Alternatively, the target dose could be enhanced to reach higher local control. In 1946, Robert Wilson proposed the usage of proton beams in radiotherapy, which was soon applied in the Lawrence Berkeley Laboratory to treat experimental animals, followed by patients [Wilson, 1946] [Tobias et al., 1952]. For conformal dose coverage of the whole tumour region, a so-called spread-out Bragg peak (SOBP) is formed from the superposition of several Bragg peaks modulated in depth (change of the beam energy) and

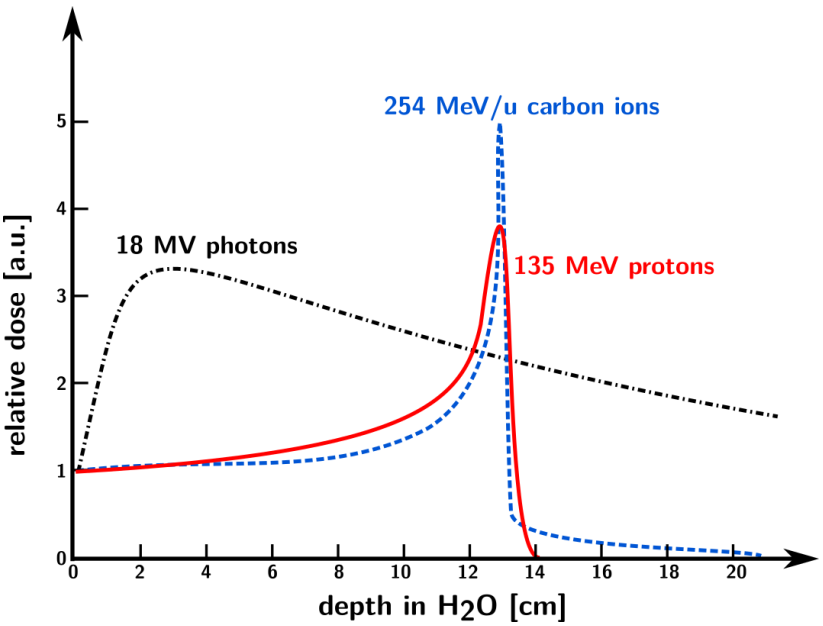

Figure I.1. Depth-dose distributions for various particle type: photons of 18 MV, protons of 135 MeV and carbon ions of 254 MeV/u.
Scheme based on [Haettner, 2006].

with variable weight (modulation of the beam fluence), as schematically presented in **Figure I.2**. Proton therapy demonstrates better conformation of the tumour dose and lower integral dose to the healthy tissues, as shown by [Suit et al., 2010]. PT evolved with the expansion of computers, raising the treatment to submillimetric precision by accurate diagnostic data, advanced treatment planning and customised dosimetry devices preceding precise beam delivery. Together with the development of intensity modulated photon radiotherapy, PT joined high-precision radiotherapy techniques. [Lomax, 1999] has shown that PT delivered half of the integral dose needed for the same effect by intensity modulated photon radiotherapy paving the way for the growing number of PT facilities worldwide [`www.ptcog.ch`].

Such submilimetric precision possible in PT requires accurate methods for the verification of the beam parameters. An experimental approach is not always possible due to experimental limitations, including time and funds. The usage of Monte Carlo methods has become an important tool for growing number of applications, especially in particle therapy where inhomogeneous media play a significant role. Nowadays Monte Carlo methods are used to design and optimise the beam line and beam modifying devices, to calculate the secondary radiation, for shielding investigation, configuration and validation of the treatment planning systems, as a parallel tool in facility commissioning or for *in situ* delivered dose verification [Sawakuchi et al., 2010a] [Paganetti, 2011].

A starting point of the calculation is a reliable Monte Carlo beam model. Though it is commonly used in every research-based proton facility, methods of its development and steps of its validation are rarely given in literature. Furthermore, depending on

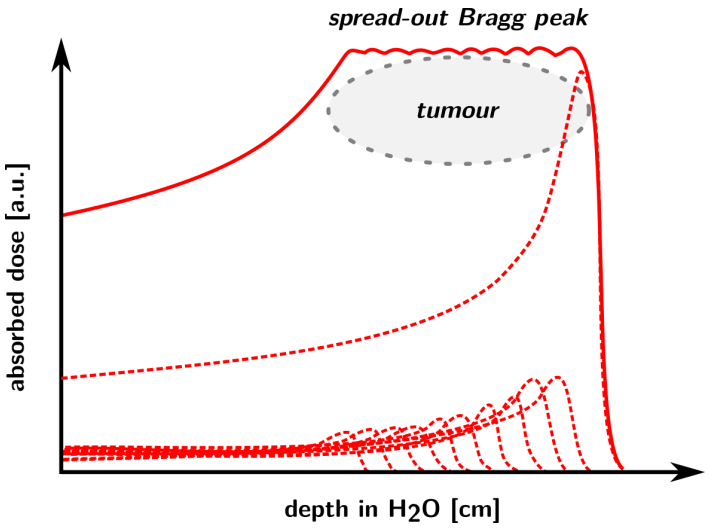

Figure I.2. Scheme of the spread-out Bragg peak (SOBP, solid line) covering the whole target region with homogeneous dose distribution obtained from the contribution of several single Bragg peaks (dotted lines) with adjusted range and weight.

the beam delivery and the beam forming system, development of a MC beam model requires an individual approach.

Aim and scope of work

At the Institute of Nuclear Physics Polish Academy of Sciences (IFJ PAN) cancer patients have been irradiated at the Cyclotron Centre Bronowice (CCB) since 2011 (beam from the AIC-144 cyclotron) and since 2016 with a proton beam produced by Proteus C-235 Proton Therapy system by Ion Beam Applications Inc. (IBA, Louvain-la-Neuve, Belgium). While both passive and active techniques of beam delivery are employed at the CCB, Monte Carlo simulations were applied for the optimisation of horizontal beam line for the eye treatment (ELTR) and for the commissioning of the gantry treatment rooms (GTR) with a rotating beam.

The aims of this work were the following:

- to develop and verify the MC beam model of the ELTR prisitne beam,
- to optimise the scattering system of the ELTR within given clinical constraints with the developed MC beam model of the ELTR,
- to develop and verify the MC beam model of GTR for correction calculation in the commissioning process of the treatment planning system (TPS) for gantry treatment rooms (GTR3, GTR4).

To achieve these goals, the applicability of the FLUKA MC code was evaluated in terms of the underlying physics influencing the protons scattering, range and energy deposition. Next, the available experimental data was analysed to extract a set of beam parameters sufficient for simplified but reliable MC beam model verification, separately for a fixed beam line (ELTR) and rotating beams (GTR). Finally, verified MC beam models were employed for the optimisation of beam forming elements at the ELTR and for the calculations of correction factors for the TPS commissioning.

Author's contribution

The development of the MC beam model for the pristine ELTR pencil-beam was performed solely by the author. The measurements of the pristine unscattered pencil-beam at ELTR (lateral in-air profiles, dose rate measurements) were performed by the team of Pracownia Terapii Oka (PTO, *Engl.* Eye Therapy Unit) under supervision of Jan Swakoń, PhD, with the author contributing to those measurements. The depth-dose profiles of the pristine pencil-beam were measured by the IBA team during the acceptance tests with PTO team participation.

The simulations of the scattering system set-ups were solely made by the author. For the symmetrised MC beam model validation and comparison with existing scattering system mounted at ELTR, the author received data from the operational tests, measured by PTO group lead by Tomasz Horwacik, PhD. The beam parameters collected between *Feb.* 2016 and *Feb.* 2018 were measured by the PTO team.

For GTR commissioning, the measurement of pencil-beams (including in-air lateral profiles at various distances from the isocentre, depth-dose distributions, beam monitor calibration) were performed by the team of Pracownia Dozymetrii i Kontroli Jakości (PDKJ, *Engl.* Dosimetry and Quality Control Unit) supervised by Liliana Stolarczyk, PhD. The author took part in the commissioning process. The calculation of the integral depth-dose distributions was part of the commissioning process, done by the author. The development of the MC beam model for GTR3 and GTR4 rooms was done solely by the author and validated with the commissioning data measured by PDKJ team.

The author tested the gantry beam scattering in RW3 solid phantom in order to verify the physical models implemented in the FLUKA code. Results of 2D TLD measurements in RW3 solid phantom, performed by Jan Gajewski, PhD, were used by the author for the code benchmarking.

The IDD curves based on the GTR MC beam model were calculated by the author for evaluation of the dose correction factor to Bragg Peak Chamber measurements. These curves were incorporated as part of the input data required to formulate the TPS beam model. The TPS configuration was done by Katarzyna Krzempek from Pracownia Planowania Leczenia (PPL, *Engl.* Treatment Planning Unit). The comparison between two TPS models, MC-based and BPC-based was made by the author.

The measurements of the lateral dose distribution far from the pencil beam axis ("second Gaussian") with TLD detectors were acquired by PDKJ team with the author's participation. Next, the obtained results were merged and symmetrised with previously measured Lynx PT in-air lateral profiles by Dawid Krzempek from PDKJ. The fitting of the second Gaussian component in the TPS beam model was done by the Varian Medical Systems team, and author had access to the obtained weights of the first and second Gaussian components from PPL. These weights were used for double Gaussian (2G) gantry MC beam model analysis, performed solely by the author.

Structure of this thesis

This thesis is organised as follows. In **Chapter 1** the theory of proton interactions with matter together with principal beam properties are described. In **Chapter 2** methods of the proton beam dosimetry are briefly characterised, with principles of MC simulations and FLUKA MC code specification. **Chapter 3** specifies the development of the MC beam model of the ELTR with results of the passive scattering system optimisation. The development of the MC beam model for GTR is outlined in **Chapter 4** with depth-dose correction calculations utilised for TPS beam model proper configuration. A summary of the results obtained and an outlook are given in **Chapter 5**. Detailed FLUKA input files are enclosed in **Appendix A** for ELTR and in **Appendix B** for GTR beam model, respectively. Details of the GTR3 beam model parameters are given in **Appendix C**.

Chapter 1

The physics of proton radiotherapy

This chapter presents proton interactions with matter which are relevant for proton radiotherapy, key dosimetric quantities and main features of the proton beam delivery techniques. The broader and detailed description of the physics of PT is beyond the scope of this work and can be found elsewhere, *e.g.* [Gottschalk, 2011] [Paganetti, 2011].

1.1. Proton interactions with matter

Protons passing the medium interact in several ways with the adjacent atoms: via elastic Coulomb interactions with atomic electrons, via elastic Coulomb interactions with atomic nucleus, via non-elastic nuclear interactions with atom nucleus in which secondary particle is emitted from the nucleus or via Bremsstrahlung. **Table 1.1** reproduced from [Newhauser and Zhang, 2015] describes proton interaction types with ejected particles (so-called *ejectiles*) and selected dosimetric consequences.

In the following subsections, proton interactions contributing to the major energy transfer to the medium will be described. Proton Bremsstrahlung is negligible in therapeutic proton range and will not be discussed here.

1.1.1. Stopping of protons

While traversing the medium, protons ionise and excite tissue atoms via electromagnetic interactions with atomic electrons. The knock-on electrons, consecutively, travel with further collisions and thus all proton energy is lost to the stopping material. This is termed stopping power, with a definition given in **Section 1.2**. As a rule of thumb, proton stopping power S is inversely proportional to its kinetic energy (*i.e.* its velocity v squared):

$$S \propto \frac{1}{v^2}. \tag{1.1}$$

Table 1.1. Characterisation of the proton interaction with matter. Reproduced from [Newhauser and Zhang, 2015]

Interaction type	**Interaction target**	**Principal ejectiles**	**Influence on projectile**	**Dosimetric manifestation**
inelastic Coulomb scattering	atomic electrons	primary proton, ionisation electrons	quasi-continuous energy loss	energy loss determines range in patient
elastic Coulomb scattering	atomic nucleus	primary proton, recoil nucleus	change in trajectory	determines lateral penumbra sharpness
non-elastic nuclear reactions	atomic nucleus	secondary protons and heavier ions, neutrons, and gamma rays	removal of primary proton from beam	primary fluence, generation of stray neutrons, generation of prompt gammas for *in vivo* interrogation
Bremsstrahlung	atomic nucleus	primary proton, Bremsstrahlung photon	energy loss, change in trajectory	negligible

Therefore the maximum energy is lost right before protons stop. Due to the nature of the collisions, which are discrete and stochastically fluctuate, even a bench of monoenergetic particles will not stop at the same depth, a quantity which is called *range straggling*. Tabulated values of proton ranges include energy and material dependence, *e.g.* in [Janni, 1982].

Suitable formula for the calculation of mass stopping power $(1/\rho)S_{col}$ offers Bethe theory (derivation can be found in other works mentioned in [ICRU49, 1993]):

$$(1/\rho)S_{col} = -(1/\rho)(dE/dx)_{el} = \frac{4\pi {r_e}^2 mc^2}{\beta^2}\frac{1}{u}\frac{Z}{A}z^2 L(\beta), \tag{1.2}$$

where $r_e = e^2/mc^2$ is the classical electron radius, mc^2 is the electron rest energy, u is the atomic mass unit, β is the particle velocity in units of the velocity of light, Z and A are the atomic number and relative atomic mass of the target atom, and z is the charge number of the projectile.
The quantity L is called the stopping number, expressed in the following terms:

$$L(\beta) = L_0(\beta) + zL_1(\beta) + z^2 L_2(\beta). \tag{1.3}$$

First term is given by:

$$L_0(\beta) = \frac{1}{2}\ln\left(\frac{2mc^2\beta^2 W_m}{1-\beta^2}\right) - \beta^2 - lnI - C/Z - \delta/2, \tag{1.4}$$

where I is the mean excitation energy of the medium, C/Z is the shell correction, and $\delta/2$ the density-effect correction term.
W_m is the largest energy loss in a single collision with a free electron:

$$W_m = \frac{2mc^2\beta^2}{1-\beta^2} \cdot \left[1 + 2(m/M)(1-\beta^2)^{-1/2} + (m/M)^2\right]^{-1}, \tag{1.5}$$

where m/M is the ratio of the electron mass to the mass of the incident particle and mc^2 is the electron rest energy ($0.511\ MeV$). The term in square brackets of **Equation 1.5** is nearly unity and other above-mentioned corrections are negligible for the therapy range of beam energies $3 \div 250\ MeV$, which corresponds to 0.14 and 37.4 cm range in water, respectively (calculated from *PSTAR* database, by NIST [Berger et al., 2009]). For this energy interval Barkas correction (zL_1) and Bloch correction (z^2L_2), together with shell and density effect correction are negligible, and nuclear stopping power S_{nuc} makes only a small contribution (about 1%) to the total stopping power, S [Gottschalk, 2011].

Mean excitation energy I is partially taken from the available experimental data and partially interpolated for other materials where the data is missing. The uncertainties of I value have a significant impact on the range calculation. This is discussed in **Chapter 2.3.4**.

1.1.2. Nuclear interactions of protons

When a proton interacts via nonelastic or inelastic collision with the atom nucleus, it may knock out secondary protons, neutrons, deuterons, α-particles, γ-rays or light recoiling residual nucleons. Most of the kinetic energy of the incident proton is carried away by secondary protons, neutrons and photons, with a rather negligible input from heavier fragments. The probability of the nonelastic interactions for protons in water is presented in **Figure 1.1**.

Some secondaries produced upstream of the beam are scattered under large-angles so they clear out before entering the volume of interest for geometric reasons [Gottschalk, 2011]. Those light fragments which are produced within the irradiated volume feature a short range, deposit their energy in the beam proximity. Some of them, as β^+-emitters, can be used for *in vivo* proton dosimetry [Parodi and Enghardt, 2000] and range verification of the proton beam.

1.1.3. Scattering of protons

As protons are slowed down in the medium, they frequently interact through the Coulomb force with electrons and atom nuclei. The scattering occurs mainly on the atom nucleus rather on electrons due to the large mass difference. This leads to the large number of small angle deflections known as *multiple Coulomb scattering* (MCS).

From the Central Limit Theorem the angular distribution being the quadratic sum of small angular scatterings of protons approaches Gaussian distribution while the number of scatterings increases. Taking into account the electromagnetic scatterings on the nucleus, the theory was developed by Molière [Molière, 1947] and [Molière, 1948] describing calculation of a characteristic multiple scattering angle θ_M and developed further by Fano by adding the correction for scattering by atomic electrons [Fano,

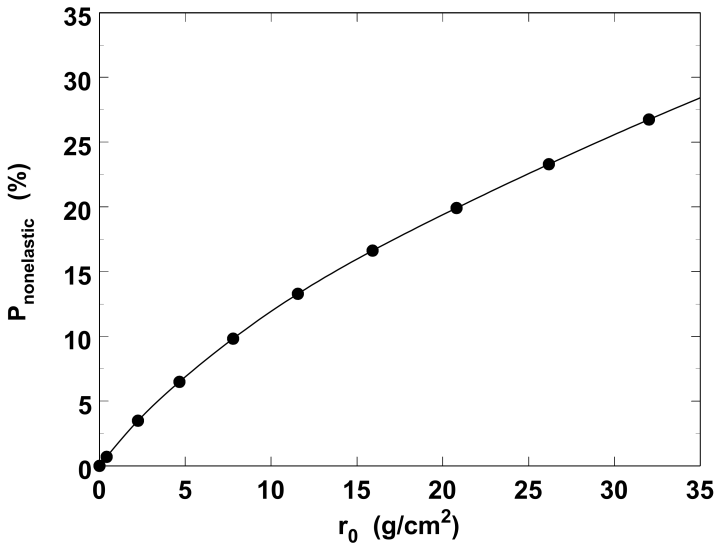

Figure 1.1. Probability of nonelastic interactions for various proton ranges in water. Reprinted from [Gottschalk, 2011].

1954]. The related formulas and others numerical approximations are reviewed by [Gottschalk et al., 1993].

The dependence of the stopping power and the scattering power (ratio between mean square scattering angle per unit thickness of an absorber traversed by the charge particle) on the atomic number Z is the basis of the material choice for the beam shaping. High-Z materials, such as lead or brass, are used for the beam scattering while minimising the energy losses, whereas low-Z materials like water, Lexan or beryllium degrade the beam (shorten its range) with reduced angular scattering (**Figure 1.2**).

The dependence of the scattering angle on the inverse power of the proton kinetic energy explains the broadening of the proton beam near the end of the range. For single narrow pencil beams (*e.g.* of 10 *mm* diameter) it leads to the vanishing of the Bragg peak as the lateral scattering equilibrium is not preserved and the number of protons deflected from the beam axis is not compensated by the number of protons scattered towards the beam axis as in the case of a broad beam [Vatnitsky et al., 1999]. For such beams, the concept of proton mini- and micro-beam therapy was developed [Prezado and Fois, 2013]. It is postulated that a very high dose can be delivered in narrow spatially spaced beams with enhanced tolerance of the healthy tissue.

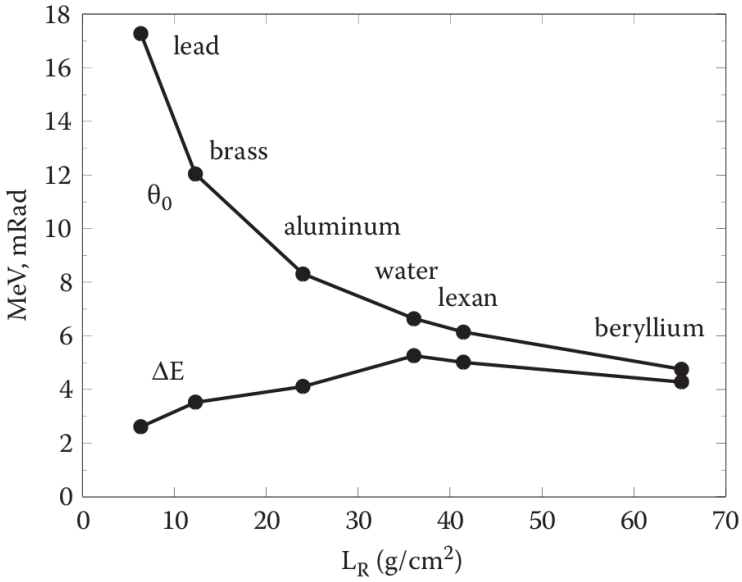

Figure 1.2. Energy loss (ΔE $[MeV]$) and multiple scattering angle (θ_0 $[mRad]$) for 160 MeV proton beam traversing 1 g/cm^2 of materials with different radiation length (L_R). Reprinted from [Paganetti, 2011]; based on data from [ICRU49, 1993].

1.2. Quantities describing a proton beam

Mass stopping power

Stopping power S is used to describe proton energy loss dE per given distance dx along the proton path:

$$S \equiv -\frac{dE}{dx} \quad \left[\frac{MeV}{cm}\right], \tag{1.6}$$

As the energy loss is negative - energy loss increases down the beam path - stopping power is positive. More often *mass stopping power* is used, including absorber density ρ $[g/cm^3]$:

$$\frac{S}{\rho} \equiv -\frac{1}{\rho}\frac{dE}{dx} \quad \left[\frac{MeV}{g/cm^2}\right]. \tag{1.7}$$

Figure 1.3 shows the total stopping power of protons in water medium plotted from *PSTAR* database, by NIST [Berger et al., 2009].
The *linear energy transfer* (LET) is under some conditions equal to S [Gottschalk, 2011].

Fluence and fluence rate

The proton fluence Φ is defined as the ratio between number of protons (dN) traversing a sphere of cross-sectional area (dA) centred at the point of interest [Attix,

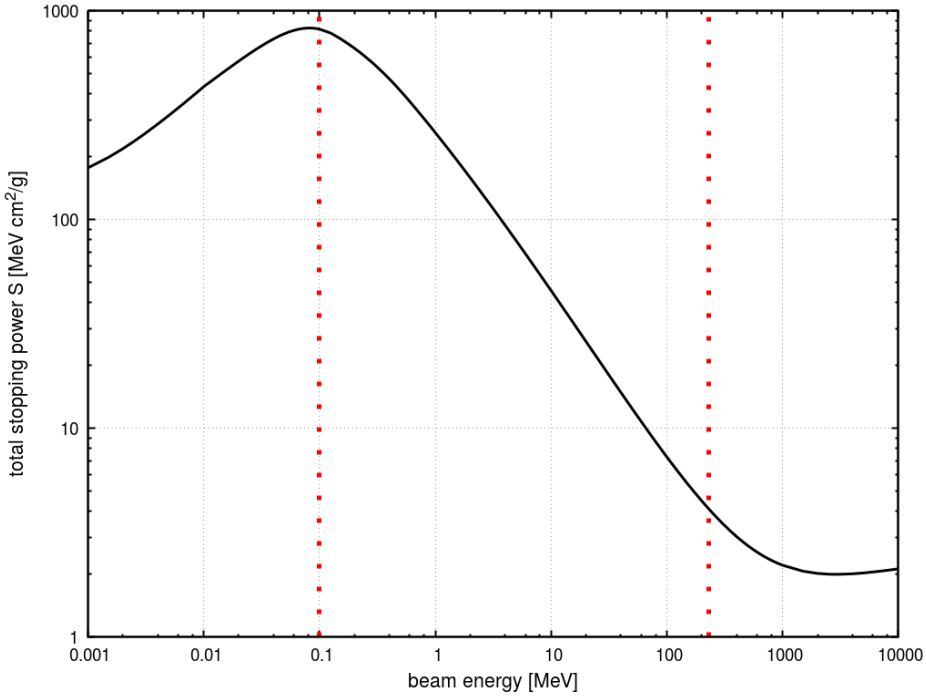

Figure 1.3. Total stopping power for protons in water depending on the proton beam energy. With red dotted lines therapeutic proton energy range of $0.1 \div 230\ MeV$ is marked. Data from *PSTAR* database, by NIST [Berger et al., 2009].

1986]:

$$\Phi \equiv \frac{dN}{dA} \quad \left[\frac{protons}{cm^2}\right]. \tag{1.8}$$

In this work only parallel pencil-beams will be considered, thus area dA will be a plane perpendicular to the beam.

Flux density or fluence rate $\dot{\Phi}$ is expressed by fluence change $d\Phi$ in time dt:

$$\dot{\Phi} \equiv \frac{d\Phi}{dt} \quad \left[\frac{protons}{cm^2\ s}\right]. \tag{1.9}$$

Dose and dose rate

The absorbed dose D at the point of interest is the ratio between the energy dE deposited in the given unit mass dm:

$$D \equiv \frac{dE}{dm} \quad \left[\frac{J}{kg}\right], \tag{1.10}$$

where gray, $1\ Gy \equiv 1\ J/kg$, is basic unit used in clinical dosimetry. Other units, as cGy or rad ($1\ rad \equiv 1\ cGy = 0.01\ Gy$) will not be used in this work.

Absorbed dose rate $\dot{D}$ is the dose delivered in the period of time dt:

$$\dot{D} \equiv \frac{dD}{dt} \quad \left[\frac{J}{kg\ s}\right] = \left[\frac{Gy}{s}\right]. \tag{1.11}$$

In this work, in the calculations performed for passive beam scattering system of the eye melanoma treatment room described in **Chapter 3**, dose rate is assumed to be constant. Dose rate is proportional to the proton beam current. For the proton beam of 1 nA number of protons per second can be calculated:

$$\begin{aligned} 1 \quad [nA] &= 10^{-9} \quad \left[\frac{C}{s}\right] \\ 1 \quad [e] &= 1.602 \cdot 10^{-19} \quad [C] \\ 1 \quad [nA] &= 6.24 \cdot 10^{9} \quad [protons/s] \end{aligned} \tag{1.12}$$

Taking beam energy of 70 MeV with $S^{total}_{H_2O} = 9.559\ MeV\ cm^2/g$ entering a water phantom ($\rho = 1\ g/cm^3$) with N protons impinging on area A with thickness of Δx we can calculate dose rate value of 1 nA proton beam of energy 70 MeV $\dot{D}(H_2O, 70\ MeV, 1\ nA)$:

$$D \equiv \frac{dE}{dm} = \frac{dE/dx \cdot \Delta x \cdot N}{\rho \cdot \Delta x \cdot A} = \Phi \frac{S}{\rho} \quad \left[\frac{protons}{cm^2}\frac{MeV}{g/cm^2}\right] \tag{1.13}$$

$$\dot{D}(H_2O, 70\ MeV, 1\ nA) = 9.559 \left[\frac{MeV}{g/cm^2}\right] \cdot 0.1602 \cdot 10^{-12} \left[\frac{J}{MeV}\right] \cdot 6.24 \cdot 10^{9} \left[\frac{protons}{cm^2\ s}\right]$$

$$\dot{D}(H_2O, 70\ MeV, 1\ nA) = 9.56 \left[\frac{Gy}{s}\right]$$

In the above calculations, no energy or fluence loss as a result of beam transport have been taken into account. In the cyclotron-based proton facilities, the beam is extracted from the cyclotron with maximum available energy and then degraded mechanically down to the demanded energy. This process leads to the beam current decrease. The beam line transmission efficiency defined as the ratio between the beam current from the cyclotron to the beam current entering the treatment room, goes down to a few percent (below 5%) for energies below 100 MeV. Assuming 2% of the transmission efficiency for the 70 MeV proton beam, dose rate of $\dot{D}^{room}(H_2O, 70\ MeV, 1\ nA) = 11.4\ Gy/min$ is obtained, a value comparable with experimental data at AIC-cyclotron eye melanoma treatment room [Swakon et al., 2010].

For passive beam scattering technique, considered in **Chapter 3**, dose rate is a required parameter constraint to be fulfilled. While from MC simulations dose rate value cannot be obtained directly, the MC results were recalculated for dose in water for 1 nA beam current $D(1\ nA)$.

For the active scanning technique, dose rate varies from spot to spot. Additionally, in the pencil beam scanning (PBS) technique available at the gantry rooms of CCB, dose is delivered in *step-and-shoot* mode. Therefore, results of the simulations devoted to the active scanning beam of the CCB gantry rooms, described in **Chapter 4**, will be presented solely in terms of the absorbed dose D.

Areal density

It is a common practice to express absorber thickness not as Δx (cm) but in terms of areal density:

$$\rho \cdot \Delta x \quad (g/cm^2), \tag{1.14}$$

where ρ (g/cm^3) is the absorber density. Such definition eases the understanding of underlying trends in stopping power and scattering power of a given material.

Beam energy

Beam energy for therapeutic purposes is typically expressed in MeV. The relation between MeV and J is as follows:

$$1\ MeV = 1.602 \cdot 10^{-13}\ J \tag{1.15}$$

Water equivalence

A water equivalent absorber means material featuring the same energy loss as in a water layer. Thus we can derive *water equivalent thickness* $WET[cm]$ of a given material M [Gottschalk, 2011]:

$$\begin{aligned} S_M(T)\rho_M\Delta x_M &= S_{H_2O}(T)\rho_{H_2O}\Delta x_{H_2O} \\ WET_M = \Delta x_M &= \frac{S_{H_2O}}{S_M}\frac{\rho_{H_2O}}{\rho_M}\Delta x_{H_2O}, \end{aligned} \tag{1.16}$$

for T being particle kinetic energy and Δx being the absorbers thickness. The ratio between two material thicknesses enables fast comparison of the scattering/degrading effects between the absorbers, noted as *water equivalent ratio* (WER). This is not, however, always true for clinical ranges. As shown in **Figure 1.4** reprinted from [Gottschalk, 2011] transition between water and Lexan is quite accurate, whereas curves for lead and brass differ in shape comparing to water, leading to discrepancies in the therapeutic energies.

Relative Biological Effectiveness (RBE)

Relative biological effectiveness (RBE) is termed as the ratio between the dose of reference radiation (typically of $Co-60$) to the dose needed to obtain the same biological effect. For hadron beams this value is typically above unity as heavy charged particles cause more damage to biological systems. The clinical RBE-dose (D_{RBE}) is given in $Gy(RBE)$ or sometimes, now obsolete, in Cobalt Gray Equivalent CGE [ICRU78, 2007].

For proton radiotherapy, the accepted and commonly used clinical RBE is 1.1 [ICRU78, 2007], although higher values at the distal part of the SOBP have been reported using different radiobiological models [Paganetti et al., 2002]. As this work is focused on the physical dose calculations, therefore *dose* will refer to the absorbed dose.

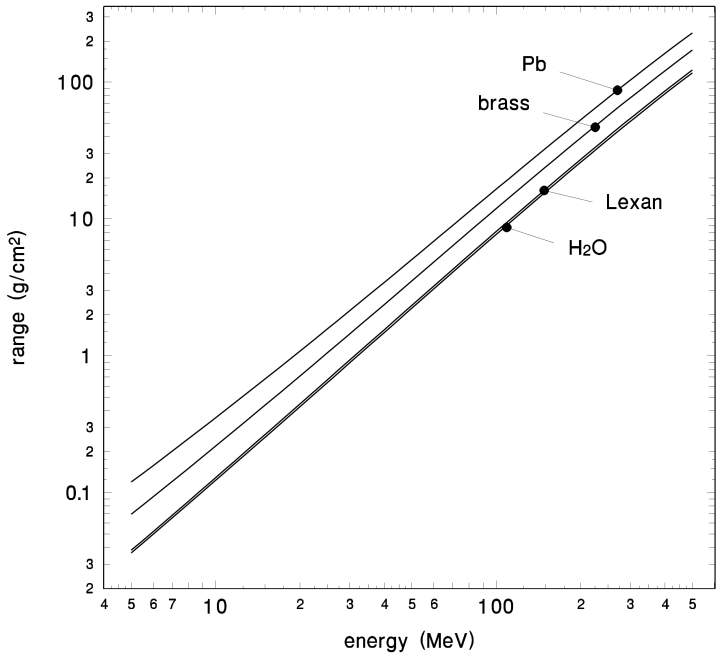

Figure 1.4. Range-energy plot over clinical proton energies for 4 typical materials used in the design of a scattering system. Reprinted from [Gottschalk, 2011].

1.3. Characteristics of the therapeutic proton beam

A proton beam can be specified by the number of characteristic features, related to the beam models used in treatment planning systems and parameters of the beam quality to be verified prior the patient irradiation. Both perspectives will be explained below, referred to as 'beam properties' with reference to the beam characteristics applied in beam modelling and as 'beam parameters' referring to the quantities used for the beam verification, according to [ICRU78, 2007].

1.3.1. Beam properties

The physical characteristics of the beam constitute an input to treatment planning systems. The *beam source* is located before the beam shaping system and is also termed as *virtual source*. A reference point is called the *isocentre*, localised inside the treatment room and required for the integration of all the coordination systems used for the beam delivery, beam monitoring, patient treatment planning and positioning.

The proton beam is characterised by several properties [ICRU78, 2007]:

- beam direction - horizontal beam in fixed beam lines and rotating beam in gantry room,
- beam energy E with beam energy spread dE/E (or beam momentum p with momentum spread dp/p)
- beam angular divergence as the correlation between the mean direction of the particles and the position in the space (θ_x,θ_y),

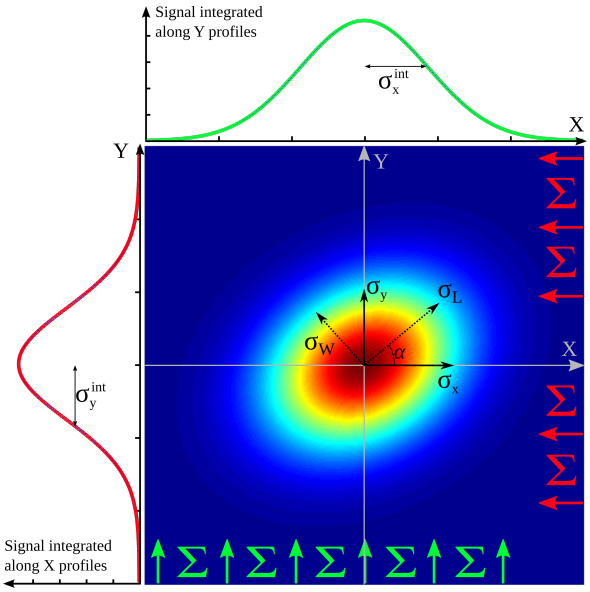

Figure 1.5. Beam spot size can be characterised by its lateral and vertical profiles (σ_x, σ_y), integrated horizontal and vertical profiles (σ_x^{int}, σ_y^{int}) or profiles through the spot major and minor axis (σ_L, σ_W) with spot rotation angle α with reference to the horizontal X axis. Reprinted from [Kłodowska et al., 2016]

- beam angular emittance as the particles distribution around their mean direction (ϵ),
- beam size as the dimensions of the lateral cross-section.

Customarily Gaussian distribution is used to describe beam energy dispersion, its angular or spatial spread, thus main beam properties are given by standard deviation σ or its full-width-at-half-maximum (FWHM) with dependence $FWHM = 2\sigma\sqrt{2ln2}$.

For the pristine (unscattered) and unmodulated pencil-beam, 2D lateral beam cross-section is called a *spot* and can be described by asymmetrical 2D Gaussian distribution [Haberer et al., 2004]. The spot size parameter σ can be obtained in three different ways, as it is schematically shown in **Figure 1.5**:

- σ_x and σ_y derived from horizontal and vertical profiles crossing the spot centre (customarily spot centre of mass),
- σ_x^{int} and σ_y^{int} derived from profiles integrated over either horizontal or vertical direction,
- σ_L and σ_W derived from profiles extracted from major and minor axis of the spot with spot rotation angle α between horizontal X axis and spot major axis.

A comprehensive description of the spot lateral profile analysis can be found in [Gajewski, 2016].

1.3.2. Beam parameters

Beam parameters are retrieved in the quality assurance (QA) procedures and serve as part of the beam quality verification. Depth-dose profiles, acquired along the beam central axis, and lateral profiles, taken in the plane perpendicular to the beam axis,

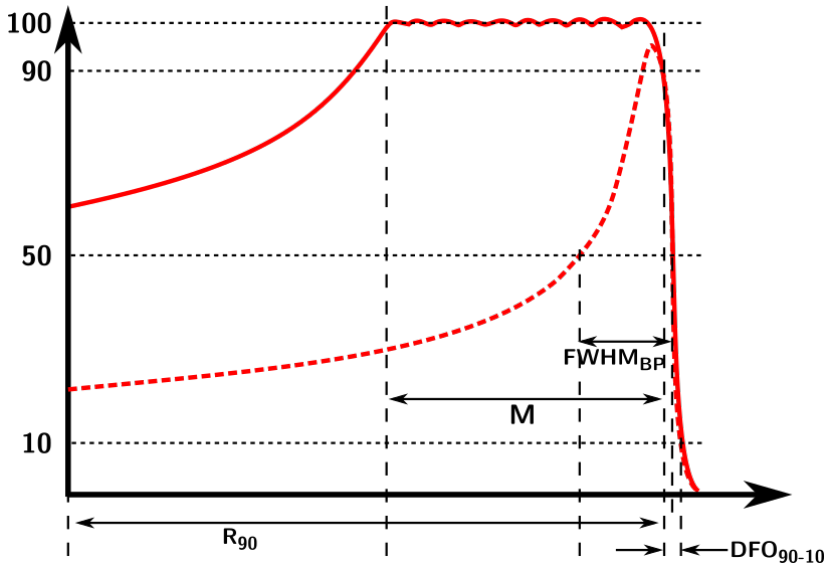

Figure 1.6. Beam parameters for a Percent Depth-Dose distribution of the proton beam for a single Bragg peak and the SOBP: range R (here marked R_{90}), BP width $FWHM_{BP}$, distal fall-off (here marked between 90% and 10%) and SOBP modulation width M (marked between proximal 99% and distal 90% level).
Based on [ICRU78, 2007].

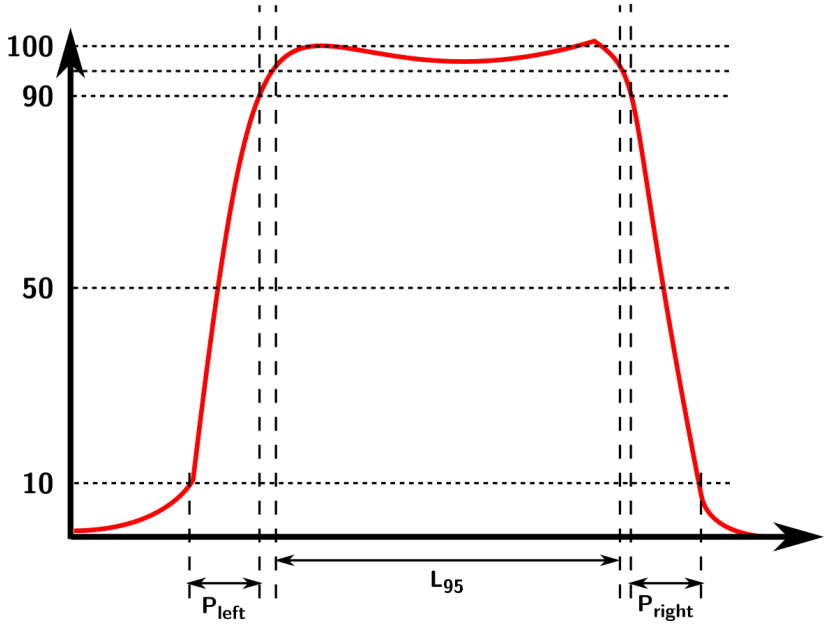

Figure 1.7. Beam parameters for a lateral dose distribution of the proton beam: penumbrae P_{left}, P_{right} (here marked between 90% and 10%) and field width L (here as width between 95% levels). Based on [ICRU78, 2007].

are parametrised, as presented in **Figure 1.6** and **Figure 1.7** with the following definitions [ICRU78, 2007]:

- **Depth-Dose Distribution,** DDD
  Depth-Dose Distribution (DDD) corresponds to the absorbed dose distribution in a medium, typically in water, measured along the beam axis. When the curve is normalised to the maximum dose value at the Bragg peak depth, it is called Percent Depth-Dose (PDD) distribution. For the measurements of single pencil-beams with parallel-plate ionisation chamber with large diameter the DDD is referred as Integral Depth-Dose (IDD) distribution.

- **beam range,** R
  Beam range R $[mm]$ corresponds to 50% of the incident proton fluence. In an alternative definition, a distal of 80% or 90% of the maximum dose value is applied, given in g/cm^2 of depth in medium.
  In this work, the range R_{90} will be used in accordance with measurement procedures given in [CCB Quality Book, 2015].

- **distal fall-off,** DFO
  Distal fall-off (DFO $[mm]$) is the distance between 80% and 20% or between 90% and 10% of the maximum dose after the Bragg peak given in a g/cm^2 in medium. In this work, both DFO_{80-20} and DFO_{90-10} values will be used in accordance with measurement procedures given in [CCB Quality Book, 2015].

- **full-width-at-half-maximum,** $FWHM_{BP}$
  Full-width-at-half-maximum ($FWHM_{BP}$ $[mm]$) for depth-dose distribution of a single BP is measured as the peak width (cm) at the level of 50% of the maximum dose value of DDD.

- **max/plateau ratio**
  The $max/plateau$ ratio is the ratio between the maximum dose and entrance dose calculated for DDD curves of a single BP .

- **modulation,** M
  For SOBP depth profile in water, modulation M $[cm]$ is the distance between distal 90% and proximal 99% of the maximum dose value *i.e.* the region of a uniform high dose.

- **penumbra,** P
  For lateral dose profiles *beam penumbra* P $[mm]$ is calculated as $80\% \div 20\%$ or $90\% \div 10\%$ lateral dose fall-off in reference to the maximum dose value at given depth in medium.
  In this work, P_{90-10} will be be used in accordance with measurement procedures given in [CCB Quality Book, 2015], for symmetrical lateral dose profile it is referred as P_{mean}.

- **lateral field width,** L
  Lateral field width $L[mm]$ is defined as the width between the lateral 50% of the

maximum dose on the isocentre plane in air.
In this work, L will be analysed at the 95% dose level on the lateral dose profile in accordance with measurement procedures given in [CCB Quality Book, 2015], as L_{95} parameter.

- **lateral flatness,** F
  Lateral flatness F [%] of the dose profile in water is defined as:

$$F = \left(\frac{D_{max} - D_{min}}{D_{max} + D_{min}} \right) \cdot 100\%, \tag{1.17}$$

  where d_{max} and d_{min} are maximum and minimum absorbed dose values in the beam profile in the target width.
  For the purpose of this work F will be calculated at the 90% level, F_{90}.

1.4. Techniques of the proton beam delivery

Proton therapy facilities have evolved from nuclear physics laboratories to almost out-of-the-box solutions of commercially available accelerators with dedicated beam lines and several therapeutic rooms to increase patient throughput. In synchrotrons protons are accelerated to the demanded energy, in cyclotrons protons are accelerated to the maximum energy of $200-250\ MeV$ and then slowed down in the energy selection system (ESS) to reach the required range. Several beam forming zones can be distinguished: beam production module with accelerator and ESS, beam-transport system with beam steering magnets and dedicated beam-delivery system for each therapeutic room separately, either with fixed beam or with rotational beam in a so-called gantry treatment room.

Once the beam of desired energy is extracted from the cyclotron, the beam is steered and formed by dipole and quadrupole magnets mounted along the beam line, additionally cut out mechanically by slits inserted into the beam path. The beam is controlled by multi-wire ionisation chambers monitoring its position and shape along the beam line. Detailed description of the beam extraction and tracking can be found elsewhere [Chu et al., 1993] [ICRU78, 2007] [Paganetti, 2011]. For the scope of this work, only the final shape of the beam will be considered in the context of beam-delivery techniques described below and applied in this work.

Most of the dose delivery concepts were designed and developed in pioneering particle therapy centres in Uppsala, Sweden [Larsson, 1962], in Berkeley, California [Pirruccello and Tobias, 1980] [Chu et al., 1993], in Paul-Sherer Institut (PSI), Switzerland [Pedroni et al., 1995] and in Cambridge, Massachusetts [Wilson, 2004]. They are customarily divided into two groups: passive methods with scattering foils inserted into the beam path for the lateral beam broadening, and active scanning methods, sweeping the beam over the target region during the irradiation.

1.4.1. Passive scattering

In the passive beam-delivery technique, dedicated beam modifiers such as plates, foils or rotating propellers are applied to degrade and broaden the beam in order to obtain the uniform dose distribution within the target volume. A dedicated compensator

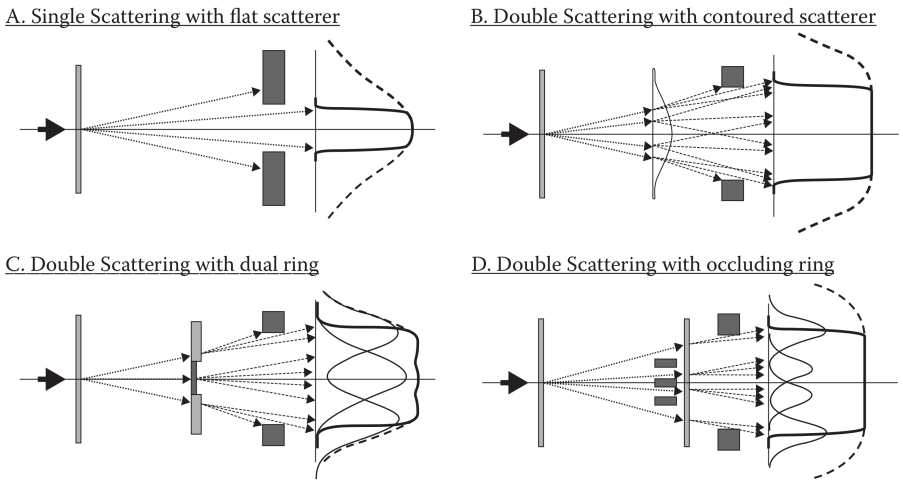

Figure 1.8. Passive methods of beam spreading with single or dual scattering systems. Reprinted from [Paganetti, 2011].

shapes the distal part of the irradiated field, whereas the lateral shape of the beam is modified by the collimators (blocks or apertures) corresponding to the projected target contour. Depending on the site prerequisites and capabilities, each facility has its own scattering system featuring elements of different distance, shape, material and arrangement on the optical bench towards the patient.

The beam can be spread by a single high-Z (lead, tantalum) foil which is called the *single scattering* technique. It requires a relatively long drift distance between the scatterer and patient to assure homogeneous beam cross-section (*cf.* **Figure 1.8 A**). Though the efficiency of such a solution is only a few percent, its simplicity and sharp lateral penumbrae makes this technique advantageous for small field irradiation, such as proton eye treatments [Hérault et al., 2005] [Bonnett et al., 1993] [Daftari et al., 1996] [Michalec et al., 2010] or intracranial radiosurgery [Daartz et al., 2009].

The efficiency of the beam spreading can be enhanced by adding a smaller second scatterer, following the first one and modifying the beam partially, which is called the *double scattering* technique. Three shapes of the second scatterer are distinguished: a dual-ring, an occluding ring and contoured scatterer, as schematically presented in **Figure 1.8 B-D**.

The dual-ring scatterer consists of high-Z central disk (lead, tungsten) with a surrounding ring of light-element material, such as aluminium or PMMA [Takada, 1994], as schematically shown in **Figure 1.8 C**. While both parts are flat with a fixed radius, flat distribution is designed only for a given size, resulting in small fluctuations in the lateral dose distribution due to its binary nature [Paganetti, 2011]. **Figure 1.9** shows total and composing beam distributions produced by dual-ring scatterers. The technique is applied in some eye cancer therapy facilities, *e.g.* in Catania, Italy [Cirrone et al., 2004].

Better flatness of dose distribution can be obtained via the occluding ring technique [Koehler et al., 1977]. Part of the beam is blocked by a high-Z cylinder and the absence of protons in the central part of the beam is complemented by adjacent protons

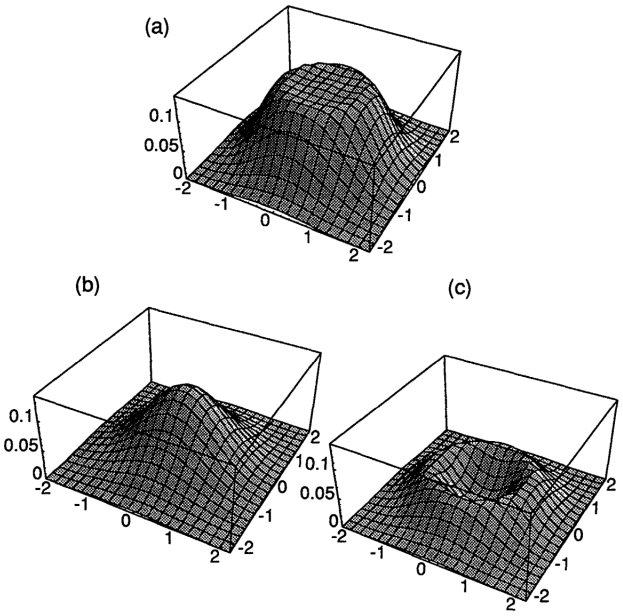

Figure 1.9. Total fluence distribution of the beam (a) formed with the dual-ring double scattering technique with contribution from inner second scatterer (b) and outer second scatterer (c), on the plane perpendicular to the beam axis. Reprinted from [Takada, 1994].

scattered by the second low-Z scatterer (*cf.* **Figure 1.8 D**). For larger field sizes additional occluding rings can be added. This solution, however, features lower beam efficiency while part of the beam is blocked. Nevertheless, it is also used for eye tumour irradiation [Nauraye et al., 1995].

An improved version of the double scattering system uses a contoured second scatterer of high-Z (lead, brass) resembling flattening filter used for beam shaping in linear accelerators for conventional radiotherapy (*cf.* **Figure 1.8 B**). The 2^{nd} scatterer radius and shape are designed numerically to get the flat dose distribution at the isocentre. In order to preserve constant stopping power for the central beam and the scattered peripheral protons, contoured scatterer are accompanied by low-Z counterpart (plastic) of width increasing with the distance from the beam axis [Grusell et al., 1994] [Gottschalk, 2011].

Regardless the choice of the second scatterer, double scattering techniques are sensitive to the beam alignment and phase-space beam distortions. Additional beam monitoring with a feedback mechanism is advisable downstream of the second scatterer [Moyers et al., 1999] [Montelius et al., 1991].

The scattering system is accompanied by patient-specific beam modifiers assuring suitable aperture of the target lateral projection and demanded beam modulation. By stacking several weighted pristine Bragg peaks, SOBP is either accomplished spatially by a so-called *ridge filter* with designed ridge-elevation steps [Kanai et al., 1997] [Akagi et al., 2003] [Hara et al., 2012] or in time with a rotating plastic propeller with steps of calculated width [Wilson, 1946]. The range of the beam is determined by its initial

energy and can be reduced by an absorber called a range shifter (RS). The next element forming the individual beam for the patient is the beam compensator which cuts out additional dose to normal tissues located behind the tumour region.

Passive scattering technique is considered as simpler, safer and less dependent on the time structure of the beam comparing to active methods of the beam spreading [ICRU78, 2007]. However, the delivery of the unwanted extra dose to the adjacent normal tissues preceding the target region along the beam axis is one of the reasons why active scanning methods are considered superior and preferred in some cases [ICRU59, 1998].

1.4.2. Active scanning

The technique of an active beam-delivery system was first developed at GSI, Darmstadt, Germany and applied for carbon ion therapy [Haberer et al., 1993]. The idea of actively scanned beam is to sweep the narrow (a few mm) beam along single energy layer of the target cross-section projection followed by switch to the shallower energy layer until the entire target volume is irradiated, as schematically shown in **Figure 1.10**. The modulation of the beam intensity allows to combineseveral Bragg peaks resulting in the conformal tumour dose distribution. From many methods of such scanning, two are most frequently applied [ICRU78, 2007]:

- **Spot (voxel) scanning**
  This method uses single pencil-beams deposited in grid steps according to spot spacing sufficient to avoid ripples in dose distribution. Single energy-layer is scanned with help of two scanning magnets, bending the beam horizontally and vertically with a position switch while the beam is off.
- **Raster scanning**
  In this technique, a pencil-beam is scanned continuously over the layer with a raster pattern with uninterrupted beam control and variable beam-intensity. The switch between the layers is done with the beam off.

Active beam-delivery techniques enable the reduction of the additional dose, both for distal and proximal part of the tumour volume, concomitantly reducing the number of patient-specific beam modifying devices. It is crucial, however, to assure proper beam shape, alignment and position while the small beam distortion is transmitted through all the spots/layers.

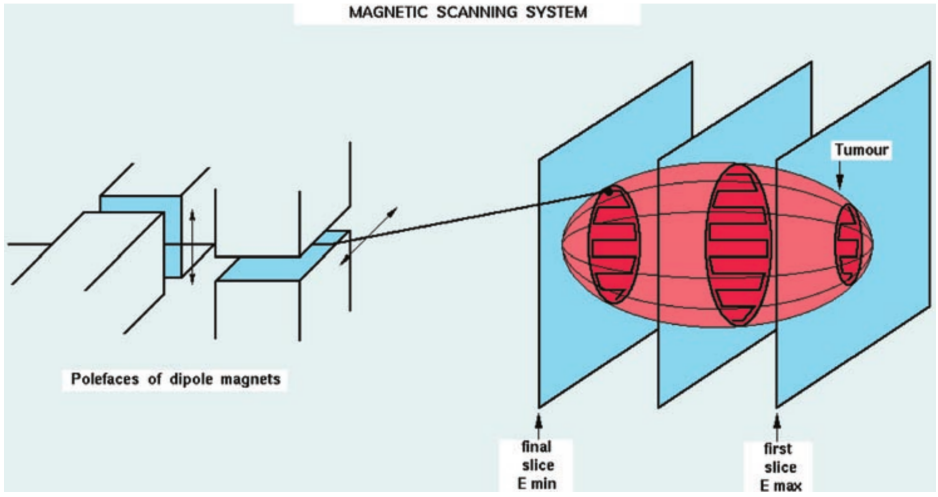

Figure 1.10. Illustration of the magnetic scanning system with pencil-beams enabling to cover the tumour region with conformal dose distribution, starting from the maximum energy (E_{max}) down to minimum required energy of the beam (E_{min}). Reprinted from [Krämer et al., 2000].

1.5. CCB facility

The Cyclotron Centre Bronowice (CCB) was formed in 2012 by combining two cyclotron-based facilities: the 60 MeV AIC-144 isochronous cyclotron [Bakewicz et al., 2003] [Strzałkowski et al., 2006] with an eye treatment room clinically operational since 2011; and Proteus C-235 cyclotron from Ion Beam applications (IBA, Louvain-la-Neuve, Belgium) installed in 2012 at IFJ PAN and put in operation in 2013. Proton eye therapy at the AIC-144 facility was performed between 2011 and 2016. Since 2016, patient treatment is fully performed at the Proteus C-235 clinical system. **Figure 1.11** illustrates the scheme of the CCB beam lines with Proteus C-235 cyclotron, an energy selection system (ESS), beam lines guiding to the experimental room or eye treatment room (ELTR), and to two gantries (GTRs) with rotational beam. Maximum beam current from the cyclotron reaches 500 nA. 106 MHz high frequency generator produces a quasi-continuous proton beam [Gajewski, 2016].

1.5.1. AIC eye melanoma treatment room

One of the first and very successful applications of proton therapy was the treatment of eye lesions. For this type of irradiation, energy of around $60 \div 70$ MeV is sufficient, corresponding to approximatelly $3 - 4$ cm range in water [Gragoudas et al., 1977] [Goitein and Miller, 1983]. Proton therapy in eye lesions, when compared to brachytherapy with isotopes, enables the sparing of critical structures like the optic nerve, fovea, optic disc, lens and ciliary body [Bonnett et al., 1993], thus giving a higher probability of preservation useful visual acuity [Fuss et al., 2001], concomitantly assuring high dose homogeneity within the tumour volume [Appleton and Bridge, 2010].

The patient is usually treated in a seated position, immobilised by a dedicated face mask and a bite block. Tantalum markers sutured around the tumour prior to the

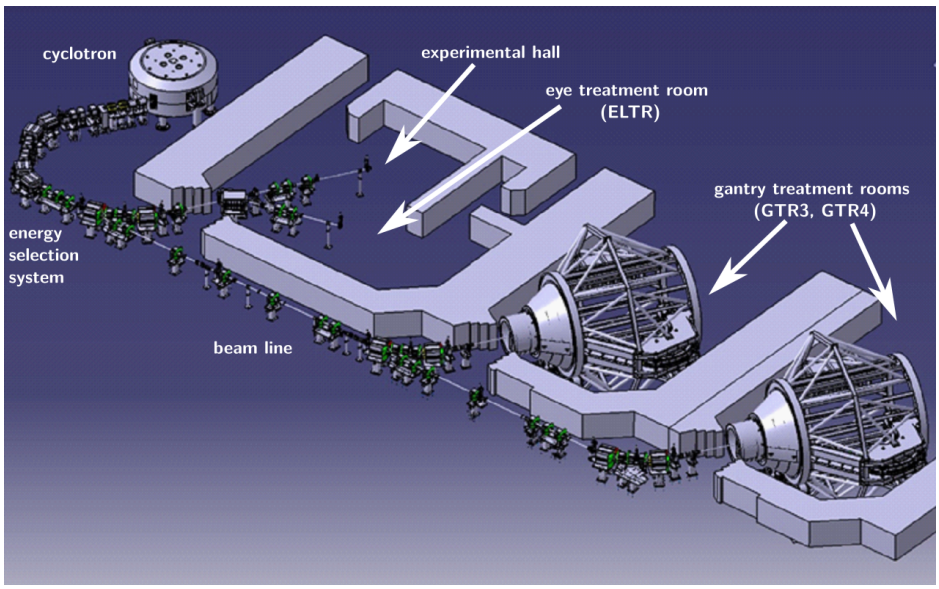

Figure 1.11. Scheme of the Cyclotron Centre Bronowice (CCB) facility at IFJ PAN with cyclotron Proteus C-235 from which the beam is transported to either experimental hall or eye melanoma treatment room (spited fixed horizontal line), or to one of the two gantries (rotational beam line). [Courtesy of IBA]

treatment determine the tumour periphery during the positioning by a sequence of orthogonal X-ray images. First developed at Massachusetts General Hospital and the Harvard Cyclotron Laboratory [Gragoudas et al., 1977] [Goitein and Miller, 1983], eye melanoma treatments at the IFJ PAN are among 16 centres worldwide (with 2 units running on gantry treatment rooms [`www.ptcog.ch`].

At the IFJ PAN, proton therapy of ocular treatments started in *Feb.* 2011 [Swakon et al., 2010] [Romanowska-Dixon et al., 2012] with AIC-144 cyclotron. The treatment room and the optical line was developed by a team of physicists, engineers and IT team of IFJ PAN [Michalec et al., 2010], lead by Jan Swakoń, PhD. Up to *Dec.* 2015, 128 patients had been irradiated at the site.

A 60 MeV proton beam extracted from AIC-144 was scattered on the 25 μm Ta foil, mounted 10 m upstream from the isocentre [Swakon et al., 2010]. A passively scattered homogeneous beam was next mechanically formed along the optical line by the PMMA beam shaping elements inside the treatment room - a range shifter of adjustable thickness and rotating energy modulator wheel [Michalec et al., 2010]. For uveal patients, a relatively high dose rate is crucial since the patient's eyelid is immobilised and the patient has a gaze point to look at during the irradiation. At the AIC eye melanoma treatment room, the required dose rate ranged from 21 to 30 Gy/min to keep irradiation time of $30 \div 60$ s, with possible dose jump to 60 Gy/min if necessary [Swakon et al., 2010]. The distal range of 29 mm (R_{90}) achievable for the AIC-144 proton beam imposes a treatment limitation for the few percent of patients with larger eye balls [Kacperek, 2009].

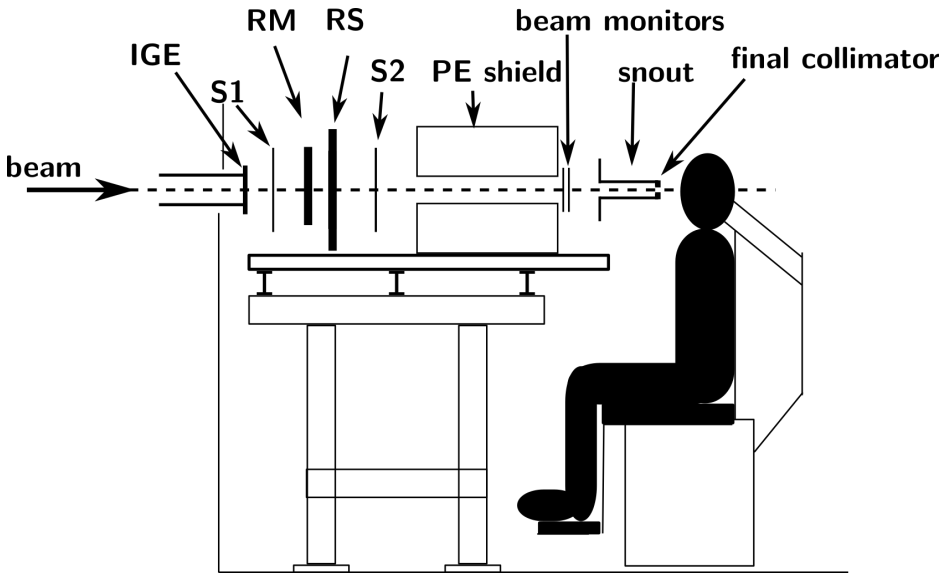

Figure 1.12. A scheme of beam shaping elements of the CCB eye-line treatment room (ELTR). The proton beam of 70 MeV enters the room from the left. The beam is formed in two scattering foils (S1, S2), degraded via a range shifter (RS) and modulated by a range modulator wheel (RM). After passing a biological shield made of PE, beam monitors check beam properties before the final patient irradiation. The final collimation of the beam is a steel snout ended with a brass patient-specific collimator. Elements and their positions are not to scale.

1.5.2. ELTR eye melanoma treatment room

In the CCB facility, the ocular treatment room was planned to take over eye melanoma patients from the AIC-144 cyclotron. The beam parameters specification for the eye treatment room (ELTR) was formulated in the tender documents and was verified during the cyclotron acceptance tests in *Nov* 2012 [CCB, 2014]. IBA was responsible for providing the beam to the so-called Ion Guide End (IGE) located at the eye treatment room. Downstream from IGE, the development of the optical line and patient positioning and immobilisation system was performed by the team from the IFJ PAN led by Jan Swakoń, PhD. In 2015, the ELTR received CE certification mark, as the effect of laborious collaboration between the IFJ PAN and IBA teams.From *Feb.* 2016 uveal melanoma patients have been treated at the new facility (*cf.* **Figure 1.11**).

The general arrangement of the beam shaping elements on the optical line is shown in **Figure 1.12**. The beam-line is ended by the vacuum window of 50 μm Ti at IGE. The beam is spread along the beam axis via energy modulator (commonly called the range modulator wheel, RM, used hereafter) to form desired SOBP dose distribution. By a range shifter (RS) with variable Lucite thickness the beam is degraded. Next, a polyethylene slab with internal diameter of 70 mm is mounted as a biological shield from scattered radiation [Stolarczyk et al., 2010]. After passing through beam monitoring devices (parallel-plate ionisation chambers from PTW, Freiburg, Germany), the beam is formed by a final collimation system consisting of the steel snout (internal diameter of 40 mm) mounted at the end of the optical bench closed with a final

brass collimator of $\varnothing 25\ mm$ or $\varnothing 35\ mm$, or with a patient-specific individually milled collimator.

The design of several elements of the eye line was copied from the AIC-144 facility to reduce the workload in the development of the new treatment room, such as RS, RM or final beam collimation - the devices were only tuned to respond 70 MeV beam like change in the RS minimal thickness. However, a completely new scattering system had to be built on the optical bench inside the treatment room. For the analysis of the scattering system solutions, Monte Carlo simulations were applied, as described in **Chapter 3**.

1.5.3. GTR gantry treatment room

At the CCB facility two gantry rooms (GTR3, GTR4) are dedicated for treating patients submitted to external radiotherapy (*cf.* **Figure 1.11**). The beam can be switched between two gantry rooms equipped with dedicated nozzles with modern Pencil Beam Scanning (PBS) implemented. Additional bending and focusing magnets are mounted on the gantry revolving 360° around the patient couch. Such beam rotation enables dose delivery with milimetric or submilimetric precision for all therapeutic ranges - the gantry rotational axis and central axis of the patient positioning system should be coaxial within diameter of $\varnothing 1$ or $\varnothing 2\ mm$ sphere as the gantry rotates [ICRU78, 2007]. Proton beam energies from the Proteus C-235 cyclotron span from 70 to 226 MeV corresponding to $4.1 \div 32\ g/cm^2$ range in water from *PSTAR* database [Berger et al., 2009]. For shallower tumour locations (less than 4.1 cm depth), gantry rooms are equipped with range shifters mounted on the nozzle which are mechanically inserted into the beam path. The narrow beam (minimal sigma size of 2.7 mm for 226 MeV) is deflected horizontally and vertically via scanning magnets with maximum scan area of $30 \times 40\ cm^2$ at the isocentre. A volume of $10 \times 10 \times 10\ cm^3$ is irradiated to 2 Gy within less than 1 min as verified during the acceptance tests. To get the gantry treatment rooms fully operational, commissioning of the treatment planning system is required. For calculation of the depth-dose distribution necessary to the TPS, Monte Carlo methods were applied, as described in **Chapter 4**.

Chapter 2

Methods of dosimetry and Monte Carlo-based dose calculations

The CCB dosimetry measurements were measured by teams from the PDKJ and from the PTO, with author participation or were provided to the author for MC simulation modelling and verification. The detailed third party contribution to this work can be found in the **Introduction**. For precise data acquisition and processing, nonetheless, the essential dosimetry information in proton radiotherapy, carried out at the CCB facility will be given in the first part of this chapter. The description will be followed by a description of the implementation of the Monte Carlo methods in dose assessment. Particular emphasis will be placed on the FLUKA code and its application in simulation of passive and active proton beam delivery techniques.

2.1. Methods of dosimetry in proton radiotherapy

Precision of the beam delivery in radiotherapy requires precise and reproducible dosimetry with overall uncertainties not exceeding 5% [TRS-398, 2001]. These are national and international reports on which procedures and codes of practice are based, ensuring dosimetry standardisation, both in reference and relative measurements.

In reference dosimetry, a clinical dosimeter is calibrated at a primary or secondary standards laboratory with reference to accurate and uniform standard of the absorbed dose. The dosimetric measurement is then reproduced on site with the same dosimeter likely preserving the reference conditions. Next, other on-site dosimeters are cross-calibrated.

The reference conditions should be reproducible and clinically relevant [Newhauser and Zhang, 2015]. The reference beam used in primary or secondary standard laboratories should correspond to the user's beam. However, due to the price and technical complications, none of the proton calibration beams have been determined by national or international calibration laboratories. Therefore, ^{60}Co gamma radiation is

recommended as the reference beam quality [TRS-398, 2001] for the calibration of the reference ionisation chambers.

Proton dosimetry, starting in the 1980's and early 1990's, evolved from Faraday cup measurements of the proton fluence in air to absorbed dose-to-water performed with an ionisation chamber (IC). IAEA (International Atomic Energy Agency) published Technical Report Series (TRS) 398 protocol "Absorbed Dose Determination in External Beam Radiotherapy", devoted for dosimetry in all external beams except neutrons [TRS-398, 2001]. It has become the gold standard of PT absorbed dose-to-water (D_w $[Gy]$) determination for scattered proton beam. However, the TRS-398 protocol dose not tackle the dosimetry of pencil scanning beams.

2.1.1. TRS-398 protocol formalism

The absorbed dose to water ($D_{w,Q}$ $[Gy]$) according to TRS-398 protocol formalism in a proton beam of quality Q under reference conditions is calculated as [TRS-398, 2001]:

$$D_{w,Q} = M_Q \cdot N_{D,w,Q_0} \cdot k_{Q,Q_0} \tag{2.1}$$

where M_Q $[C]$ is the dosimeter reading positioned at the depth z_{ref} and corrected for the atmospheric conditions, polarity effect, ion recombination and electrometer calibration. N_{D,w,Q_0} $[Gy/C]$ is the absorbed dose-to-water calibration coefficient of the dosimeter calibrated at the reference quality Q_0; and k_{Q,Q_0} is chamber-specific beam quality correction factor accounting for the different beam quality Q. The calibration coefficient N_{D,w,Q_0} is obtained from calibration performed in reference ^{60}Co beam at a standards laboratory.

Based on water-to-air stopping power ratios, mean energies per ion pair production ratios and perturbation factors under beam Q_0 and Q, k_{Q,Q_0} were calculated and are tabulated in the TRS-398 protocol for each ionisation chamber type, as a function of residual range (dependent on proton beam energy and depth of the measurements) [TRS-398, 2001].

As for other external beams, water is recommended as the reference medium for proton beams. For relative measurements and routine daily-checks, solid phantoms are more convenient due to easier set-up and better reproducibility of the chamber positioning. In such cases, water-equivalent thickness values have to be applied.

2.1.2. Reference and relative dosimetry at CCB IFJ PAN

At the CCB IFJ PAN, there are two reference dosimetry sets: first includes a Farmer ionisation chamber 0.6 cm^3 TM30010 (PTW, Freiburg, Germany) with Unidos^{Webline} electrometer T10021 (PTW, Freiburg, Germany) and second includes a Mrakus IC TM23342 (PTW, Freiburg, Germany) with Unidos^{Webline} electrometer T10021 (PTW, Freiburg, Germany). The sets are calibrated in reference conditions at the Secondary Standard Dosimetry Laboratory at the Department of the Medical Physics Oncology Centre, Warsaw (ZFM COI Warszawa) according to TRS-398 protocol [TRS-398, 2001]. The remaining ionisation chambers (Semiflex 0.125 cm^3 TM31002 and TM31010, Farmer TM30013 or Markus TM23343, all PTW, Freiburg, Germany) with Unidos electrometers (Unidos T10001 and Unidos^{Webline} T10021, both

PTW, Freiburg, Germany) are cross-calibrated using ^{60}Co beam from *Theratron 780E* in a $30 \times 30 \times 30$ cm^3 water phantom 41001 (PTW, Freiburg, Germany) according to TRS-398 protocol [TRS-398, 2001]. Prior to the patient dosimetry, absolute and relative dosimetry with the cross-calibrated dosimeters are performed. Depending on the treatment room (ELTR or GTR), various dosimetry equipment is used for relative dosimetry (such as range verification, beam profile measurements).
In the following subsections crucial details are given for each type of dosimetry measurements, regarding the data needed for the verification of the MC simulations carried out within this work.

2.1.3. Dosimetry methods at CCB-ELTR

Reproducibility of the ELTR beam parameters must be periodically checked. During the morning QA, the 1D and 2D lateral beam profiles are measured in air, together with depth-dose profiles acquired either in water or PMMA, similarly to other eye tumour facilities (*e.g.* [Bonnett et al., 1993] [Linz (ed.) and Kacperek, 2012] [Michalec et al., 2010] [Nauraye et al., 1995]).

1D lateral beam shape in-air

For ELTR checks of the beam lateral profile in air, a semiconductor rectifier diode 1N4007 is used. The diode is placed in the in-house developed X-scanner consisting of a stepper motor VEXTA moving the diode in direction perpendicular to the beam axis, and an encoder type MOK 40. The X-scanner is mounted at the snout, with 5 cm distance between the collimator surface and the diode. **Figure 2.1** illustrates the measurement set-up with the rectifier diode and a plotted exemplary lateral profile. The generated diode current is read out from an Ergen electrometers (Ergen, Kraków, Poland) and corrected for the beam fluctuations registered by beam monitor positioned right after the IGE. Acquired 1D vertical and horizontal current ratios are referred to the absorbed dose profiles. Accounting for the precision of the stepper motor and positioning uncertainties, the overall measurement resolution is assumed to 0.1 mm. The measurement of the beam lateral profiles is performed according to CCB procedures, described in [CCB Quality Book, 2015].

2D lateral beam shape in-air

Measurements of the 2D lateral beam profiles in-air is performed using Proton Beam Imaging System (*ProBImS*) developed by Marzena Rydygier, PhD [Rydygier, 2016]. The ProBImS (**Figure 2.2**) includes a thin scintillator positioned perpendicularly to the beam axis, a high resolution CCD camera ATIK 383 L+ and a 45° glass mirror to reflect scintillation photons towards the camera. The system is locked in a light-tight cover to prevent from unnecessary background light reflections with CCD camera positioned off-axially to limit its radiation exposure. The system is mounted on the patient positioning chair with a dedicated holder, with scintillator positioned at the given distance from the final collimator surface along the beam axis (shown in left top of **Figure 2.3**).

The 2D beam image acquisition is schematically presented in **Figure 2.3**. A single pixel of the CCD matrix with 5.4×5.4 μm^2 corresponds to 26×26 μm^2 pixel size on the scintillator. Size of the camera view is 6.5 $cm \times 8.6$ cm. The system was found to show

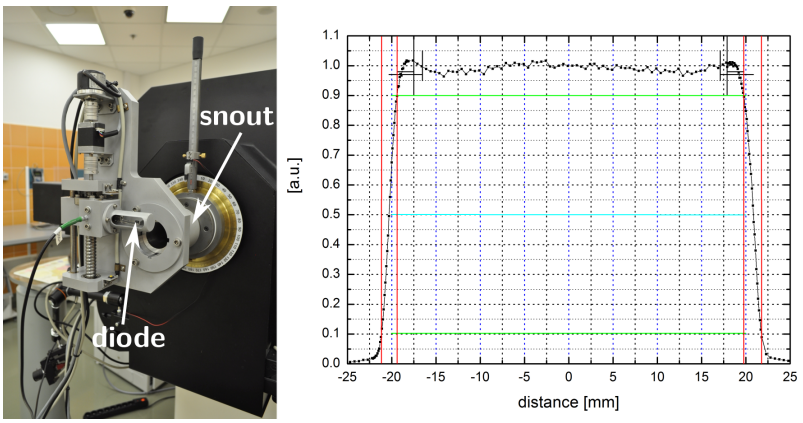

Figure 2.1. (left) A rectifier diode measurements placed in the X-scanner mounted on the snout with an exemplary X profile acquired in plane perpendicular to the beam axis (right). [Courtesy of PTO]

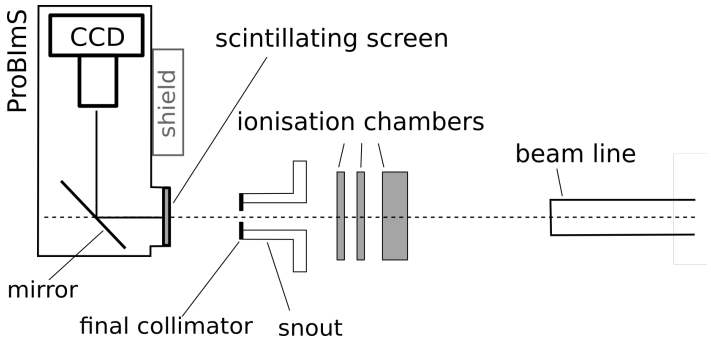

Figure 2.2. A scheme of the **ProBImS** system positioned after the final collimator, axially to the beam axis (dotted line). [Courtesy of M. Rydygier - detailed description in [Rydygier, 2016]]

linear dose response between 1 and 15 Gy [Rydygier et al., 2015] [Rydygier, 2016]. 2D image is captured as a set of two-dimensional matrix $I^{CCD}(x, y)$, with image resolution ranging from 0.02 mm/pix to 0.03 mm/pix depending on the applied lens [Rydygier, 2016].

For the measurements of the ELTR pristine pencil-beam, a 2D image $I^{CCD}(x, y)$ acquired with ProBImS was normalised to its maximum value. The coordinates of the image centre of mass $\overrightarrow{CM}$ were calculated from the image area above 80% according to the following expressions [Rydygier, 2016]:

$$CM_x = \frac{\sum_{x,y} x \cdot I(x,y)}{\sum_{x,y} I(x,y)}$$
$$CM_y = \frac{\sum_{x,y} y \cdot I(x,y)}{\sum_{x,y} I(x,y)}. \tag{2.2}$$

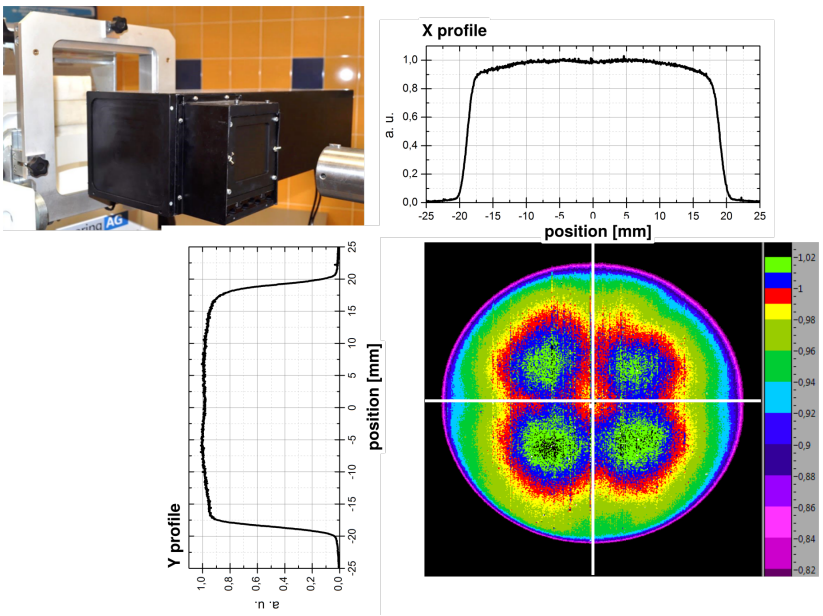

Figure 2.3. ProBImS system mounted on the therapeutic chair at the AIC-144 facility (left top). Exemplary acquired 2D beam image (right bottom) is analysed with X and Y profiles extraction (right top and left bottom, respectively). [Courtesy of M. Rydygier - detailed description in [Rydygier, 2016]]

Profiles X and Y, extracted from the spot image $I^{CCD}(x, y)$ through the spot centre of mass $\overrightarrow{CM}$ are then described as follows [Gajewski, 2016]:

$$\begin{aligned} X(x) &= I^{CCD}(x, CM_y) \\ Y(y) &= I^{CCD}(CM_x, y) \end{aligned} \tag{2.3}$$

For the above mentioned 1D profiles $X(x)$ and $Y(y)$, 1D Gaussian curves were fitted:

$$\begin{aligned} f(x) &= A_x \cdot \exp\left(\frac{-(x-\mu_x^2)}{2\sigma_x^2}\right), \\ f(y) &= A_y \cdot \exp\left(\frac{-(y-\mu_y^2)}{2\sigma_y^2}\right) \end{aligned} \tag{2.4}$$

from which spot position $\vec{S} = [\mu_x, \mu_y]$ and spot size σ_x $[mm]$ and σ_y $[mm]$ were calculated [Rydygier, 2016] [Gajewski, 2016].

Depth-dose distribution in water

The depth-dose and lateral dose profiles in water are acquired with a Markus ionisation chamber TM23343 (PTW, Freiburg, Germany) with sensitive volume of 0.055 cm^3 and radius $r = 0.256$ cm. The IC is immersed in an in-house developed water phantom of inner dimensions 10 $cm \times 12$ $cm \times 16$ cm (XYZ) with 1 cm thick PMMA walls. The Markus IC is mounted on the dedicated holder compatible with the in-house developed 3D-scanner. The 3D-scanner consists of three perpendicular

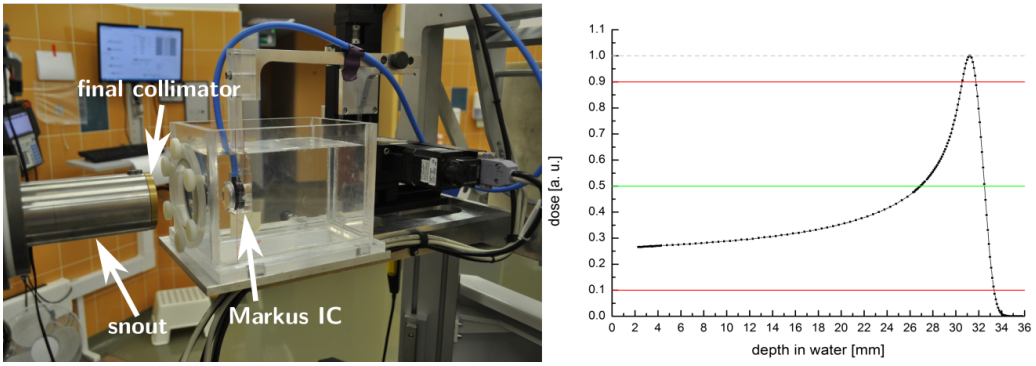

Figure 2.4. (left) Measurement with Markus ionisation chamber placed in the 3D-scanner mounted on the treatment chair with an exemplary acquired depth-dose distribution along the beam axis for unmodulated scattered beam (right). [Courtesy of PTO]

OWIS LTM 60-50-MSM linear stages moving the Markus chamber along XYZ axes with stepper motors. The 3D scanner is mounted on the patient positioning chair, with a mounted measurement set, as shown in **Figure 2.4**. The water phantom is screwed on the 3D-scanner and filled with distilled water. Frontal surface of the phantom is positioned perpendicularly to the beam axis. It has an entrance window of $\varnothing 6.0\ cm$ made from mica of 0.2 mm thickness ($WET_{mica} = 0.45\ mm$).

The Markus IC is connected to a Unidos^{Webline} T10021 electrometer (PTW, Freiburg, Germany). The dosimeter read-out is recalculated either as relative depth-dose distribution normalised at the BP depth (as shown in the right side of **Figure 2.4** or calculated for dose in water $D_{w,Q}$ with dedicated absorbed dose-to-water calibration coefficient N_{D,w,Q_0} and corresponding correction factors (here atmospheric conditions only) according to **Equation 2.1**. The measurement resolution is assumed to 0.1 mm, including stepper motors precision, IC and treatment chair positioning precision together with mica entrance window deflection from water. Relative standard uncertainty of the Markus IC $u(D^{Markus})$ is assumed to 2.3% following [TRS-398, 2001].

For beam range verification the Markus chamber measurements are also performed in a PMMA disk of changeable thickness however this method of dosimetry is not applied in this work and will not be described here.

2.1.4. Dosimetry methods at CCB-GTR

Routine QA procedures of the gantry pencil beam scanning system implies extensive dosimetric measurements such as spot size and position verification, its gantry angle dependence, gantry isocentricity, field homogeneity, output factor (ratio between the absorbed dose and required monitor units) stability verification etc., which lay out of scope for the thesis. Only dosimetry measurements performed during the commissioning phase of gantry rooms (GTR3, GTR4) will be described relevant to the developed MC beam model. Similarly to other PBS facilities with active scanning of the proton beam, customarily 2D lateral spot images are captured in-air along the

beam axis, complemented with DDD measurements of single pencil-beams for a set of therapeutic energies (*e.g.* [Paganetti, 2011]).

Depth-dose distribution

At the CCB depth-dose distribution of the scanning pencil beam is measured using a Bragg Peak Chamber (BPC) TW34070 (PTW, Freiburg, Germany). The BPC is a plane parallel ionisation chamber with radius $r = 4.08\ cm$, the sensitive volume of $10.5\ cm^3$ and $4\ mm$ water equivalent thickness of the entrance window. The ionisation chamber is positioned in the *Blue Phantom*^{2} (IBA Dosimetry, Schwarzenbruck, Germany) mounted at the technical table in the gantry treatment room. The phantom (exterior: $67.5\ cm \times 64.5\ cm \times 56.0\ cm$) has $1.5\ cm$ PMMA walls of $1.18\ g/cm^3$ and is filled with distilled water with an additive called AquaBlue (IBA Dosimetry, Schwarzenbruck, Germany). The Aqua Blue is a water agent assumed to have an insignificant impact on the water density [Dosimetry, 2013]. The *Blue Phantom*^{2} has 3D servo system for chamber positioning (with precision of $0.2\ mm$). The chamber assembly enables measurements without wall irradiation, with gantry angle $\phi_G = 0°$, shown in left side of **Figure 2.5**. It is also possible to irradiate through the *Blue Phantom*^{2} walls or dedicated entrance window ($\phi_G = 90°$, $\phi_G = 270°$) which is $2.93 \pm 0.03\ mm$ thick with inner diameter of $\varnothing 20.0\ cm$. The BPC is connected to the dedicated Common Control Unit (CCU, IBA Dosimetry, Schwarzenbruck, Germany) with integrated two-channel electrometer. The output of the beam monitors IC2 and IC3 is also connected to the CCU with an entrance beam signal for beam fluctuations correction (IC2 and IC3 are located in the nozzle). Control of the BPC is done via *OmniProAccept* software (IBA Dosimetry, Schwarzenbruck, Germany). Obtained $DDDs(E)$ are first corrected for IC2/IC3 signal, then normalised to the BP maximum resulting in $PDD^{BPC}(E)$ curves. In the right side of **Figure 2.5** $IDD^{BPC}(E)$ distributions measured distributions are shown, normalised at the $2\ cm$ depth. The uncertainty of the range measurements was estimated to $0.5\ mm$ [Mojżeszek, 2018]. The uncertainty of the relative dose read-out $u(D^{BPC})$ was assumed to 0.9% [Mojżeszek, 2018]. The measurement is performed according to the internal procedures with details given in [CCB Quality Book, 2015].

Lateral spot size in air

For verification of the beam spatial distribution, the Lynx PT (IBA Dosimetry, Schwarzenbruck, Germany) is used [Fimel, 2015], shown in **Figure 2.6**. The system consists of $30 \times 30\ cm^2$ scintillation screen, a mirror reflecting scintillation photons and a CCD camera for image acquisition. The intensity of each pixel refers to the proton fluence impinging on the scintillation screen. Single spot and spot maps parameters verification is evaluated for various proton beam energies according to internal CCB procedures covered by [CCB Quality Book, 2015].

The Lynx PT can either be positioned at the treatment couch or mounted to the nozzle and rotated with the gantry, with the scintillation screen perpendicular to the beam axis. For the spot size measurements, the gantry angle $\phi_G = 270°$ is set with Lynx PT positioned at the treatment table to move it along the beam axis, as shown in the left side of **Figure 2.6**.

From a single exposure, 2D images are captured as a set of two-dimensional matrix

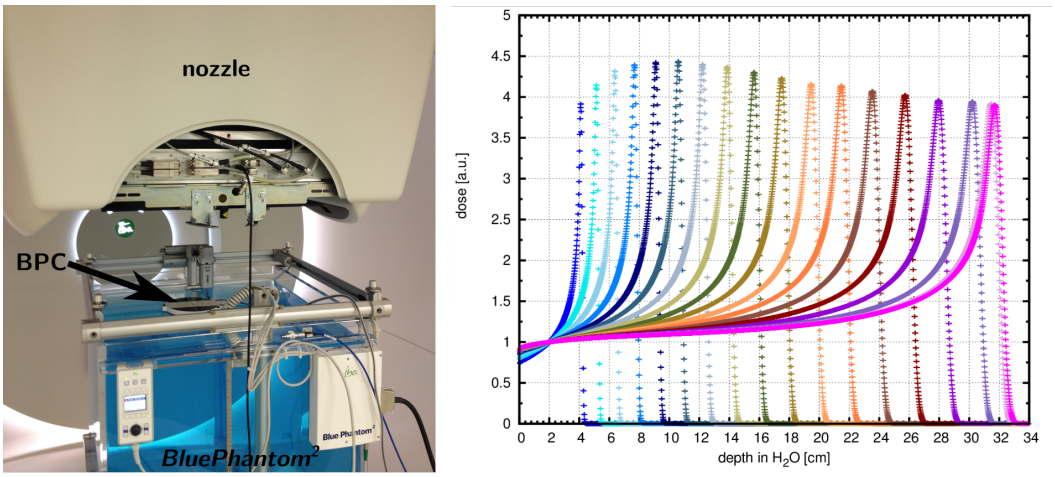

Figure 2.5. (left) *BluePhantom*^{2} (IBA Dosimetry) positioned at the technical table for depth-dose profiles measurements with the Bragg Peak Chamber (PTW) immersed in distilled water with colouring agent added. The beam impinges the water directly - gantry angle $\phi_G = 0°$. (right) Exemplary set of $IDD^{BPC}(E)$ distributions normalised at 2 cm depth. [Courtesy of PDKJ]

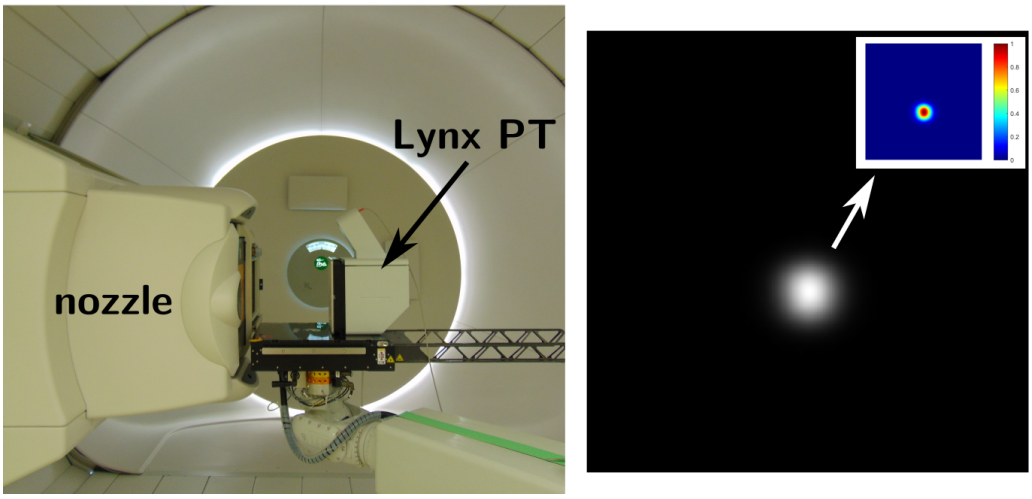

Figure 2.6. (left) Lynx PT detector placed on the treatment couch with the scintillating screen perpendicular to the beam axis for gantry angle $\phi_G = 270°$. (right) An exemplary single spot image of $E = 70\ MeV$ in black-white scale, reploted in colour scale normalised to the maximum intensity value (colour insert). [Courtesy of PDKJ]

$I(x, y)$, each element containing a recorded intensity of the scintillation. Spatial resolution of the images from Lynx PT reaches 0.5 mm [Farr et al., 2013]. The inhomogeneity of the scintillating screen is corrected by a periodically determined response matrix. However, energy-dependent response to protons must be taken into account during the measurements [Gajewski, 2016]. From the measured image, the spot centre of mass is calculated as a vector $\overrightarrow{CM}$ with the components following **Equation 2.2** [Gajewski, 2016]. Profiles X and Y, extracted from the spot image $I(x, y)$ through the spot centre of mass $\overrightarrow{CM}$ are then described according to **Equation 2.3** [Gajewski, 2016]. For 1D profiles X and Y, 1D Gaussian curve is fitted similarly to profiles from the ProBImS system, with **Equation 2.4**, from which spot position $\vec{P} = [\mu_x, \mu_y]$ and spot size σ_x $[mm]$ and σ_y $[mm]$ are calculated [Gajewski, 2016].

Lateral spot size in medium

For more accurate spot shape verification, passive dosimetry methods are used, such as radiochromic films or thermoluminescence detectors and foils (TLD) developed also at the IFJ PAN [Olko et al., 2006] [Bilski, 2012] [Gajewski et al., 2016]. The TLD foil system enabling 2D image acquisition has been applied by Jan Gajewski, PhD [Gajewski, 2016]. TL foils or radiochromic films allow the determination of the spot size at the given depth when installed between the phantom plates. At the CCB, RW3 T29672 slab phantom (PTW, Freiburg, Germany) is used. It consists of 33 plates of size 30 $cm \times 30$ cm, made of water-equivalent RW3 material (polystyrene C_8H_8 containing 2% $\pm$ 0.4% TiO_2) of 1.045 g/cm^3 density [PTW, 2015].

2D TLD foils with thermoluminescent powder $LiF : Mg, Cu, P$ (MCP) were placed between RW3 phantom plates and irradiated from the top (gantry angle $\phi_G = 0°$), as shown in **Figure 2.7**. The resulting 2D lateral dose profiles were fitted with rotated 2D Gaussian distribution:

$$f^R(x, y) = A^R \cdot \exp\left(-\frac{[(x-\mu_x^R)\cos\theta+(y-\mu_y^R)\sin\theta]^2}{2\sigma_x^{R\,2}} - \frac{[(y-\mu_y^R)\cos\theta-(x-\mu_x^R)\sin\theta]^2}{2\sigma_y^{R\,2}} \right), \tag{2.5}$$

where A^R being normalised to the spot maximum value, spot position is described by $\vec{P}[\mu_x^R, \mu_y^R]$, spot rotation by θ and spot size by σ_x^R $[mm]$ and σ_y^R $[mm]$ [Gajewski, 2016].

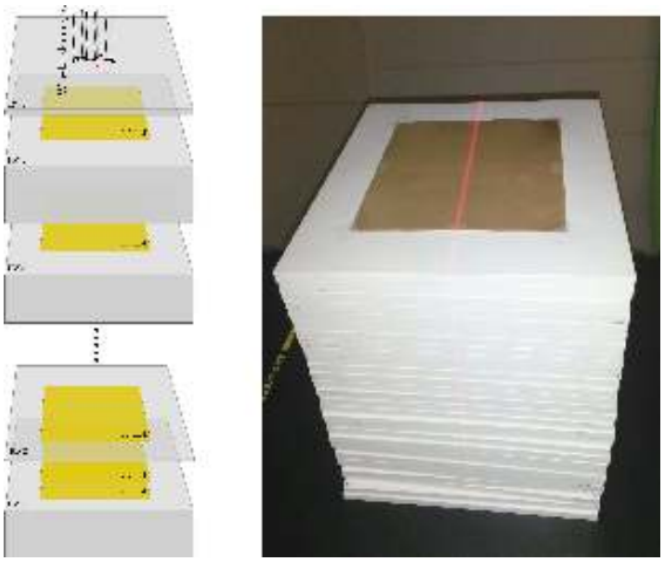

Figure 2.7. (left) Scheme of the 2D TLD set-up in the RW3 phantom for spot size measurements as a function of depth. (right) The experimental set-up with visible entrance 2D TLD foil placed on the RW3 phantom. Reprinted from [Gajewski, 2016].

2.2. Monte Carlo calculation methods in radiation transport

The first attempts to use a Monte Carlo-like approach date back to 1777 when Georges-Louis Leclerc, Comte de Buffon, estimated the probability P of a needle of given length L being randomly tossed on a plane ruled with parallel lines of equal distance d (where $d > L$) [Mayles et al., 2007]:

$$P = \frac{2L}{\pi d}. \tag{2.6}$$

In 1886, Laplace applied this approach for the determination of the π number, given the probability of the event. The precision was improved by increasing the number of trials (tosses).

Initially Monte Carlo methods were used for solving differential equations, however its quick development was observed during World War II, when its applications in solving problems in physics was accompanied by the beginning of the computer era. The method was intensively expanded in Los Alamos by John von Neuman and Stanisław Ulam for neutron transport calculation, who also coined the name *Monte Carlo* (MC). Thanks to the employment of the first computers, modelling of stochastic processes with a large number of events enabled the rapid spread of the Monte Carlo methods, also into many other disciplines.

The principle of MC method is a simulation of particle transport on a step-by-step basis. For each step a random number is sampled from a probability density function. Contemporary random number generators feature a period long enough not to repeat itself during a single simulation [Paganetti, 2011]. A probability density function corresponds to the physics - it is the probability of given type of interaction for a given particle. For protons all possible interactions are taken into account: excita-

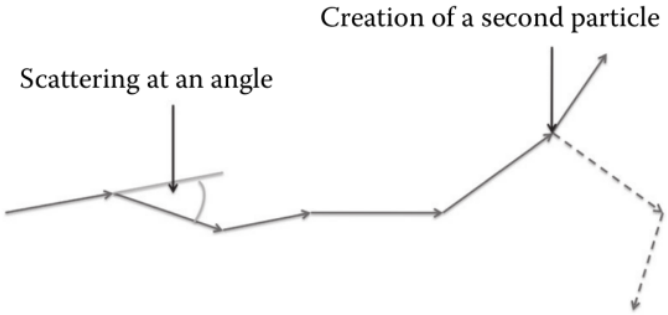

Figure 2.8. A scheme of particle tracking during the Monte Carlo simulation - the illustration shows particle scattering under a given scattering angle, and interaction with medium through which a secondary particle is created. Reprinted from [Paganetti, 2011].

tion, ionisation, multiple Coulomb scattering and nuclear interactions. The secondary particles generated in these processes (so-called *secondaries*) are also tracked with primary particles down to the predefined energy cutoff (transport threshold) when the remaining energy is deposited in a point. Tracking of a primary particle with all its secondaries is called a particle history. A scheme of a MC simulation of a particle path is presented in **Figure 2.8**.

The number of tracked particle histories influences the uncertainty of the method - for N simulated histories the uncertainty of the calculated quantity is proportional to $1/\sqrt{N}$ [Paganetti, 2011]. From the *Central Limit Theorem*, assuming the true average $\bar{x}$ exists and the distribution in x has a true finite variance σ_x^2, by increasing the number of simulated histories N, Monte Carlo estimator of $\bar{x}$ denoted as $< x >$ arbitrary approaches $\bar{x}$. *Central Limit Theorem* guarantees also that distribution of $< x >$ is Gaussian, described by a variance $\sigma^2_{<x>}$ which may be estimated in the simulation. For $N \to \infty$, from the *Central Limit Theorem*, variance $\sigma^2_{<x>}$ goes to zero.

In radiation physics Monte Carlo methods are used to track individual particles. Particle tracking is performed using theoretical models and parametrisation of the available experimental data based on which cross sections are calculated. Typically, each interaction of a particle is simulated and tracked with all secondaries down to the transport threshold. For charged particles like protons, a so-called condensed history method evolved. Energy losses and directional changes are summed into a net result of several single-scattering events occurring in a single step. This approach enables faster simulations, but it decreases the precision of the calculation. Therefore, in some codes the user is allowed to switch between the condensed history and the discrete process handling. In the MC simulations of the proton beam the following physics is frequently taken into account [Paganetti, 2011]:

- energy loss of protons by Bethe-Bloch formula down to 2 MeV (*cf.* **Equation 1.2**),
- parametrisation based on stopping power formalism from ICRU below 2 MeV [ICRU49, 1993],

- multiple Coulomb scattering with condensed history implementation (*cf.* **Chapter 1.1.3**):
  — scattering angle by the Moliere theory,
  — Lewis theory for calculation of moments of the lateral displacement,
- nuclear interactions derived from available cross sections, models or combinations of model, parametrisation and existing experimental data.

2.2.1. Monte Carlo methods in radiotherapy

For the purpose of proton transport simulations, a variety of Monte Carlo codes are available, such as FLUKA [Ferrari et al., 2005] [Battistoni et al., 2016], Geant4 [Agostinelli et al., 2003] [Allison et al., 2006], MCNPX [Pelowitz, 2011] [Waters, 2002], VMCpro [Fippel and Soukup, 2004] and SHIELD-HIT12A [Bassler et al., 2014]. Customarily the user is to prepare an input file defining the particle source and geometry which is run with software executable. Some codes enable more flexibility, such as Geant4, being the assembly of toolkit libraries to be linked. For better program handling, graphical interfaces for a given code are also available, like GATE [Jan et al., 2004] [Jan et al., 2011], TOPAS [Perl et al., 2011], or *flair* [Vlachoudis, 2009].

Monte Carlo methods found multiple applications in radiotherapy [Seco and Verhaegen, 2016]. In ion therapy simulations, a number of effects are to be considered due to charged particles interactions, occurring during the beam degradation, in the treatment nozzle or in the patient body especially in case of large uncertainties. Moreover, when compared with photon radiotherapy techniques, treatment with light ions requires the analysis of the LET dependency, paving the way for RBE research. Wherefore MC methods can be applied in *i.a.* [Paganetti, 2011] [Newhauser and Zhang, 2015]:

- analysis of the characteristics of the beam and the beam line design,
- design of the treatment nozzle (both for passive and active beam delivery techniques),
- beam model development,
- QA issues as an alternative dose engine for dose calculation or evaluation of the beam perturbation in case of implants.

More sophisticated simulations include irradiation of the moving organs, development of the detector system for the measurement of prompt-gamma from proton interactions [Kang and Kim, 2009], *in situ* or *in vivo* dose verification [Parodi et al., 2007b] [Parodi et al., 2007a], or secondary neutron dose assessment [Farah et al., 2015] [Stolarczyk et al., 2018].

The application of the MC codes is targeted depending on the code development purpose, mainly due to the underlying physics tailored to the given range of particles and energies [Paganetti, 2011]. Applied physics models may cause discrepancies and it is important to choose a MC code relevant to the problem. Other uncertainties of the MC calculations may be caused by material constants, such as mean excitation energy (discussed in detail below in **Section 2.3.4**). From a statistical point of view, the step size of a tracked particle or number of primaries also influences the accuracy of the results.

MC code validation and benchmarking are carried out, together with codes intercomparison useful for a better understanding of their appropriateness. *E.g.* [Kim-

strand et al., 2008] analysed Geant4, FLUKA and MCNPX codes and compared to the experimental data in terms of scattering components generated at the aperture edges, showing significant impact on the user-defined parameters. [Randeniya et al., 2009] studied the same three codes for the eye treatment simulations, obtaining comparable results between all three codes for lateral and depth-dose profiles with the highest code efficiency of the FLUKA code (though it was for FLUKA 2006 code version). For the purpose of the patient dose calculation, MC calculated dose estimation accuracy is verified, *e.g.* [Stankovskiy et al., 2009] [Paganetti et al., 2004] [Robert et al., 2013].

2.3. FLUKA - Monte Carlo multi-particle transport code

The Monte Carlo code FLUKA (FLUktuierende KAskade - *Engl.* fluctuating cascade) was written in FORTRAN by Johannes Ranft and co-workers from CERN in $1960's$. The code was enriched by a group of developers, *i.a.* J.M. Zazula from IFJ PAN was one of them up to version *FLUKA 90* [Zazula, 1990]. The code was originally dedicated for shielding calculations in high-energy accelerator physics [Ferrari et al., 2011]. The current version of general purpose particle transport code is the result of the collaboration between CERN and INFN [Battistoni et al., 2016] [Ferrari et al., 2005]. The code consists of the FORTRAN routines and subroutines executing underlying physical models. For input files handling, *flair* graphical user interface was developed [Vlachoudis, 2009][`www.fluka.org/flair`]. The code can be downloaded from the official web-page: `www.fluka.org`.

2.3.1. Physical models in FLUKA code

The FLUKA code comprises refined physical models in terms of accuracy and completeness. The final estimations of the calculated quantities are given with a minimal set of user-dependent free parameters. Compared to other codes like Geant4 with user-request libraries added, FLUKA has rather a limited ability for modification of the particle tracking settings. The code efficiency is optimised *e.g.* in biasing options [Battistoni et al., 2016]. The variety of the FLUKA code benchmarking and physical models development, being far beyond the scope of this work, can be found in the *Publications* section at the FLUKA web-site [`www.fluka.org`].

The following physical processes and models are taken into account in ion simulations [Battistoni et al., 2016] [Ferrari et al., 2011]:

- electronic stopping power is based on Bethe-Bloch formula (*cf.* **Equation 1.2**) with Barkas and Bloch corrections for projectile stopping in the given medium;
- energy loss fluctuations and secondary electrons production are solved by the application of the cumulants of distributions, avoiding limitations from classical approach from Landau and Vavilov distributions [Battistoni et al., 2016]; an arbitrary thresholds for the δ ray production and transport are user-defined values down to 1 keV;
- the dedicated charge particle transport algorithm is based on Molière's theory of multiple Coulomb scattering improved by Bethe with Fano correction for multiple scattering;
- nuclear interaction modelled by the PEANUT package, is activated for hadron,

photon, muon and neutrino inelastic nuclear interactions from a few MeV up to several GeV [Ferrari and Sala, 1998] [Ferrari and Sala, 2002];
- a modified Relativistic Quantum Molecular Dynamics (RQMD) model [Sorge et al., 1989] is employed for nucleus-nucleus interactions between 0.125 and 5 GeV/n; Boltzmann Master Equation model is applied below 150 MeV/n [Cerutti et al., 2006].

For simulations of the ion beams in therapeutic ranges, the HADROTHE(rapy) card applies a set of defaults [Ferrari et al., 2011]:
- electrons, positrons and photons detailed transport is switched on;
- low-energy neutron transport down to thermal energies is applied (up to 20 MeV);
- particle transport threshold at kinetic energy of 100 keV is used except for neutrons simulated down to thermal energies (1×10^{-5} eV);
- multiple scattering threshold at minimum allowed energy is applied (both for primary and secondary charged particles);
- delta ray production threshold is set to 100 keV.

2.3.2. Validation of the FLUKA code

The FLUKA Monte Carlo code has been intensively developed and validated for particle therapy purposes. The main benchmarking includes comparison of the depth-dose and lateral dose distributions with results of the measurements in a water phantom. Its first validation for carbon ion beam therapy was conducted for an in-beam Positron Emission Tomography (PET) at Gesellschaft fur Schwerionenforschung (GSI, Darmstadt, Germany) [Sommerer et al., 2006]. A group from the Heidelberg Ion Beam Therapy Centre (HIT, Heidelberg, Germany) applied the FLUKA code in the commissioning of the synchrotron-based facility, verifying depth-dose measurements [Parodi et al., 2012] [Mirandola et al., 2015] and lateral dose-profiles [Schwaab et al., 2011]. **Figure 2.9** from [Battistoni et al., 2016] shows an exemplary comparison between proton and carbon ion beams simulated in FLUKA and measured with PeakFinder water column (PTW, Freburg, Germany) [Parodi et al., 2012]. The position of the Bragg peaks calculated with the FLUKA code is reported to agree with experimental uncertainties within 100 μm, and the dose difference within 1% for protons [Battistoni et al., 2016].

Experimentally validated FLUKA code is currently applied in a wide range of radiotherapy applications: *i.a.* as a complementary tool during the commissioning of a novel PT facility, in radiation protection calculation, in commissioning of treatment planning systems (TPSs) or patient-specific dose validation and calculation [Battistoni et al., 2016]. FLUKA tools developed for computed tomography (CT)-based simulations or feasible biological effect calculation with external radiobiological database shows the code strong position as a complementary tool in contemporary proton therapy management.

2.3.3. Monte Carlo simulation of the CCB facility

The FLUKA code was chosen for the modelling of the CCB proton beam for radiotherapy purposes due to its verified reliability, free access and the author's previous experience with the code for hadron therapy purposes [Jelen et al., 2014]. Being not

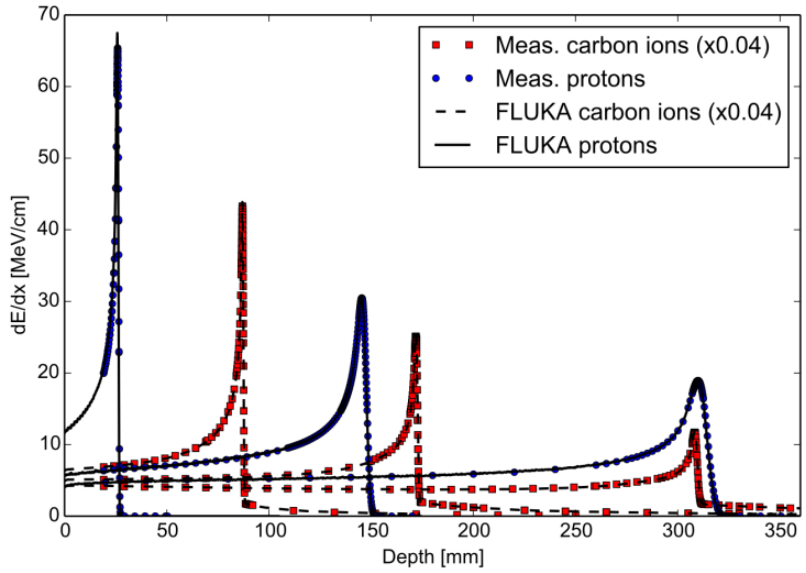

Figure 2.9. Results of the FLUKA simulations of the depth-dose profiles for proton and carbon ion beams compared with experimental data measured at HIT [Parodi et al., 2012]. The beam nominal energies were 54.19, 142.66 and 221.05 MeV for protons, and 200.28, 299.94 and 430.1 MeV/n for carbon ions. Reprinted from [Battistoni et al., 2016].

only established particle transport code, but also general purpose, FLUKA enables the implementation of proprietary CT-stoichiometric calibration curves, calculation on the voxelised external CT or β^+ emitters calculation for *in situ* PET dose verification, which may be introduced in the future for CCB proton beam.

All simulations were performed in the FLUKA code ver. 2011.2. (2011.2c-6 and 2011.2x). From default settings, HADROTHErapy card was chosen implying thresholds described in **Section 2.3.1**. No additional energy or particle transport thresholds were used for the purpose of this work. No biasing options were used in order to speed up the simulations. All particles were generated and tracked in the same manner, without any techniques of importance sampling.

A simplified geometry of the CCB treatment rooms were modelled in the FLUKA code, separately for ELTR and for GTR rooms. The impact from the concrete walls, floor or ceiling or from the equipment located inside the treatment room on the scoring quantities was neglected, and they were not modelled in the code. Also the beam line from the cyclotron up to the treatment rooms was omitted and emphasis was put to properly model the final beam shape at the entrance to the treatment room. All in-beam beam modifying elements were modelled according to their true sizes and materials, if known and feasible.

In all MC simulations single proton pencil-beams were used. By default the FLUKA code runs the beam "horizontally" along Z axis, whereas X and Y directions are perpendicular to the beam axis. The particle source is defined through the BEAM card in the FLUKA code. It allows to define main source characteristics:

- particle type,

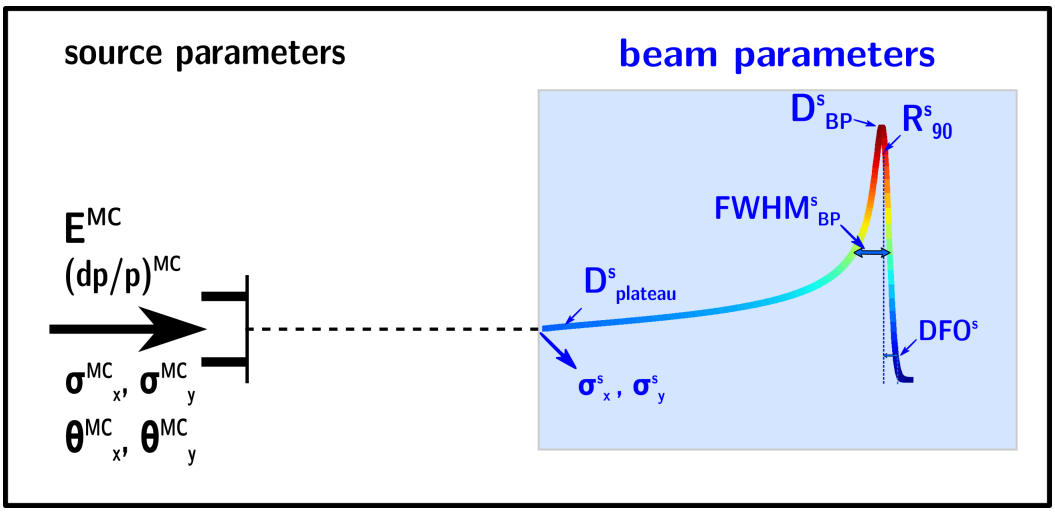

Figure 2.10. Scheme of the FLUKA simulation geometry with applied source parameters: source energy E^{MC}, source momentum spread $(dp/p)^{MC}$, source spatial distribution σ_x^{MC} and σ_y^{MC} and source angular distribution θ_x^{MC} and θ_y^{MC}. From the simulated dose distribution, simulated (s) beam parameters can be evaluated, *e.g.* beam range R_{90}^s, distal fall-off DFO^s, peak width $FWHM_{BP}^s$ or $max/plateau$ ratio as calculated as $D_{BP}^s/D_{plateau}^s$. From lateral dose distribution spot size σ_x^s and σ_y^s can be derived, here at the entrance depth.

- particle energy (momentum) and its momentum distribution (flat or Gaussian),
- source spatial distribution (rectangular, annular or Gaussian),
- source angular distribution (flat, isotropic or Gaussian).

Additionally, beam obliqueness may be defined through direction cosines if the beam is not parallel to the Z axis. More complicated source definitions exceeding available distributions may be defined via function or read from external phase space files, linked through SOURCE card in the FLUKA code.

For CCB beam models, position of the source was adopted to agree with experimental beam parameters. It was placed around $1-2$ m upstream of the isocentre, depending on the specific treatment room conditions (*cf.***Chapters 3.2** and **4.2**). Source energy E^{MC} and its momentum distribution $(dp/p)^{MC}$, spatial and angular distributions (σ^{MC}, θ^{MC}) were tailored to agree with experimental data, separately for ELTR (**Chapter 3.2**) and GTR (**Chapter 4.2**). **Figure 2.10** illustrates the main source parameters and simulated (s) beam parameters, extracted to be validated against the measured ones. While both for ELTR and GTR MC beam models were developed for the first time, no phase space files were created within this work.

For the calculation of relative difference (RD) between measured (m) and simulated (s) values (x), the following relation was applied [Ustaw, 2017]:

$$RD[\%] = \frac{x^m - x^s}{x^s} \cdot 100\% \tag{2.7}$$

For the ELTR simulations, the beam is then transported through all major beam shaping components, like scattering foils, range shifter or the beam collimation system ended up with dedicated brass collimator. For the GTR room, gantry nozzle

was not modelled for the MC beam model simplification, thus the beam was transported through the air only. FLUKA has a built-in Material Database [Ferrari et al., 2011], including material and tissue compositions recommended by ICRU with their expanded characteristics such as effective atomic number and atomic weight, density and composition, inelastic and elastic scattering length, radiation length etc. [Ferrari et al., 2011]. If not specified in the following chapters separately, FLUKA Material Database was used to assign compound to a given element of the treatment geometry.

In the FLUKA code the user defines the grid in which the sought quantity is recorded, a process which is called scoring. In this work calculations were performed solely with Cartesian grid or cylindrical R-Z mesh (defined through USRBIN card), depending on the modelled experimental set-up. The scored quantity was the dose in water, in units of GeV/g per source proton with water density of $\rho = 1\ g/cm^3$ [Ferrari et al., 2011]. To obtain the absorbed dose in water in Gy per source proton, calculated values were multiplied by $1.60218 \cdot 10^{-7}$. To obtain the absorbed dose in water in Gy per 1 nA beam current, considered in **Chapter 3**, calculated values were multiplied by 10^{-3}, based on values from **Equation 1.12**.

Calculated single dose profiles (voxel by voxel) or integrated depth-dose profiles (slice by slice) were extracted either through the *flair* software [Vlachoudis, 2009], or via self-written tools to exclude human error in the data processing stage.

The statistical uncertainty of the scored quantities depends on the bin size and on the number of events occurring in a given bin. The former factor was adjusted to the experimental level of precision. The latter - the number of source protons - was adjusted to keep the statistical uncertainty level between $1 - 2\%$ of the scored quantities and ranged from $25 \times 6 \cdot 10^6$ to $25 \times 50 \cdot 10^6$, depending on the scoring geometry.

The FLUKA code enables parallel runs with different initial seed number to be merged during the data post-processing. All MC simulations were run simultaneously on $20 - 30$ cores at the time within the Polish Grid Infrastructure - an IT platform offering the extended amount of computational resources by over 230 $TFlops$ of computing power and more than 3600 TB of storage space with convenient access, large number of grid services and continuous effective technical support [`www.plgrid.pl`].

2.3.4. Mean excitation energy of material

FLUKA Material Database offers pre-defined materials and compounds, for the latter the specified Sternheimer parameters together with ICRU recommendations [ICRU37, 1984] for ionisation potential and composition are applied [Ferrari et al., 2011]. The material properties can be modified from the user-level. The parameter which is broadly discussed in the literature is mean excitation energy, I, which influences the stopping power of protons, according to **Equation 1.4**. **Figure 2.11** from [ICRU49, 1993] shows above 10 % variance of the mean excitation energy as a function of atomic number Z. Depending on the I-value definitions, calculated range differences up to 7.7 mm were found for 5% or 10% I-value variations [Besemer et al., 2013].

As for MC simulations run in this work mainly water phantoms were used, the I-value of water has been a concern. A wide range of values has been recommended in the literature, from 72.5 eV [Tan et al., 2004],through FLUKA-implemented value of

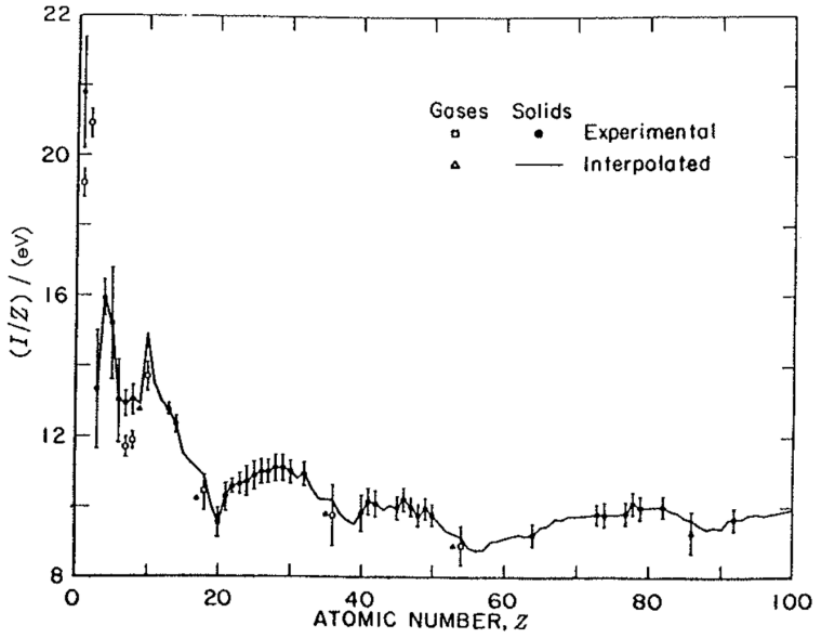

Figure 2.11. Mean excitation energy I as a function of atomic number Z. Reprinted from [ICRU49, 1993].

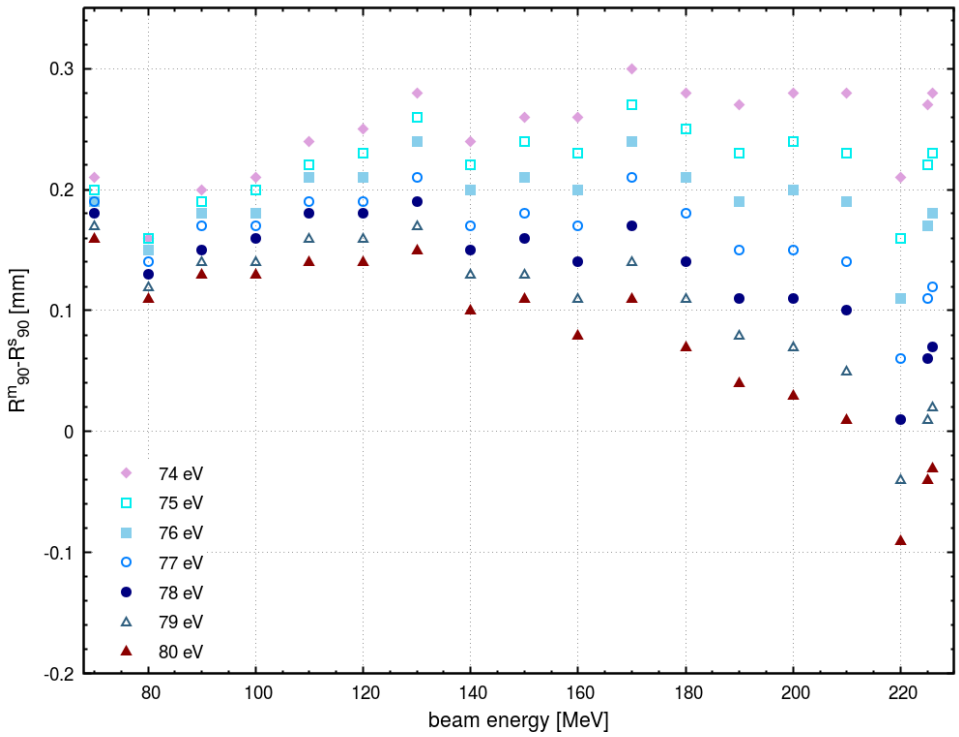

Figure 2.12. Difference between reference GTR3 measured (m) and simulated (s) range R_{90} for various water mean excitation energy simulated for the CCB proton beam nominal energies.

75 eV based on 75±3 eV ICRU value [ICRU37, 1984] [ICRU49, 1993], up to 80.8±2 eV by [Paul, 2007a] [Paul, 2007b]. The newest ICRU recommendations from [ICRU90, 2014] advise 78 ± 2 eV and it is even suggested for FLUKA-users to override current built-in value [Battistoni et al., 2016].

In [Sommerer et al., 2006] the mean excitation energy of water was redefined in the FLUKA code in order to adjust simulated beam range to the measured one (*ibidem* calculated in TRiP TPS for the same beam energy), concluding I-value of 80 eV for synchrotron-based HIT carbon ion beam. A similar investigation was done for the CCB facility within this work: depth-dose profiles were simulated in a water phantom for gantry nominal energy range $70 \div 220$ MeV each 10 MeV and water mean excitation energy between 74 eV and 80 eV. Pencil-beams were defined according to the developed MC GTR3 beam model, described in **Chapter 4.2.2**. Scored integral depth-dose profiles $IDD_4^{MC}(E, I)$ were integrated in slices of $r = 4.08$ cm every 0.2 mm. In **Figure 2.12** the difference between the measured (m) and simulated (s) BP ranges R_{90} is plotted versus nominal beam energy for different water I-values. The previously ICRU-recommended value of 75 eV for water mean excitation energy gives the smallest range shift between $0.16 \div 0.27$ mm, with the mean value of 0.22 $mm \pm 0.03$ $mm(SD)$. The highest differences were observed for 80 eV, between $-0.09 \div 0.16$ mm with the mean value 0.08 $mm \pm 0.07$ $mm(SD)$. A default value of 75 eV for water mean excitation energy was chosen for all of the MC simulations performed in this work.

Chapter 3

Modelling a passively scattered proton beam for the CCB eye melanoma treatment room

3.1. Introduction

In the first decade of this century dedicated medical cyclotrons with a maximum proton energy 230-250 MeV, such as Proteus C-235 from IBA or COMET from Varian, became commercially available. Reduction of energy extracted from cyclotrons is achieved by degrading the beam on absorber being a solid material inserted into the beam. Such mechanical degraders also reduce the beam current due to beam scattering, despite using low-Z solid materials, like graphite or boron. Transmission efficiency drops to a few percent for the lowest proton energy and maximisation of the treatment dose rate may become a crucial task. Therefore, for dedicated eye treatment rooms built at the new proton therapy facilities with high–energy cyclotrons (PSI in Villigen, Switzerland; CPO in Orsay, France; UFHPTI in Jacksonville, USA; WPE in Essen, Germany) methods of the beam forming developed for low energy cyclotrons could not be directly applied.

As described in **Chapter 1.5.1**, in the eye-line at the AIC-144 cyclotron the first scattering foil was placed 10 metres from the isocentre, which assured good beam uniformity. Such a solution was possible because a high incident current of about 20 nA of 60 MeV protons was available from the cyclotron and thus the clinical dose-rate between $21 \div 30$ Gy/min was easily possible [Swakon et al., 2010]. At the new CCB facility IBA (Ion Beam Application, Louvain-La-Neuve, Belgium) was responsible for providing the beamline to the eye treatment room according to the contract specification. The treatment unit was to be developed by the team of physicists and engineers from the Institute of Nuclear Physics PAN. For the IBA system the available beam current at 70 MeV was at the order of $1 \div 2$ nA, which required a careful beam opti-

misation in maximising the dose rate which become main issue in the development of the beam forming elements (*cf.* calculation in **Equation 1.13**).

Both, single and double scattering systems, characterised in **Chapter 1.4**, were investigated, and Monte Carlo simulations were applied to optimise the scattering setup of the new eye-line. In addition to dose maximisation, uniformity of the lateral profiles together with desired depth-dose beam parameters were taken into account in the optimisation procedure.

The calculations were performed in the following order. First, based on the measurements of the pristine Bragg peak, the Monte Carlo beam model of the ELTR was developed and quantitatively verified against both beam shape and absorbed dose. Next, various beam forming solutions were considered using single and double scattering approaches. The selected solutions were referenced with results of the measurements performed at the ELTR with current scattering system. The impact of the beam misalignment or distortion such as the beam shift or change in the spot size was discussed. This analysis allowed to quantify the advantages of single and double scattering techniques for beam formation at ELTR of CCB IFJ PAN.

3.2. Materials and methods

3.2.1. Depth-dose distribution measurements of the pristine ELTR beam

At the construction stage of the ELTR, systematic beam measurements were performed in order to experimentally determine the properties of the measured (m) unscattered ($unscatt$) pristine pencil beam, in particular:

- beam range ($R_{90}^{m,unscatt}$),
- spot size ($\sigma_x^{m,unscatt}$, $\sigma_y^{m,unscatt}$),
- beam divergence ($\theta_x^{m,unscatt}$, $\theta_y^{m,unscatt}$),
- absolute dose in water ($D_{H_2O}^{m,unscatt}$).

The results of those measurements were used to adjust the source parameters of the MC input file in order to obtain the MC beam model of the ELTR. **Figure 3.1** illustrates the set of the measurements obtained, resulting data sets with measured beam parameters and complementary geometry in the FLUKA code, described in the following subsections.

Beam range

During the beamline acceptance tests of the ELTR, the range of the unscattered pristine ELTR beam in water was determined by the measurement of relative depth-dose distribution with the Bragg Peak Chamber (BPC) IC, placed in *BluePhantom*^{2} filled with water (see **Chapter 2.1.4** for details). The phantom was positioned directly after the vacuum window with 1 cm air gap between the IGE (Ion Guide End) and the phantom wall. The IC was connected to a Common Control Unit (CCU) with integrated two-channel electrometer. The Beam Profile Monitor (BPM) output was also connected to the CCU with an entrance beam signal (BPM is located at the IGE). A collected signal was then calculated as relative dose in water, referenced as integral depth-dose distribution IDD^{BPC}. From this $IDD^{BPC}(70\ MeV)$ beam range $R_{90}^{m,unscatt}$ parameter was calculated at distal 90% after the BP maximum,

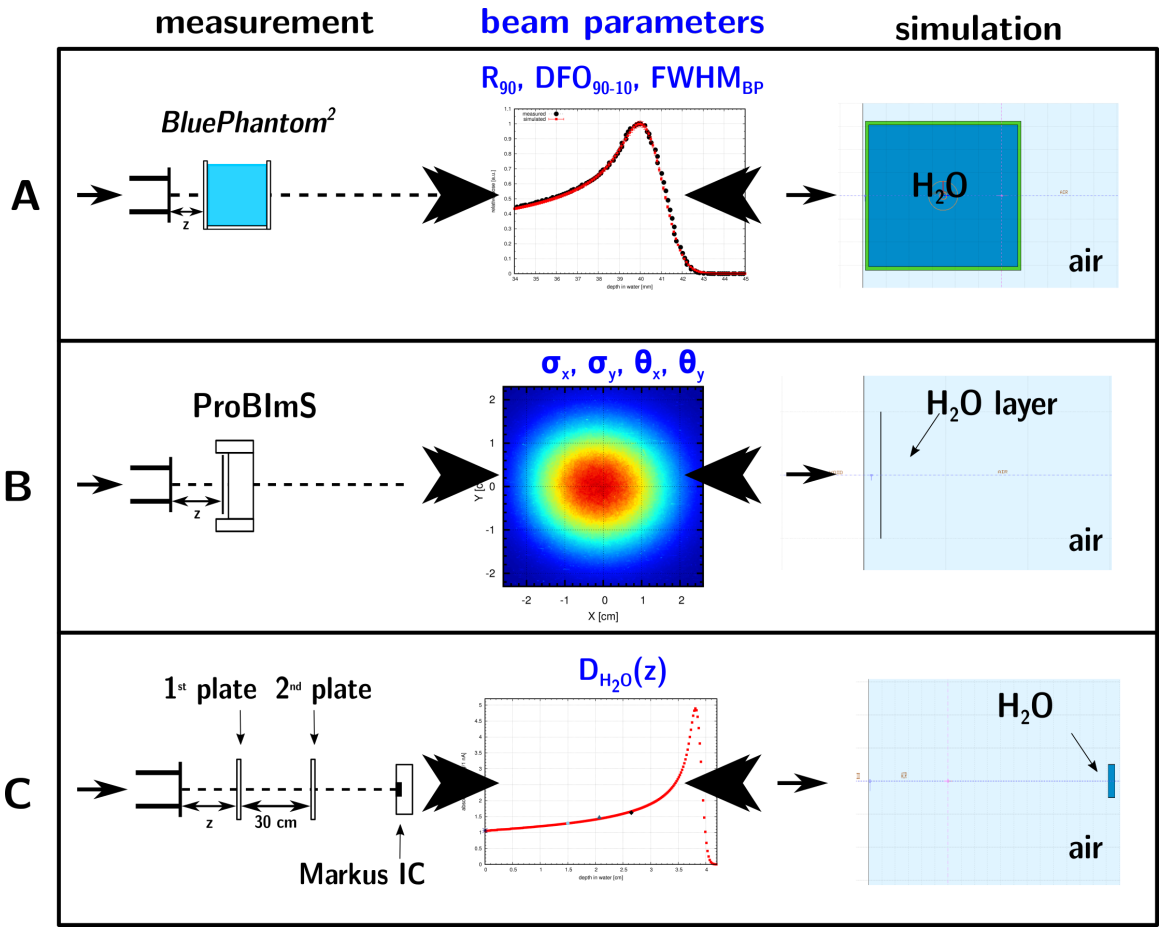

Figure 3.1. Measurement set-up of the pristine ELTR beam (left), corresponding MC simulation geometry (right) and compared beam parameters (middle).
A: Beam range measurements in a water-filled *BluePhantom*^{2} with BPC, with $z = 1.0$ *cm* after the IGE. Simulation geometry included water cube surrounded by PMMA walls.
B: Spot size measurements in air with ProBImS scintillator positioned at two distances from IGE: $z = 2.0$ or $z = 181.5$ *cm*. Simulation geometry included water layer in position corresponding to the scintillator screen of the ProBImS system.
C: Absorbed dose measurements with Markus IC positioned $z = 181.5$ *cm* from IGE, with beam scattered by two-set PMMA plates: first plate of 8 *mm* and second plate of 5, 10 or 15 *mm* PMMA. The first plate was positioned either $z = 40.0$ *cm* or 65.0 *cm* from IGE, with the second plate positioned 30.0 *cm* downstream. Simulation geometry included water phantom defined at $z = 181.5$ *cm* from IGE.

distal fall-off $DFO_{90-10}^{m,unscatt}$ as the distance between 90% and 10% dose level after the Bragg peak, and peak width $FWHM_{BP}^{m,unscatt}$ at the 50% dose levels of the BP. The left side of **Figure 3.1 A** illustrates beam range measurements.

Spot size

For the registration of lateral 2D images of the beam shape in-air, the ProBImS system [Rydygier, 2016] described in **Chapter 2.1.3** was used. The scintillator was positioned perpendicularly to the beam axis, in two positions (z):

- 2 cm from the IGE - at the beginning of the optical line,
- 181.5 cm from the IGE - close to the isocentre.

Spot images $I(x, y)$ were captured by CCD camera with 0.0256 $mm/pixel$ resolution. According to **Equation 2.2**, spot centre of mass $\overrightarrow{CM}$ was derived and 1D lateral spot profiles X and Y were extracted (**Equation 2.3**). By fitting 1D Gaussian curve (**Equation 2.4**), separately for X and Y profile, spot size described by $\sigma_x^{m,unscatt}(z)$ $[mm]$ and $\sigma_y^{m,unscatt}(z)$ $[mm]$ was calculated. The left side of **Figure 3.1 B** illustrates spot size measurements.

Beam divergence

The beam focusing point at the ELTR (so-called *waist*) was set at the IGE, resulting in only divergent beam inside the treatment room. Based on spot sizes $\sigma_x^{m,unscatt}$ and $\sigma_y^{m,unscatt}$ obtained from the spot lateral profiles X and Y, full-width at half-maximum ($FWHM$) values were calculated:

$$\begin{aligned} FWHM_x^{m,unscatt}(z) &= 2\sqrt{2ln(2)}\sigma_x^{m,unscatt}(z), \\ FWHM_y^{m,unscatt}(z) &= 2\sqrt{2ln(2)}\sigma_y^{m,unscatt}(z), \end{aligned} \tag{3.1}$$

for two distances z from the IGE: 2.0 cm and 181.5 cm. The relationship between the spot size in $FWHM$, and the distance, z, from the IGE was fitted using the function: $FWHM/2 = az + b$, for a being the tangent of the beam broadening angle $\theta/2$ and b being a free parameter. For small angles $\tan\theta/2 \approx \theta/2$, both $\theta_x^{m,unscatt}$ and $\theta_y^{m,unscatt}$ were calculated separately to describe the orientation value of the beam divergence.

Absorbed dose

For the preliminary mean dose measurement with the Markus IC, the beam was initially scattered to reduce dose uncertainties due to field inhomogeneities. Between IGE and PMMA holder for the IC, two PMMA plates were placed on the optical bench. Initially, the first plate was positioned at $z = 40.0$ cm from the IGE, mimicking range shifter with constant thickness of $d_1 = 8$ mm. The second plate was positioned 70 cm from IGE, with three various thickness of $d_2 = [5, 10, 15]$ mm alternatively installed as simulation of the range modulator scenario. In the second series of the measurements, the same plates were used with first plate positioned 65 cm from the IGE, and second plate at 95 cm from the IGE. The PMMA plates had the same thicknesses d_1 and d_2 as in the first measurement series.

In the PMMA holder, a Markus ionisation chamber TM23343 (PTW, Freiburg, Germany) was mounted and it was connected to the Unidos^{Webline} electrometer T10021

(PTW, Freiburg, Germany). The IC was positioned 181.5 cm from the IGE and centred at the beam axis. The relative intensity of the signal from the IC, referred later as $D^{m,unscatt}_{H_2O}(z, d_1, d_2)$, was then recalculated for a corresponding mean dose in water on the given depth depending on the total thickness of the PMMA plates $(d_1 + d_2)$. The PMMA water equivalent thickness $WET^{PMMA} = 1.16\ cm$ was calculated from **Equation 1.16** for PMMA density of $\rho = 1.18\ g/cm^3$ and total stopping power $S_{tot} = 9.31\ MeV\ cm^2/g$ from $PSTAR$ database, by NIST [Berger et al., 2009] for 70 MeV proton beam. The left side of the **Figure 3.1 C** illustrates absorbed dose measurements with the Markus IC.

3.2.2. Relative dosimetry methods at the ELTR

For the further development of the forming elements on the ELTR scattered beam, some dosimetric procedures for the beam verification were standardised. Two sets of beam data were collected:

- lateral profiles,
- depth-dose profiles.

Beam lateral profiles

1D lateral beam profiles X and Y were measured in-air with a rectifier diode 1N4007 connected to the Ergen electrometer as specified in **Chapter 2.1.3**. The measurements were performed 5.0 cm from the final collimator surface, 2.0 cm upstream from the isocentre (*i.e.* $z = 200.0\ cm$). The measured signal was normalised to the entrance beam monitor, located at $z = 12.5\ cm$ from the IGE, before the RS (beam monitors were not included in the simulated geometry shown in **Figure 1.12**).

The width of the lateral profile depends on the final collimator mounted on the snout, currently $\varnothing = 25\ mm$ or $\varnothing = 35\ mm$ in diameter. The profiles were normalised to the mean value from the central part of the profile $[-7.5\ mm : 7.5\ mm]$. For the normalised profiles, several beam parameters were evaluated:

- lateral beam width L^m_{95},
- field flatness F^m_{90},
- mean lateral beam penumbrae P^m_{mean},

according to the definitions given in **Chapter 1.3.2**, both for $\varnothing = 25\ mm$ and $\varnothing = 35\ mm$ beam collimator. The measurement resolution is estimated to 0.1 mm.

Depth-Dose Distribution (DDD)

Depth-dose distribution, DDD, was acquired in water with a Markus ionisation chamber TM23343 (PTW, Freiburg, Germany) connected to the Ergen electrometer, with the IC mounted in the in-house developed 3D-scanner as described in **Chapter 2.1.3**. The resolution of the chamber position is estimated to 0.1 mm with the read-out relative standard uncertainty of 2.3% assumed (*cf.* **Chapter 2.1.3**). The read-out was corrected for beam fluctuations, monitored by the entrance beam monitor.

From the DDD normalised at the BP depth, the following beam parameters were evaluated:

- beam range R^m_{90},
- distal fall-off DFO^m_{90-10},

- peak width $FWHM^m_{BP}$,
- $max/plateau^m$ ratio,

according to definitions given in **Chapter 1.3.2**.

3.2.3. Simulations of the pristine ELTR beam

All radiation transport calculations were performed using the FLUKA transport code. Input settings in FLUKA included HADROTHE(rapy) card option defining the physics of the particle transport, such as particle transport and energy cut-offs, type of followed particles etc., as described in detail in **Chapter 2.3.3**.

To build a MC beam model of the pristine ELTR beam, the consecutive simulations were performed:

- beam range simulations – to adjust beam energy and momentum spread source parameters (E^{MC}, $(dp/p)^{MC}$);
- spot size simulations – to adjust source spatial distribution (σ_x^{MC}, σ_y^{MC});
- beam divergence – to adjust source angular distribution (θ_x^{MC}, θ_y^{MC});
- calculation of absorbed dose in water ($D^{s,unscatt}_{H_2O}$).

The right side of **Figure 3.1** illustrates the FLUKA simulation geometry, depending on the measurement set-up of the ELTR pristine beam. From the above mentioned calculations, the simulation (s) beam parameters were derived:

- beam range R^s_{90},
- distal fall-off DFO^s_{90-10},
- peak width $FWHM^s_{BP}$,
- maximum to entrance dose ratio $max/plateau^s$ ratio,
- spot size of the unscattered pristine beam at given distance z from the IGE: $\sigma^s_x(z)$, $\sigma^s_y(z)$.

The extracted simulation parameters were referenced to the measured ones. By the trial and error method MC source parameters were tailored to fit the experimental values.

A simplified model of the ELTR room was defined in the FLUKA code. No room walls, floor or ceiling were included in the geometry, as their impact on the dose distribution was neglected. In the model, the beam source position was defined 290 cm from the IGE, in vacuum. The position of the virtual source in the FLUKA code was found empirically by adjusting the simulation results to the experimental data. The position of the virtual source did not overlap with *e.g.* the position of the focusing magnet or with the beam waist, set at the IGE point. A horizontal beam passed through the 50 μm thick Ti entrance window separating vacuum from the air space and positioned at the IGE. In all simulations, a water medium was used for absorbed dose scoring with density of $\rho = 1\ g/cm^3$ and 75 eV mean excitation energy recommended by [ICRU37, 1984], according to FLUKA Material Database [Ferrari et al., 2011], and examined in **Chapter 2.3.4**.

Beam range simulations

A cuboid phantom with the external dimensions of 67.5 $cm \times 56.0\ cm \times 64.5\ cm$ (XYZ) was positioned with the 1 cm air gap to the IGE. The dimensions of the water phantom correspond to the $BluePhantom^2$ specification [Dosimetry, 2013] with

1.5 cm thick PMMA walls of density $\rho = 1.19\ g/cm^3$, predefined in the FLUKA Material Database with compound parameters recommended by the ICRU [ICRU37, 1984]. The right side of **Figure 3.1 A** illustrates MC simulation geometry for the beam range adjustment. In parallel, water phantom of 67.5 $cm \times 56.0\ cm \times 64.5\ cm$ (XYZ) was simulated without PMMA walls, to verify the material influence on the BP shape.

The absorbed dose in water was scored along the beam axis in 0.1 mm slices of 4.08 cm radius what corresponds to spatial resolution of BPC measurements. Resulting IDD_4^{MC} was normalised at the Bragg peak maximum and $R_{90}^{s,unscatt}$ with $DFO_{90-10}^{s,unscatt}$ were determined. In the FLUKA code, beam energy E^{MC} was adjusted to reproduce the measured beam range $R_{90}^{m,unscatt}$. The source momentum spread $(dp/p)^{MC}$ was assumed to have the Gaussian distribution described by $FWHM$ and it was adapted to correspond with the measured distal fall-off $DFO_{90-10}^{m,unscatt}$. The simulated number of protons was 10^7 run in 25 parallel runs.

Spot size simulations

A thin water layer of 20 $cm \times 20\ cm$ size of 1 mm thickness was defined for spot size simulations referring to ProBImS spot measurements (*cf.* **Chapter 2.1.3**). The simulated detector size was much bigger than the scintillator dimensions to cover the low-dose envelope of the scattered beam far from the beam axis. The detector was positioned $z = 2.0\ cm$ or $z = 181.5\ cm$ from the IGE. The absorbed dose in water was calculated in $0.1\ mm \times 0.1\ mm \times 1\ mm$ (XYZ) voxels. The right side of **Figure 3.1 B** illustrates the MC geometry of the spot size simulations.

The beam was assumed to have zero direction cosines, with respect to OX and OY axes, respectively, and to run axially along the OZ axis. The spatial beam distribution was assumed to follow Gaussian distribution and σ_x^{MC} and σ_y^{MC} were adjusted. From the simulated 2D absorbed dose distribution $I^{MC}(x, y)$, 1D X and Y profiles were extracted through the point $P[0, 0]$ for two distances z from the IGE. For each profile, a Gaussian curve was fitted, assuming $(0, 0)$ position of the centre of the peak:

$$\begin{aligned} f(x, z) &= A_x \cdot \exp\left(\frac{-x^2}{2\sigma_x^{s,unscatt2}}\right), \\ f(y, z) &= A_y \cdot \exp\left(\frac{-y^2}{2\sigma_y^{s,unscatt2}}\right) \end{aligned} \tag{3.2}$$

for $z = 2.0\ cm$ or $z = 181.5\ cm$ distance from the IGE, with A_x, A_y normalised to the spot maximum value. $\sigma_x^{s,unscatt}$, $\sigma_y^{s,unscatt}$ were spot sizes obtained from the MC simulations and were compared to the measured values $\sigma_x^{m,unscatt}$, $\sigma_y^{m,unscatt}$. The simulated number of protons was 10^7 run in 25 parallel runs.

Beam divergence simulations

In the default input file of the FLUKA code, beam divergence is specified symmetrically with respect to X and Y axes. The spot measurements with the ProBImS system yielded an asymmetrical beam angular distribution. The customisation of the user routine called *SOURCE.f* in the FLUKA code allowed the definition of two separate independent Gaussian distributions of the angular spread from which proton direction cosines were randomised (by default only single Gaussian distribution

is available to describe the source angular spread). The derived values of the source angular distribution θ_x^{MC} and θ_y^{MC} were subsequently tailored to fit measured $\sigma_x^{s,unscatt}$ and $\sigma_y^{s,unscatt}$.

Calculation of the absorbed dose in water

For verification of the MC beam model of the ELTR, the absorbed dose in water $D_{H_2O}^{s,unscatt}$ was calculated in the FLUKA code for the unscattered pristine ELTR beam with the source parameters based on the above mentioned simulations (E^{MC}, $(dp/p)^{MC}$, σ_x^{MC} and σ_y^{MC}, θ_x^{MC} and θ_y^{MC}).

$D_{H_2O}^{s,unscatt}$, was scored in a cylinder with 0.265 *cm* radius and 5 *cm* length, in 0.02 *cm* slices *i.e.* with dimensions reproducing the active volume of the Markus IC. The cylinder was positioned axially, along the beam axis, with bases perpendicular to the beam. For Markus IC comparison, a dose ratio between simulation and measurements for pristine beam was calculated, and all dose results were multiplied by this ratio. The obtained depth-dose profile was compared to the absorbed dose measurements with two PMMA plates positioned in the beam path $D_{H_2O}^{m,unscatt}(d_1, d_2)$. The right side of **Figure 3.1 C** illustrates the MC simulation geometry of the DDD calculation. The simulated number of protons was 10^7 run in 20 parallel runs.

3.2.4. Constraints of the ELTR beam parameters

For CE marking of the ELTR room, the team led by Jan Swakoń, PhD, developed beam forming elements required to uniformly scatter the ELTR pristine beam. Beam shaping elements were adjusted to result in the required beam parameters of the scattered field. The constraints for beam parameters were defined based on experience gathered during exploitation of the eye treatment room at the AIC-144 cyclotron and validated during the acceptance tests of the ELTR room.

Table 3.1 specifies clinical requirements for lateral and depth-dose distributions measured in-air and in-water. The set of parameters combines (according to definitions given in **Chapter 1.3.2**):

- lateral dose distribution parameters:
  - L_{95} - field width at the level of 95%,
  - P_{mean} - lateral penumbrae between 90% and 10%,
  - F_{90} - lateral field flatness at 90%;
- depth-dose distribution parameters:
  - R_{90} - depth of the distal 90%,
  - DFO_{90-10} - distal fall-off between 90% and 10%,
  - $FWHM_{BP}$ - full-width at half-maximum (50%) of the BP,
  - $max/plateau$ ratio - ratio between dose maximum ($D(z_{BP})$) and plateau value at the entrance ($D(z = 0.2\ cm)$).

The ELTR scattering system was optimised to fulfil the clinical beam requirements. For the eye tumour irradiation ⌀25 *mm* beam collimator is sufficient but a broader beam width is useful for any type of the experiment *e.g.* radiobiological experiments with cells or mice, hence a ⌀35 *mm* beam collimator was also considered.

Table 3.1. Beam parameters constraints for in-air and in-water measurements at the ELTR of the CCB for $\varnothing = 25\ mm$ and $35\ mm$ beam collimator. [Courtesy of PTO]

Pristine Bragg peak	
range in water	$R_{90} = 31.8 \pm 0.2\ mm$
full-width-half-maximum	$FWHM_{BP} \leq 6.0\ mm$
distal fall-off	$DFO_{90-10} \leq 2.0\ mm$
Max to plateau ratio	$max/plateau \geq 3.5$
field $\varnothing 35\ mm$	
field width	$L_{95} \geq 30.0\ mm$
field flatness	$F_{90} \leq 5.0\%$
mean penumbra	$P_{mean} \leq 2.3\ mm$
field $\varnothing 25\ mm$	
field width	$L_{95} \geq 19.0\ mm$
field flatness	$F_{90} \leq 4.3\%$
mean penumbra	$P_{mean} \leq 2.1\ mm$

3.2.5. Symmetrised MC beam model of a pristine ELTR beam

In order to speed up the analysis of the scattering systems, a symmetrised MC beam model of the pristine ELTR beam was defined. Beam energy with momentum spread (E^{MC}, $(dp/p)^{MC}$) and source position were consistent with the MC beam model developed according to description of **Section 3.2.3**. The symmetrised spot shape was used, with averaged initial beam width σ^{MC}_{mean}, equal for both X and Y directions:

$$\sigma^{MC}_{mean} = \frac{\sigma^{MC}_{x} + \sigma^{MC}_{y}}{2}, \tag{3.3}$$

and averaged beam angular distribution, defined by θ^{MC}_{mean}:

$$\theta^{MC}_{mean} = \frac{\theta^{MC}_{x} + \theta^{MC}_{y}}{2}. \tag{3.4}$$

To confirm MC symmetrised beam model compatibility with the experimental data, current[1] commissioned [Horwacik et al., 2016] ELTR scattering set-up was redefined in the FLUKA code to model the measurement geometry from one of the early operational tests performed on *Dec.* 2015. In the FLUKA code, all beam forming elements except the range modulator were accurately defined, in order referring to geometry shown in **Figure 1.12**. No beam collimators or beam monitors present at the ELTR optical bench were taken into account in the simulation geometry and their impact was assumed to be negligible. The defined geometry of the beam shaping elements included:

- two *Ta* foils defined in single scattering mode: S1 of 50 μm thickness at $z = 5.0\ cm$ from the IGE and S2 of 25 μm thickness defined at $z = 60.0\ cm$ from the IGE,

[1] valid till *Sept.* 2018

- PMMA range shifter (RS) positioned at $z = 20.0\ cm$ from the IGE,
- PE biological shield as $50.0\ cm \times 42.5\ cm \times 40\ cm$ (XYZ) cube, axially hollowed out with $3.5\ cm$ diameter cylinder for the beam transport,
- final collimation steel snout of $18\ cm$ length with $\varnothing 40\ mm$ inner aperture and ended with brass collimator of $\varnothing 25\ mm$ aperture for lateral dose profiles measurements.

During the operational tests of the ELTR, a Markus IC TM23343 (PTW, Freiburg, Germany) connected to the Unidos^{Webline} electrometer T10021 (PTW, Freiburg, Germany) was used with IC mounted in the in-house developed 3D-scanner as described in **Chapter 2.1.3**. The DDD measurements were performed for $\varnothing 40\ mm$ beam collimator, starting from the isocentre. Lateral field profiles in-air were performed with a rectifier diode 1N4007 connected to the Ergen electrometer as specified in **Chapter 2.1.3** for $\varnothing 25\ mm$ beam collimator. The in-air measurements were performed $+5\ cm$ from the final collimator surface, *i.e.* $-2\ cm$ from the isocentre (and $z = 200.0\ cm$ from the IGE). The measurements precision was estimated to $0.1\ mm$ for both, lateral and depth profiles acquisition.

To simulate Markus IC measurements, a water tank of size $12\ cm \times 13\ cm \times 18\ cm$ (XYZ) was defined in the FLUKA code, corresponding to the 3D phantom dimensions described in **Chapter 2.1.3**. The mica entrance window impact was neglected in the simulations, as was the impact from the PMMA walls. The phantom proximal surface was positioned at the isocentre, according to the experiment geometry. 1D absorbed dose in water $D^s(z)$ was scored in $0.1\ mm$ steps in slices of $r = 0.265\ cm$ radius, up to $5\ cm$ depth. The calculations were run for $\varnothing 40\ mm$ beam collimator with no additional brass collimator mounted at the snout. The simulated number of protons was $10 \cdot 10^6$ run in 25 parallel runs.

For in-air lateral profiles calculation, a $1\ mm$ thick water layer of $12\ cm \times 12\ cm$ was defined at $z = 200.0\ cm$ from the IGE, *i.e.* $-2\ cm$ from the isocentre. The X profile $D^s(x, 0)$ was extracted from the 2D dose distribution as a central line of $1\ mm$ thickness in $0.1\ mm$ steps. The simulations were run for $\varnothing 25\ mm$ beam collimator. The simulated number of protons was $30 \cdot 10^6$ run in 25 parallel runs.

From the calculated lateral and depth-dose distributions, beam range R_{90}, distal fall-off DFO_{90-10}, peak width $FWHM_{BP}$, lateral field penumbrae P_{mean}, lateral field width L_{95} and lateral field flatness (F_{90}) were derived and compared with measured ELTR operational tests values.

3.2.6. MC evaluation of the ELTR scattering systems

Several components of the ELTR scattering system were predefined based on the earlier experience from eye-line in AIC-cyclotron as shown in **Figure 1.12**. The left side of **Figure 3.2** illustrates simulation geometry of the scattering system, including certain elements in their designated positions:

- scatterers, S1 and/or S2, as $10\ cm \times 10\ cm$ foils of variable thickness d (d_{S1} and d_{S2}, respectively);
- range shifter (RS) as $10\ cm \times 10\ cm$ PMMA plate of thickness adjusted to required R_{90} value, positioned at $z = 19.0\ cm$;
- biological shield as $50.0\ cm \times 42.5\ cm \times 40.0\ cm$ (XYZ) PE block, axially hollowed out with $3.5\ cm$ diameter cylinder for beam transport, positioned at $z = 63.0\ cm$;

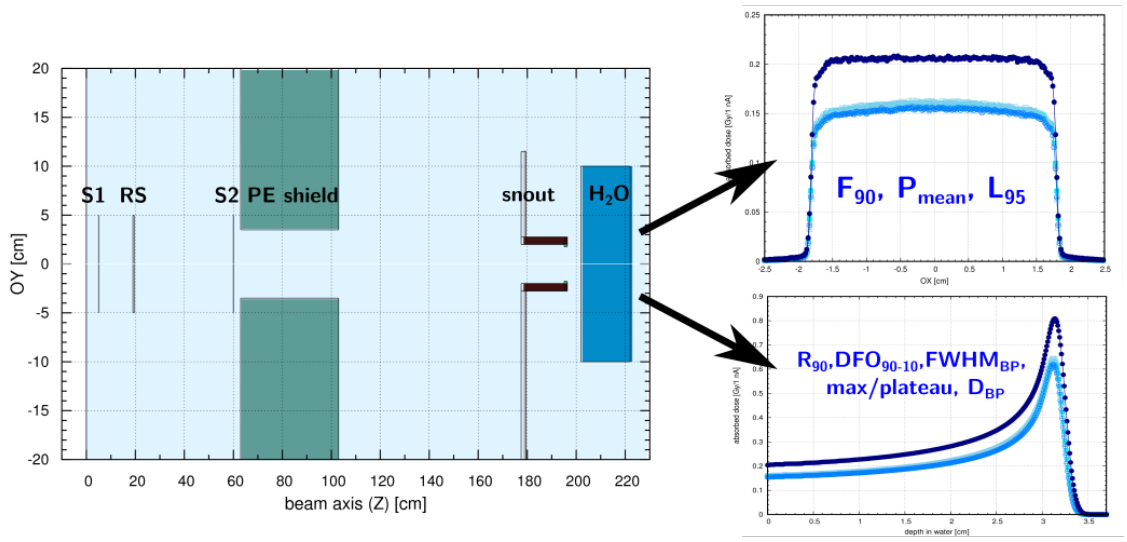

Figure 3.2. (left) Simulation geometry of the ELTR including first (S1) and second (S2) scatterer, range shifter (RS), PE neutron shield and final collimation (snout) ended with either $\varnothing 25$ or $\varnothing 35$ mm aperture collimator. Beam direction is from the left. Absorbed dose was scored in the water phantom, starting at the isocentre. (right) Extracted lateral (top) and depth (bottom) dose profiles from which characteristic beam parameters were assessed: field flatness F_{90}, mean penumbrae P_{mean}, field width L_{95}, range R_{90}, distal fall-off DFO_{90-10}, peak width $FWHM_{BP}$, $max/plateau$ ratio and maximum dose D_{BP}.

- final collimation steel snout of 18 cm length with $\varnothing 40$ mm inner aperture and ended with brass collimator of $\varnothing 25$ mm or $\varnothing 35$ mm aperture, positioned at $z = 177.5$ cm from the IGE.

While only pristine pencil-beams were simulated, the impact of a range modulator (RM) for the formation of the Spread-Out Bragg Peak (SOBP) was not considered at this stage of the study. No beam monitors or additional collimators were included in the considered set-up since they had no significant impact on the analysed beam parameters.

For scattering material of S1 and S2 tantalum foils were chosen based on experience from the AIC-144 eye treatment room [Swakon et al., 2010] and with positive outcomes from other eye treatment centres with Ta scattering system [Cirrone et al., 2004] [Hérault et al., 2005]. The possibilities of moving S1 and S2 on the optical bench were limited, due to presence of several other elements. In order to assure space for biological shielding against secondary neutrons, the scattering system was installed first $30 \div 60$ cm from the IGE.

The desired RS thickness was calculated in order to fulfil R_{90} parameter constraint given in **Table 3.1**. For this purpose the value of WER of the tantalum foils and air were calculated. Corresponding thickness of the PMMA range shifter was estimated according to **Equation 1.16**, with total stopping power taken from $PSTAR$ database, by NIST [Berger et al., 2009] for 70 MeV proton beam. In **Table 3.2** calculated WER values are given. As noticed in [Gottschalk, 2011], for water-Lexan recalculation the

Table 3.2. WER values calculated for various scattering materials. Data based on *PSTAR* database, by NIST [Berger et al., 2009] and the SRIM software (Stopping and Range of Ions in Matter) [`www.srim.org`].

material	$S_{tot}[\frac{MeV\ cm^2}{g}]$	$\rho\ [g/cm^3]$	WER
dry air	8.44	0.0012	0.0011
PMMA	9.31	1.19	1.16
tantalum	4.75	16.60	8.25

adopted equation gives good WER assessment, while for high-Z materials it becomes imprecise (*cf.* **Figure 1.4**). Therefore, values obtained from **Table 3.2** were treated as the first approximation of the required RS thickness, with further the trial and error method for RS thickness adjustment to fulfil R_{90} constraint.

Single and double techniques of the beam spreading were considered in the optimisation process. The scattering foils were characterised by the following parameters:

- for single scattering:
  - — scatterer material: *Ta* for both S1 and S2,
  - — scatterer size: 10 $cm \times 10$ cm foils,
  - — scatterer position: S1 at $z = 5.0$ cm from the IGE, S2 at $z = 60.0$ cm from the IGE (constant relative distance),
  - — changeable scatterer thickness d_{S1}, d_{S2};
- for double scattering:
  - — scatterer material: *Ta* cylinder surrounded by *PMMA*,
  - — scatterer size: PMMA disk of radius $R = 2.5$ cm with inner *Ta* cylinder of variable radius r_{S2},
  - — scatterer position: as S2 at $z = 60.0$ cm from the IGE,
  - — changeable scatterer thickness (independently D for PMMA and d for *Ta* components) and *Ta* radius r_{S2}.

The proximal surface of a cube water tank of 20.0 $cm \times 20.0$ $cm \times 20.0$ cm size (XYZ) was positioned at the isocentre, *i.e.* 202.0 cm from the IGE. Two scoring scenarios were evaluated to refer to the ELTR routine dosimetry methods:

- **lateral beam profiles**
  2D absorbed dose in water from entrance 1 mm water layer was calculated, X dose profile $D^s(x, 0)$ was extracted as central line of 1 mm thickness in 0.2 mm steps (bin size);
- **depth-dose profiles**
  1D absorbed dose in water $D^s(z)$ was scored in 0.1 mm steps in slices of $r = 0.265$ cm radius up to 5 cm depth.

Figure 3.2 illustrates the FLUKA simulation geometry with extracted 1D lateral and depth-dose profiles.

The simulated number of protons was adjusted to the simulation geometry (number of scatterers, number of materials to be crossed prior final scoring region) equal to $50 \cdot 10^6$ run in 25 parallel runs. This number of primary particles kept the statistical level of the results below 2% (1 SD).

Table 3.3. Foil thickness ranges of the analysed scattering set-ups for both single and double scattering method.

set-up type	1^{st} scatterer - **S1**	2^{nd} scatterer - **S2**
1 - S1 only	$d_{S1} = 20 \div 60\ \mu m\ Ta$ $\Delta d_{S1} = 10\ \mu m$	-
2 - $S1$ + $S2$	$d_{S1} = 25 \div 50\ \mu m\ Ta$ $\Delta d_{S1} = 5\ \mu m$	$d_{S2} = 20 \div 80\ \mu m\ Ta$ $\Delta d_{S2} = 10\ \mu m$
3 - S2 dual ring	-	$d_{S2} = 60 \div 90\ \mu m\ Ta$ disk with $r_{S2} = 3 \div 7\ mm$ $\Delta d_{S2} = 10\ \mu m$ with $\Delta r = 1\ mm$ each with $PMMA$ ring of $D_{PMMA} = 1$ or $1.5\ mm$ and $R_{PMMA} = 2.5\ cm$

In the further analysis, only the set-ups meeting requirements given in **Table 3.1** were considered. Each analysed scattering set-up fulfilled R_{90}, DFO_{90-10}, $FWHM_{BP}$ and $max/plateau$ ratio restrictions, hence these parameters were not taken into account in the optimisation process. The parameters of the lateral beam profiles, such as P_{mean}, L_{95} and F_{90}, were analysed to find the optimal scattering set-up. The additional, fourth parameter taken into the optimisation process was the dose. In simulations it was the maximum absorbed dose at the BP depth D^s_{BP} recalculated for 1 nA of the beam current $D_{BP}(1\ nA)$, according to **Equation 1.13** and description in **Chapter 2.3.3**.

3.3. Results

3.3.1. MC beam model of the pristine ELTR beam

Figure 3.3 shows IDD^{BPC} measured in water during the acceptance tests of the ELTR, compared to FLUKA MC simulation results. In the MC beam model of the pristine proton beam of the ELTR, beam energy E^{MC} and beam momentum spread $(dp/p)^{MC}$) were adjusted in such a way that R^s_{90}, DFO^s_{90-10} and $FWHM^s_{BP}$ parameters agreed with experimental values within $\pm 0.1\ mm$ (*cf.* **Table 3.4**). No significant influence of the phantom type (with PMMA walls or wall-less) on the beam parameters was found. IDD^{MC}_4/IDD^{BPC} ratio for both phantoms is shown in the insert plot of **Figure 3.3**. The maximum relative difference between simulated and measured curves around the BP did not exceed 5%.

Spot size agreed within $\pm 0.2\ mm$ (**Table 3.4**) was obtained for both X and Y profiles with one exception of σ^m_y at 181.5 cm with 1 mm difference (-10% of relative difference). Achieved agreement allowed to approve MC source parameters of beam spatial distribution (σ^{MC}_x and σ^{MC}_y) and angular distribution (θ^{MC}_x, θ^{MC}_y) obtained from the customised application of the *SOURCE.f* routine.

With verified free source parameters of the MC beam model (E^{MC}, $(dp/p)^{MC}$,

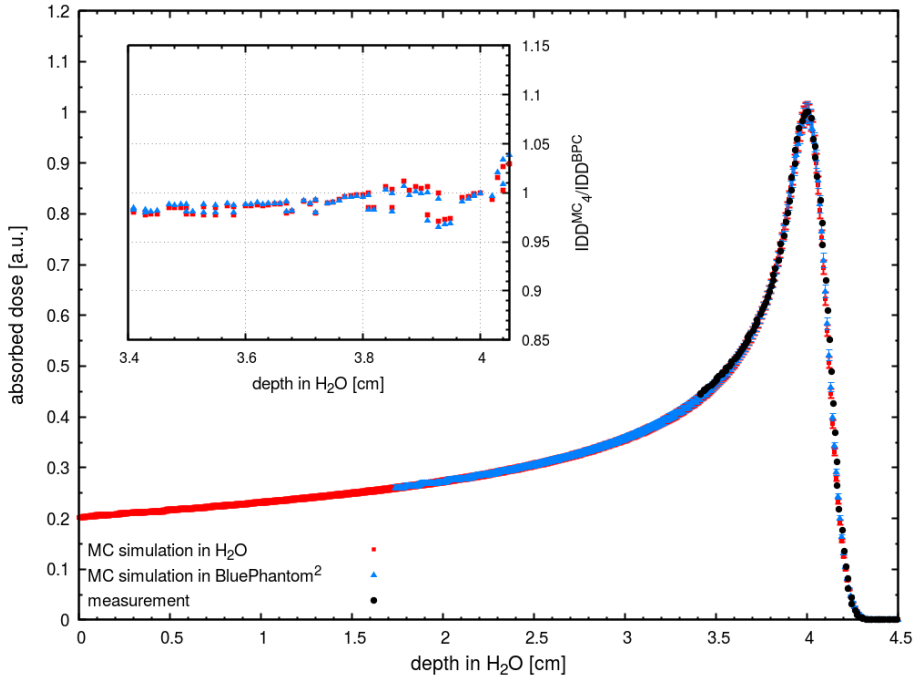

Figure 3.3. Depth-dose distribution of 70 MeV proton beam measured with BPC plane parallel ionisation chamber (IBA Dosimetry) in a water tank $BluePhantom^2$ during the acceptance tests of the ELTR (black dots). Corresponding results of calculations in the FLUKA code with the developed beam model of pristine beam is shown for $BluePhantom^2$ geometry (blue trianlges) and for water phantom geometry (red squares) with statistical uncertainty level below 2%. The insert plot shows the ratio between simulated IDD_4^{MC} and measured IDD^{BPC} for two geometries, with and without PMMA walls (blue triangles and red squares, respectively).

Table 3.4. Beam model verification parameters compared with in-air and in-water measurements for 70 MeV pristine proton beam of ELTR.

		measurement	**MC simulation**
Bragg peak in-water			
range	R_{90} $[mm]$	40.5 ± 0.1	40.5 ± 0.1
distal fall-off	DFO_{90-10} $[mm]$	1.6 ± 0.1	1.6 ± 0.1
peak width	$FWHM_{BP}$ $[mm]$	5.6 ± 0.1	5.4 ± 0.1
spot size in-air			
2 cm from IGE	σ_x $[mm]$	5.4 ± 0.2	5.3 ± 0.1
	σ_y $[mm]$	5.3 ± 0.2	5.2 ± 0.1
181.5 cm from IGE	σ_x $[mm]$	12.7 ± 0.5	12.8 ± 0.1
	σ_y $[mm]$	9.9 ± 0.5	10.9 ± 0.1

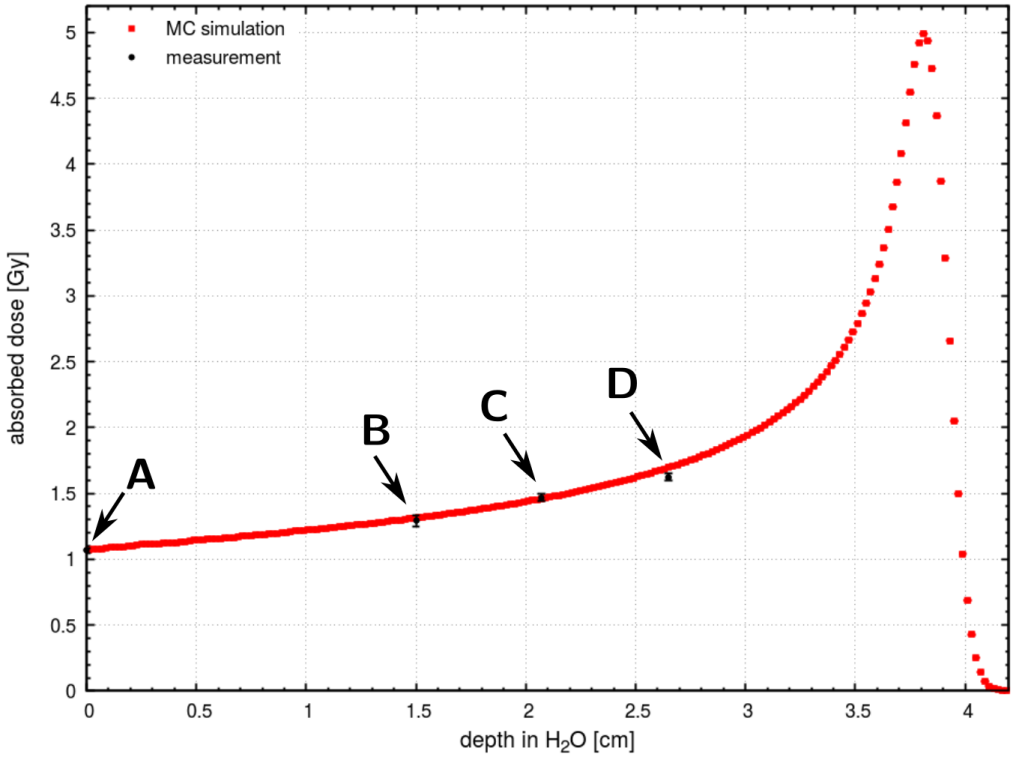

Figure 3.4. Absorbed dose in water simulated as a Markus chamber with MC beam model of the unscattered ELTR pristine beam (red squares). The measurements performed with Markus IC (black circles) were done for various scatterers set-ups, recalculated for corresponding depth in water (d)- A: pristine Bragg peak ($d = 0.00\ cm$); B: 1^{st} PMMA plate of 8 mm and 2^{nd} PMMA plate of 5 mm ($d = 1.50\ cm$); C: 1^{st} PMMA plate of 8 mm and 2^{nd} PMMA plate of 10 mm ($d = 2.07\ cm$); D: 1^{st} PMMA plate of 8 mm and 2^{nd} PMMA plate of 15 mm ($d = 2.65\ cm$). Detailed measurement and statistical uncertainties are given in **Table 3.5**.

σ_x^{MC} and σ_y^{MC}, θ_x^{MC} and θ_y^{MC}), the dose deposited by the unscattered pristine pencil beam was calculated in water. The resulting BP is shown in **Figure 3.4**. For dose comparison, measurements with the Markus IC in PMMA holder were recalculated for the corresponding depth in water. **Table 3.5** shows measured (m) and simulated (s) absorbed dose values $D_{H_2O}(z, d_1, d_2)$ with uncertainties. The relative dose difference of the absorbed dose simulations was found within $-2.3\% \div 8\%$ (calculated according to **Equation 2.7**).

Developed set of parameters complied with customised *SOURCE.f* routine was applied as a reliable MC beam model of the pristine ELTR beam.

3.3.2. Symmetrised MC beam model verification

Symmetrised MC beam model of the ELTR beam was defined by the source parameters: beam energy E^{MC}, beam momentum spread $(dp/p)^{MC}$ with averaged spot size (σ_{mean}^{MC}) and averaged beam angular distribution (θ_{mean}^{MC}). In **Figure 3.5** a qualitative

Table 3.5. Entrance mean dose measured with the Markus ionisation chamber ($D_{H_2O}^{m,unscatt}$) with various PMMA plates configurations recalculated for corresponding depth in water and compared with simulation results ($D_{H_2O}^{s,unscatt}$). Plates were mounted 30 *cm* from each other on the optical bench.

1^{st} plate distance from IGE	plates thickness $d_1 + d_2$	depth in water [cm]	$D_{H_2O}^{m,unscatt}$ $[Gy]$	$D_{H_2O}^{s,unscatt}$ $[Gy]$
40 cm	none	0.0	1.066 ± 0.021	1.066 ± 0.001
	8 mm + 5 mm	1.50	1.291 ± 0.045	1.302 ± 0.002
	8 mm + 10 mm	2.07	1.470 ± 0.025	1.447 ± 0.003
	8 mm + 15 mm	2.65	1.623 ± 0.027	1.665 ± 0.003
65 cm	8 mm + 5 mm	1.50	1.207 ± 0.074	1.302 ± 0.001
	8 mm + 10 mm	2.07	1.480 ± 0.026	1.447 ± 0.002
	8 mm + 15 mm	2.65	1.669 ± 0.029	1.665 ± 0.002

comparison of the spot images measured with the ProBImS system and calculated with the FLUKA code ar shown at the depth of $z = 2.0$ *cm*, prior to the first scattering foil. The spot shape irregularities, observed at the ProBImS image, result from the beam optics set-up of the ELTR, fixed by the IBA.

The symmetrised beam model was applied in the tested scattering system of the ELTR geometry, as described in **Section 3.2.5**. **Figure 3.6** in top shows comparison between the simulated and measured depth-dose distributions for ⌀40 *mm* beam collimator. FLUKA statistical uncertainty was below 2%. The maximum difference between simulation and measurement did not exceed ±5%, with the highest difference observed for the entrance region (**Figure 3.6**). The reason of discrepancy might be in the curve normalisation at the BP maximum (instead of the plateau normalisation), sensitive to the chamber positioning and read-out step. Moreover, for the pristine ELTR beam, the MC beam model was not validated for the plateau region while the measured *DDD* in water started from 3.4 *cm* depth due to the measurement through a $BluePhantom^2$ wall. The evaluated depth-dose beam parametersare given in **Table 3.6**. The agreement obtained was within 0.1 *mm*.

Dose lateral profiles measured with the rectifier diode and simulated with the symmetrised MC beam model for ⌀25 *mm* beam collimator are plotted in **Figure 3.6**. The FLUKA statistical uncertainty was below 2%. The plotted difference between simulation and measurement did not exceed ±5% in the flat field region and ±15% in the penumbrae region. The beam parameters of the lateral dose profiles are also given in **Table 3.6**. From the measurements data (m), mean value of the lateral dose profile penumbrae (P_{mean}^{m}), lateral field width ($L_{95,mean}^{m}$) and lateral field flatness ($F_{90,mean}^{m}$) were calculated. 1.1 *mm* difference was obtained for P_{mean} and 0.9 *mm* for the L_{95}. Difference in F_{90} reached 2.0%.

Symmetrised MC beam model of the ELTR was found appropriate for the ELTR

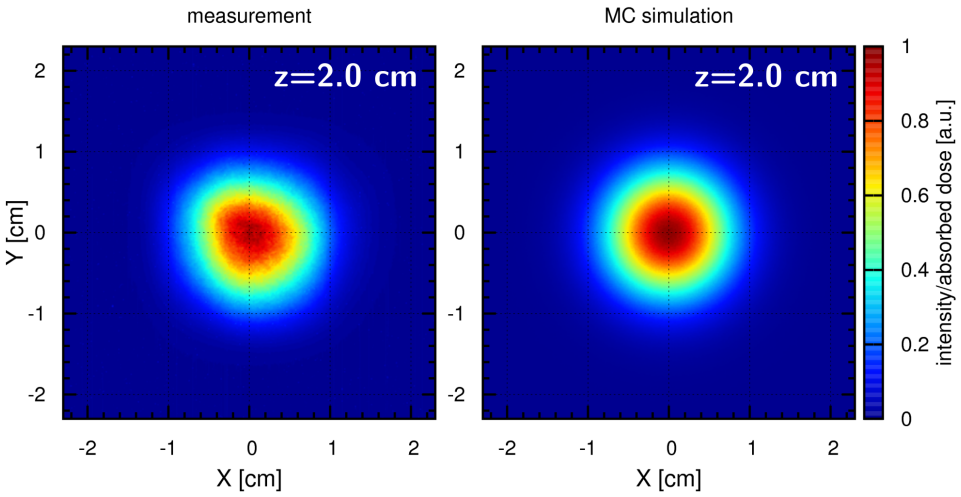

Figure 3.5. (left) 2D ELTR spot image acquired at $z = 2.0\ cm$ from the IGE, measured in-air with the ProBImS scintillator positioned perpendicularly to the beam. (right) Corresponding dose distribution from the FLUKA code at $z = 2.0\ cm$ from the IGE calculated with symmetrised MC beam model of the pristine ELTR beam.

beam model for the further evaluation of the scattering systems. In **Appendix A** the FLUKA input file of the symmetrised MC beam model of the ELTR is given.

3.3.3. Evaluation of the scattering systems for ELTR

With a symmetrised MC beam model of the ELTR, three different scenarios of the scattering set-ups for ELTR beam line were analysed, in total 87 set-ups. All of the evaluated scattering set-ups fulfilled the requirements of R_{90}, DFO_{90-10} and $FWHM_{BP}$, given in **Table 3.1**, which were not the subject of further optimisation. **her 3.7-3.10** show selected results, chosen to present parameter variation as a function of the scattering material thickness. For a single scattering system, the derived beam parameters are plotted as a function of the first scatterer S1 thickness for various second scatterer S2 layers. For double scattering (dual ring), the parameters are the function of the tantalum scatterer (S2) thickness, for various S2 radii and thickness of the PMMA occluding ring.

Mean penumbrae P_{mean} derived from the calculated lateral entrance profiles are presented in **Figure 3.7** with the constraint marked for $\varnothing 35\ mm$ beam collimator. For the single scattering system, mean penumbrae P_{mean} decreases with S1 foil thickness. For the double scattering system the trend is not so significant, however, smaller penumbrae are observed for thicker S2 foils. For $\varnothing 35\ mm$ beam collimator, mean penumbrae were found within $1.6 \div 2.8 \pm 0.2\ mm$ for single and within $1.1\ mm \div 3.4 \pm 0.2\ mm$ for double scattering system, with $P_{mean}(\varnothing 35\ mm) < 2.3\ mm$ constraint. All considered scattering geometries fulfilled the requirement of $P_{mean}(\varnothing 25\ mm) < 2.1\ mm$. The following set-ups have been excluded:

1. S1 scatterer (no S2) - $d_{S1} < 50\ \mu m$;
2. S1+S2 scatterers : for $d_{S1} = 25\ \mu m$, $d_{S2} \leq 30\ \mu m$

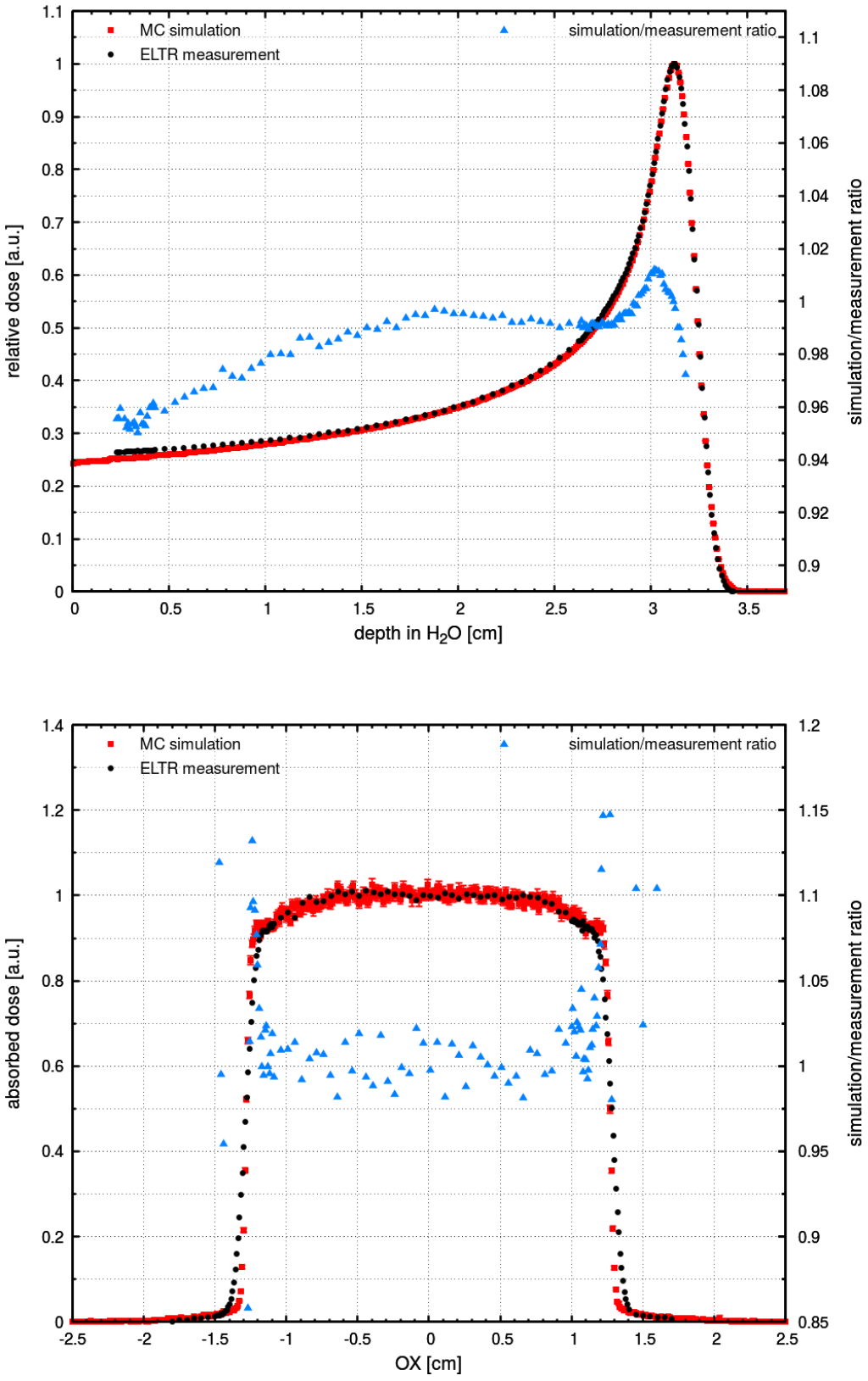

Figure 3.6. Comparison of the calculated and measured depth-dose profiles for $\varnothing 40\ mm$ beam collimator (top) and lateral dose profiles for $\varnothing 25\ mm$ beam collimator (bottom). Ratios between simulated and measured distributions are plotted with blue triangles. Evaluated measurement and simulation beam parameters are given in **Table 3.6** with uncertainties. [ELTR data - courtesy of PTO]

Table 3.6. Comparison of the beam parameters measured during the operational test of the ELTR and simulated in the FLUKA code with the symmetrised MC beam model of the ELTR. For the lateral profile parameters, averaged values of the peanumbrae P, lateral field width L_{95} and lateral field flatness F_{90} are calculated based on the X and Y profile analysis.

	measurement	**simulation**
Bragg peak		
$R_{90}[mm]$	31.8 ± 0.1	31.7 ± 0.1
$DFO_{90-10}[mm]$	1.6 ± 0.1	1.6 ± 0.1
$FWHM_{BP}[mm]$	5.6 ± 0.1	5.4 ± 0.1
$max/plateau$	3.8 ± 0.1	4.0 ± 0.1
$\varnothing = 25\ mm$ ***lateral profile***		
$P_{mean}[mm]$	1.9 ± 0.1	0.8 ± 0.1
$L_{95,mean}[mm]$	20.1 ± 0.1	21.0 ± 0.1
$F_{90,mean}[\%]$	3.6 ± 0.1	5.6 ± 0.7

3. S2 dual ring:
   - for 1 mm PMMA $d_{S2}(r = 3\ mm) = 60 \div 90\ \mu m$; $d_{S2}(r = 4\ mm) \leq 60\ \mu m$;
   - for 1.5 mm PMMA $d_{S2}(r = 3 \div 4\ mm) = 60 \div 90\ \mu m$, $d_{S2}(r = 5\ mm) \leq 60\ \mu m$.

Lateral field width at the level of 95% L_{95}, for $\varnothing 35\ mm$ beam collimator is shown in **Figure 3.8**. The scatterer thickness significantly influences the beam spreading in both methods. For the single scattering option $(1-2)$ this is a matter of the total S1+S2 thickness while the dual ring (3) depends on a combination of the scatterer thickness and radius. For $\varnothing 35\ mm$ beam collimator, field width L_{95} was found within $22.5 \div 30.4 \pm 0.2\ mm$ for single and within $23.0 \div 34.1 \pm 0.2\ mm$ for double scattering system with $L_{95}(\varnothing 35\ mm) \geq 30\ mm$ constraint. For $\varnothing 25\ mm$ beam collimator, field width L_{95} was found within $18.2 \div 24.2 \pm 0.2\ mm$ for single and within $17.2 \div 24.2 \pm 0.2\ mm$ for double scattering system with $L_{95}(\varnothing 25\ mm) \geq 19\ mm$ constraint. The following set-ups were excluded:

1. S1 scatterer (no S2) - $d_{S1} < 60\ \mu m$;
2. S1+S2 scatterers - $d_{S1} + d_{S2} > 80\ \mu m$;
3. S2 dual ring:
   - for both 1 mm and 1.5 mm PMMA ring thickness, radius below $r = 5\ mm$;
   - additionally, for 1 mm PMMA $d_{S2}(r = 5\ mm) \leq 50\ \mu m$;
   - for 1.5 mm PMMA $d_{S2}(r = 5\ mm) \leq 80\ \mu m$.

Lateral flatness at the 90% level F_{90} of the entrance lateral profile is presented in **Figure 3.9** for $\varnothing 35\ mm$ beam collimator. All studied cases fall into the given criteria of $F_{90}(\varnothing 35\ mm) \leq 5\%$. However, for $F_{90}(\varnothing 25\ mm) \leq 4.3\%$ constraint, almost none single scattering set-up could be accepted, with $F_{90}(\varnothing 25\ mm)$ of $4.7 \div 6.1\% \pm 0.6\%$. The only one accepted single scattering set-up with $F_{90}(\varnothing 25\ mm) = 4.3\%$ was with S1 foil of 25 μm *Ta* and S2 of 80 μm of *Ta*. Only a few dual ring set-ups meet the requirement, with $F_{90}(\varnothing 25\ mm)$ ranging between 3.4 and 6.2%. The smallest $F_{90}(\varnothing 25\ mm)$ values

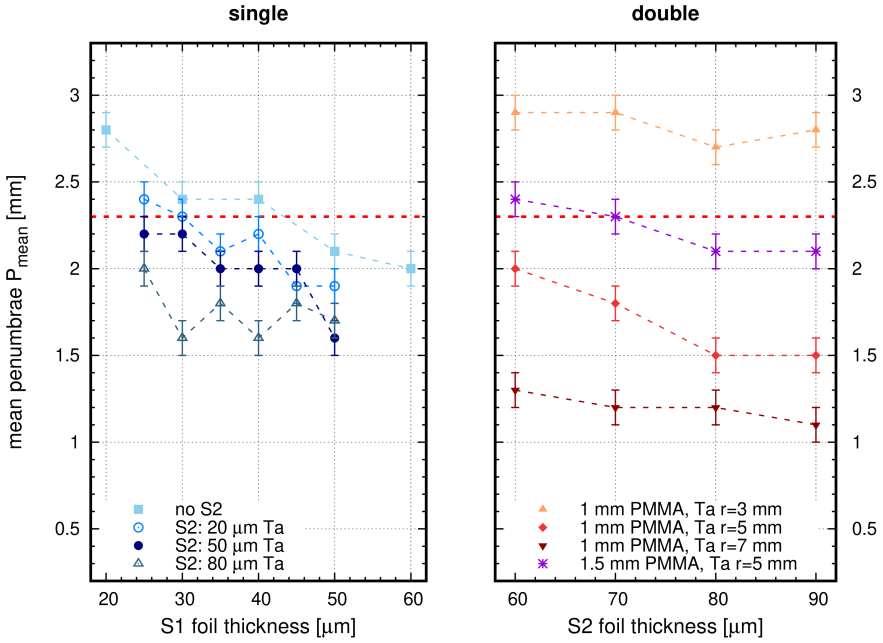

Figure 3.7. Mean penumbrae P_{mean} calculated for $\varnothing 35$ mm beam collimator for the selected single (left) and double (right) scattering set-ups. Horizontal dashed red line indicates the lateral penumbra constraint. The corresponding dotted lines are only guide to the eye.

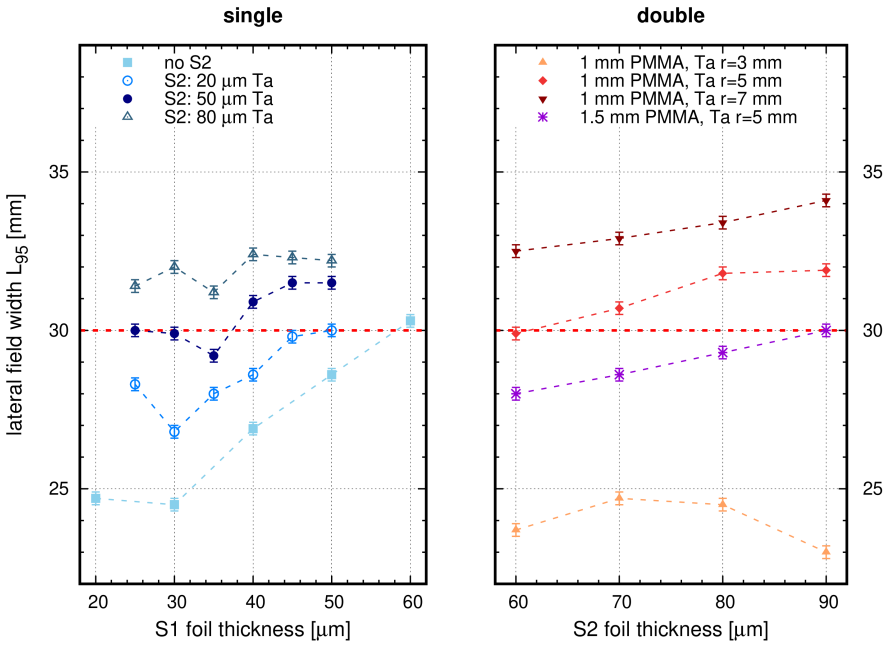

Figure 3.8. Lateral field width L_{95} calculated for $\varnothing 35$ mm beam collimator for the selected single (left) and double (right) scattering set-ups. Horizontal dashed red line indicates minimum field width L_{95} constraint. The corresponding dotted lines are only guide to the eye.

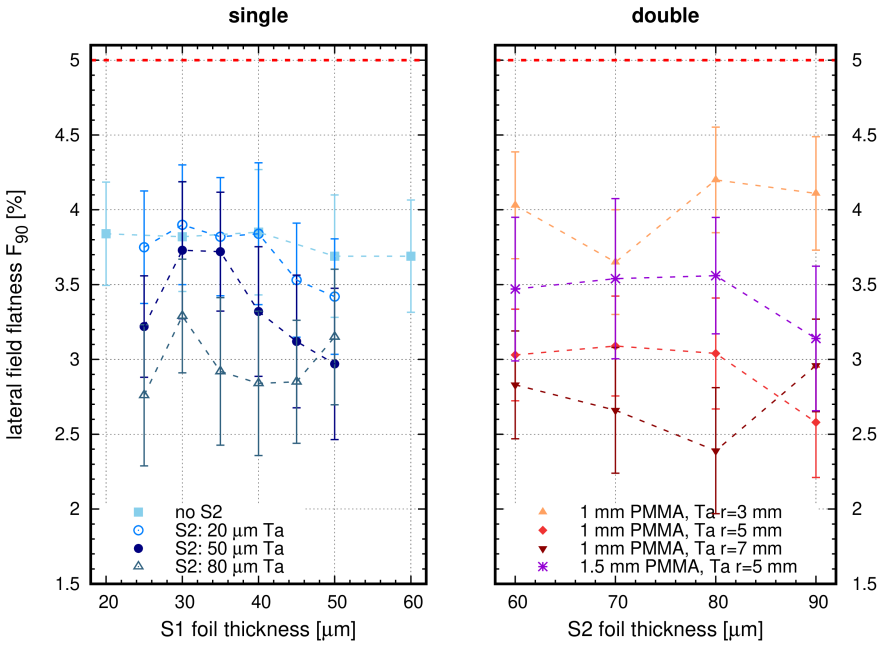

Figure 3.9. Lateral field flatness F_{90} calculated for $\varnothing 35\ mm$ beam collimator for the selected single (left) and double (right) scattering set-ups. Horizontal dashed red line indicates maximum field flatness F_{90} constraint. The corresponding dotted lines are only guide to the eye.

were obtained for 1 mm PMMA set-ups with $d_{S2}(r = 6\ mm) = 80 \div 90\ \mu m$ and $d_{S2}(r = 7\ mm) = 80 \div 90\ \mu m$. Taking into account large uncertainty of the field flatness parameter within $\pm 0.7\%$, the following set-ups were excluded for $F_{90}(\varnothing 25\ mm) > 5.0\%$ level:

1. S1 scatterer (no S2) - $d_{S1} < 60\ \mu m$;
2. S1+S2 scatterers - $80\ \mu m < d_{S1} + d_{S2} < 120\ \mu m$;
3. S2 dual ring:
   - for both 1 mm and 1.5 mm PMMA ring thickness, $r < 5\ mm$;
   - for 1.5 mm PMMA, $d_{S1}(r = 7\ mm) = 60 \div 90\ \mu m$;

Taking into account the considered set of the analysed beam parameters (P_{mean}, L_{95}, F_{90}) to be fulfilled according to requirements listed in **Table 3.1**, concomitantly for 35 mm and 25 mm beam collimator, some scattering set-ups can be distinguished:

1. S1 scatterer only (no S2)- $d_{S1} \geq 60\ \mu m$,
2. S1+S2 scatterers - $80\ \mu m < d_{S1} + d_{S2} < 120\ \mu m$;
3. S2 dual ring:
   - for 1 mm PMMA ring thickness, $d_{S1}(r = 6 \div 7\ mm) = 60 \div 90\ \mu m$;
   - for 1.5 mm PMMA ring thickness, $d_{S1}(r = 7\ mm) = 60 \div 90\ \mu m$.

For the above set of scatterers, the dose at the maximum of Bragg peak D_{BP} was recalculated to 1 nA beam current (see **Figure 3.10**). As the calculated dose in the FLUKA code is normalised per scoring unit volume (*cf.* **Chapter 2.3.3**), collimation size was irrelevant. For single scattering method, the thinner layer of the scatterer the higher dose in water, ranging between 0.50 Gy and 0.89 Gy with uncertainties (1 SD)

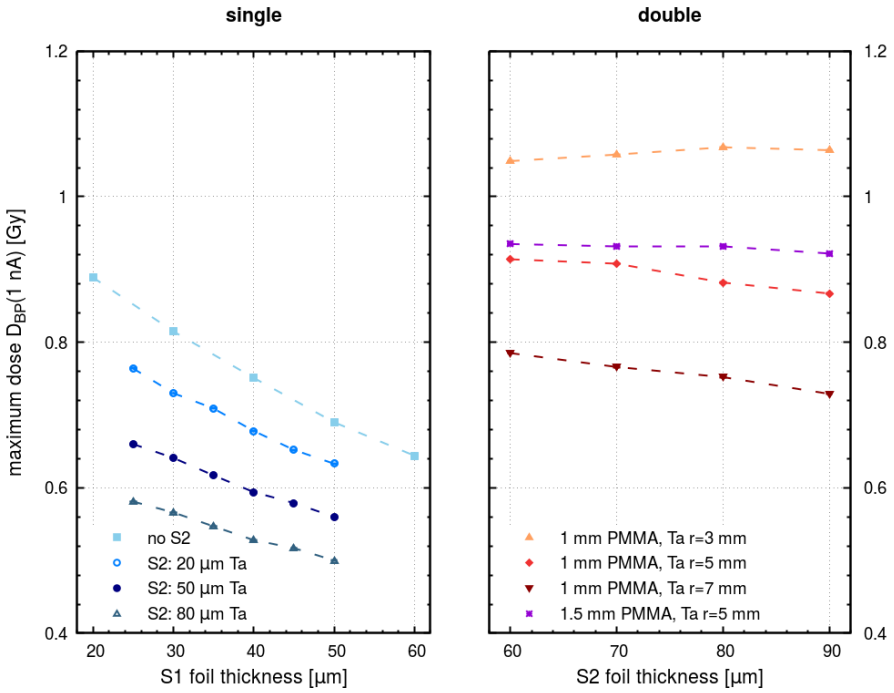

Figure 3.10. Absorbed dose at the Bragg peak depth D_{BP} recalculated for 1 nA beam current for $\varnothing 35$ mm beam collimator for the selected single (left) and double (right) scattering set-ups. The corresponding dotted lines are only guide to the eye.

between 0.05 Gy and 0.11 Gy. Higher doses were obtained for the double scattering system while only the central part of the beam was attenuated by the high-Z tantalum foil, ranging from 0.68 Gy to 1.07 Gy with dose uncertainties between 0.03 Gy and 0.12 Gy.

Finally, from the scattering set-ups $1-3$ specified in **Table 3.3**, solutions with maximum dose rate were selected by choosing the minimal required thickness of the Ta foil. These are:

1. S1 scatterer (no S2) - $d_{S1} = 60$ μm of Ta;
2. S1+S2 scatterers - $d_{S1} = 25$ μm with $d_{S2} = 60$ μm of Ta;
3. S2 dual ring - 1 mm PMMA ring with $r_{S2} = 6$ mm Ta disk of $d_{S2} = 80$ μm thickness.

In **Table 3.7** calculated beam parameters from lateral and depth-dose profiles are presented. In **Figures 3.11** the depth and lateral dose distributions corresponding to these scattering set-ups for $\varnothing 25$ mm beam collimator are presented, with dose recalculated for 1 nA of the beam current ($D(1\ nA)$. Mean lateral penumbrae P_{mean}, lateral field width L_{95} and field flatness F_{90} were within the constraints and comparable between the single and double scattering set-up. Moreover, the obtained beam parameters values were comparable with simulated current ELTR scattering system, given in **Table 3.6** with agreement within 1.1 mm and 2.0% for the field flatness. For maximum dose D_{BP}, when compared to the MC-simulated current ELTR scattering set-up, the relative dose difference reached 6%, 4% and 33% for scattering set-up 1, 2 and 3, respectively. Dose gain from double scattering set-up is visible in **Figure 3.11**.

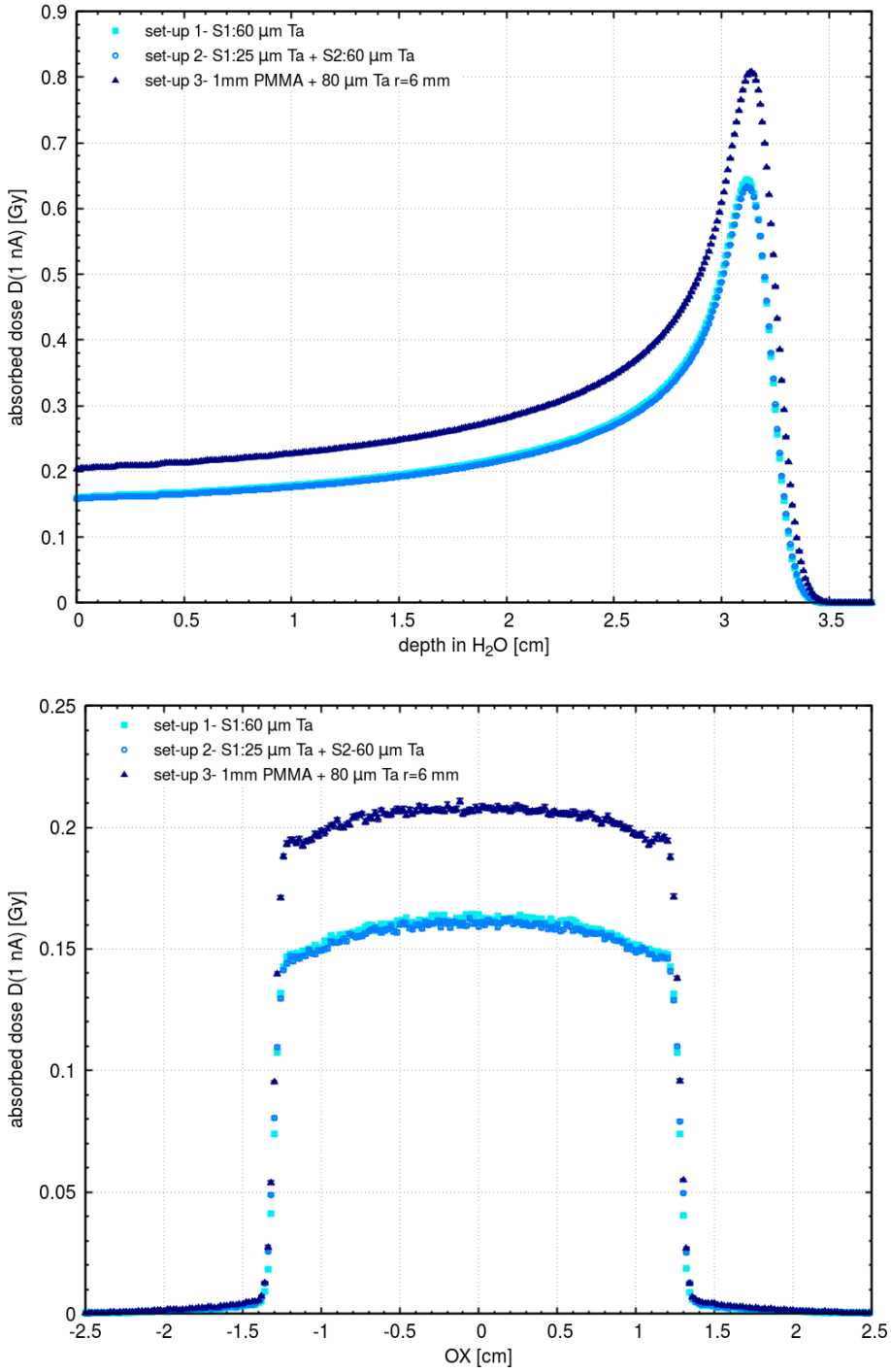

Figure 3.11. Depth-dose distribution (top) and lateral entrance profile for $\varnothing 25mm$ beam collimator for three scattering system solutions:set-up 1 (light blue squares) - S1 60 μm Ta foil; set-up 2 (hollow blue circles) - S1 25 μm Ta foil with S2 60 μm Ta foil; set-up 3 (dark blue trianlges)- 1 mm PMMA ring with $r_{S2} = 6$ mm Ta disk of $d_{S2} = 80$ μms. Statistical uncertainties (below 1%) are covered by the plot points.

Table 3.7. Beam parameters derived from the most favourable scattering set-ups. Set-up 1 - S1 60 μm *Ta* foil; set-up 2 - S1 25 μm *Ta* foil with S2 60 μm *Ta* foil; set-up 3 - 1 mm PMMA ring with $r_{S2} = 6$ mm *Ta* disk of $d_{S2} = 80$ μm for two beam collimators, $\varnothing 25$ mm and 35 mm with calculated uncertainties.

set-up	beam collimator	P_{mean} $[mm]$	$F_{90\%}$ [%]	L_{95} $[mm]$	$D_{BP}(1\ nA)$ $[Gy]$
1		2.0 ± 0.1	3.7 ± 0.4	30.3 ± 0.1	0.64 ± 0.08
2	$\varnothing 35$ mm	2.1 ± 0.1	3.1 ± 0.4	30.2 ± 0.1	0.63 ± 0.07
3		1.2 ± 0.1	3.1 ± 0.4	32.5 ± 0.1	0.81 ± 0.06
1		1.2 ± 0.1	5.0 ± 0.3	19.4 ± 0.1	0.64 ± 0.08
2	$\varnothing 25$ mm	1.3 ± 0.1	5.0 ± 0.4	19.2 ± 0.1	0.63 ± 0.07
3		1.1 ± 0.1	4.5 ± 0.4	22.0 ± 0.1	0.81 ± 0.05

3.4. Discussion

CCB at IFJ PAN is one of the proton facilities based on high-energy cyclotron, reaching energies up to 230 MeV. Maximisation of the dose rate in eye treatment lines of such facilities became an important issue, while the beam is mechanically degraded to obtain lower energies and its intensity is significantly reduced. The beam, being transported to the treatment room, passes through slits limiting the energy spread of the beam, which additionally decreases the beam intensity. Concomitantly, the eye treatment requires relatively high dose rates in order to shorten the irradiation time - a patient must gaze at the given point constantly when the beam is on. Among 11 eye cancer facilities around the world, the lowest maximum declared dose rate is 7 Gy/min from UCSF-CNL in San Francisco, USA, however this is for a low-energy based facility (67.5 MeV of accelerator energy) [Linz (ed.) and Kacperek, 2012]. The problem of the dose rate maximisation is new and unique for facilities with high energy cyclotrons and is infrequently described in the literature.

Beam degradation results in higher dose distal fall-off while the beam energy spread is raised by passing through the degrader. Lowering the distall fall-off is important due to critical structures of the eye, located at the distal part of the eye ball - optic nerve, fovea or optic disc [Bonnett et al., 1993]. The aim of the work presented in this chapter was to determine the most efficient, in terms of the dose rate, scattering systems for ELTR with simultaneous fulfilment of the other required beam parameter constraints (beam range and distal fall-off, BP width, field width, penumbrae, field flatness). For this purpose, Monte Carlo methods were applied.

In this section, several aspects of the eyeline optimisation are discussed:

- applicability of the Monte Carlo methods,
- utility of the MC beam model of the ELTR pristine pencil beam,
- foundation of beam parameters analysis (field width L_{95}, lateral field flatness F_{90}, lateral field penumbrae P_{mean} and maximum dose D_{BP}),
- scattering solution independent from the beam misalignment.

3.4.1. MC-based scattering system optimisation

The usage of the Monte Carlo methods in proton therapy is broadly referred [Seco and Verhaegen, 2016]. MC methods enable precise beam parameters calculation, such as dose distribution or beam scattering. Moreover, it can also be a useful tool for refinement of beam shaping elements. However, for construction of eye treatment rooms, customarily experimental approach and experience from the other facilities in operation were adopted until desired parameters levels were achieved [Hérault et al., 2005] [Cirrone et al., 2004] [Nauraye et al., 1995]. It has been shown, however, that MC simulations enable wider scope of the analysed geometries, extend dosimetric information where the measurements are problematic to carry out (*e.g.* small collimator sizes, neutron production), simultaneously sparing beam time [Hérault et al., 2005].

For calculation of eye treatment line, MC code MCNPX was tested for CAL (Niece, France) therapeutic beams and accepted to complement the beam measurements [Hérault et al., 2005]. With the GEANT4 toolkit, a MC tool for verification of the eye patient dose has been approved after a precise cross-check with IFNF-CATANA (Catania, Italy) ocular beam line [Cirrone et al., 2004] [Cirrone et al., 2003]. The FLUKA code used in this work has been selected for the first time for the ELTR eye line development.

The optimisation process of the scattering system is individual for each facility, depending both on the beam characteristics (beam current, beam energy, energy spread, beam size and shape, focusing point, beam direction and emittance) and technical aspects (treatment room geometry including distance between the exit window and the isocentre, required beam interlocks, etc.). A general method cannot be given, due to the large number of free parameters (distance of each element to the isocentre, its material, shape, size and function in the beam forming process). It can be, however, limited to several steps, as shown in early experimental optimisation of [Nauraye et al., 1995]:

- extraction of the beam parameters from the lateral and depth-dose profiles of the pristine beam,
- adjustment of the scattering foil thickness for lateral field broadening accompanied by desired beam range adjustment,
- adjustment of the scattering foil position for lateral penumbra sharpness and absorbed dose maximisation,
- improvement of the scattering foil shape for lateral field flatness.

Usually, considered scattering foil materials are lead, brass or tungsten [Nauraye et al., 1995], but also gold or tantalum are in use [Montelius et al., 1991] [Hérault et al., 2005] [Cirrone et al., 2004]. Typically, practical reasons impose the choice of the material (*e.g.* some of the materials turn out too thin to handle in given beam conditions [Montelius et al., 1991]). In this work tantalum foils were considered, accessible at CCB and following the scattering solutions from the other facilities [Cirrone et al., 2004] [Hérault et al., 2005].

From the survey of [Hrbacek et al., 2016] out of 10 participating centres only 2 have double scattering system, the remaining 8 use the single scattering technique for beam broadening. The applied system depends on the primary beam conditions, such as

beam size and emittance imposing required scattering solution. In this work, a single scattering set-up was considered due to PTO team experience in handling such a beam, gained during operation of the treatment room at the AIC-cyclotron facility. Moreover, such a solution is also more secure in case of beam misalignment [ICRU78, 2007]. This issue could not be ignored at the beginning of work at ELTR with very limited statistics on beam stability. The single scattering system, described in **Section 3.2.5**, is now in use for the ELTR treatments [Horwacik et al., 2016]. Additionally, double scattering solution for the ELTR scattering system was also analysed in the simulations.

Another challenge was the maximisation of the absorbed dose as a consequence of the large beam degradation of the 70 MeV proton beam, which is easily achievable with double scattering technique as a smaller fraction of the beam is cut out by collimators. The occluding ring technique, proposed in [Koehler et al., 1977], requires large field formation distance and gives lower beam intensity when compared to dual ring technique [Takada, 1994]. The dual ring method used in this work was also found easier when compared to the sophisticated contoured scatterer method proposed by [Grusell et al., 1994] [Gottschalk, 2011] which, however, also requires good knowledge and reproducibility of the beam shape.

Position and the order of the beam forming elements on the optical bench was designed by PTO team and was not a subject of optimisation, though alternative scenarios separating beam scattering and beam modulators might be advantageous in terms of the analysed beam parameters. Typically, the beam is first broadened via the scattering foils, then degraded and modulated for a given tumour conditions, *e.g.* [Montelius et al., 1991] [Bonnett et al., 1993] [Hérault et al., 2005] [Swakon et al., 2010]. This approach also limits the influence of the additional scatterers (as ionisation chambers, range shifter or range modulator) on the final beam shape [Takada, 1994]. On the other hand, it has been experimentally shown by [Bonnett et al., 1993] that increasing the distance between the range shifter with a range modulator and the isocentre results in sharper lateral beam penumbrae. Additionally, this study has shown that the penumbra value remains invariable to the effective PMMA thickness in the beam path from RS+RM combination. Furthermore, by the increment of the second scatterer-to-isocentre distance, smaller energy loss is obtained [Takada, 1994]. Thus, installing beam spreading and beam modulating elements at the beginning of the optical bench, close to the IGE as considered in this work, ought to result in sharper and stable beam penumbrae and higher dose. Moreover, it should limit the undesirable additional dose from the scattered radiation [Stolarczyk et al., 2010]. The drawback of the tested set-up (**Figure 3.2**) was interspersed beam scattering and forming when compared to the scattering set-ups of the other facilities where beam is first scattered then modulated, *e.g.* [Cirrone et al., 2004] [Montelius et al., 1991]. However, the reverse order of the elements (beam modulation followed by the beam scattering) was also applied [Nauraye et al., 1995] with customised elliptical second scatterer designed to improve the lateral field flatness.

3.4.2. MC beam model of the ELTR beam

The MC model was verified with the measurements data in terms of beam size (σ_x^m, σ_y^m), beam range (R_{90}^m), distal fall-off (DFO_{90-10}^m) and BP width ($FWHM_{BP}^m$),

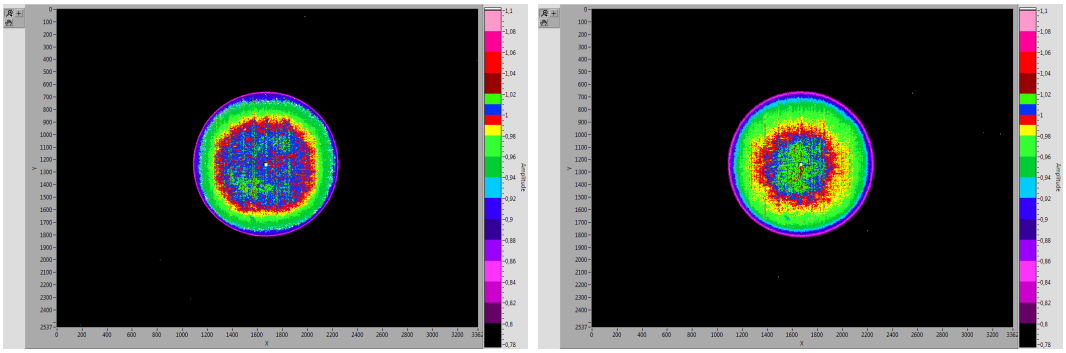

Figure 3.12. 2D beam images of the scattered, axially extracted ELTR beam, captured with CCD-based ProBImS system, at 5 (left) and 20 *cm* (right) from the final collimator surface (−2 and 13 *cm* from the isocentre) with ⌀25 *mm* beam collimator. The images were captured on the XY plane (in pixels) perpendicular to the beam axis, with the scintilator intensity colour scale (the right side of each image) described in [Rydygier, 2016]. [Courtesy of PTO]

as shown in **Table 3.4**. ±0.1 *mm* agreement was found, with exception for σ_y at 181.5 *cm* where the difference of 1 *mm* was obtained. The reason for the discrepancy is associated with beam width variations during that measurement session and spot rotation (*cf.* description given in **Chapter 1.3.1**). This post rotation was not included in the XY profile analysis, but is visible in **Figure 3.5** at $z = 2.0$ *cm* measuring distance from the IGE. Moreover, in the measurements of spot size, 1D profiles of 0.0256 *mm* were extracted for σ_x^m, σ_y^m calculation from the ProBImS system – such narrow read-out without any averaging method is sensitive for any beam fluctuations, biasing measured value of the spot size.

The description of the proton source in the FLUKA code enables direction cosines to be defined in reference to the beam axis. For the ELTR beam model it was assumed to be zero, both with respect to OX and OY axes (**Section 3.2.3**). The reason was one of the ELTR daily QA procedures, in which beam direction is set to be extracted axially along the optical bench inside the ELTR. In **Figure 3.12** two images captured with ProBImS system during such procedure are shown, in 5 *cm* and 20 *cm* from the final collimator surface (*i.e.* −2 *cm* and 13 *cm* in reference to the isocentre). Symmetrical distribution of the beam can be qualitatively seen. Thus, analysis of the beam obliqueness was excluded from the considerations presented within this work. As noticed in [Takada, 1994], particle fluence distribution is more sensitive for a large beam emittance, something which is not the case of the ELTR. Still, beam misalignment may lead to the field flatness distortions particularly for the double scattering technique, which is discussed in **Section 3.4.4**.

The ELTR proton beam waist was steered at the IGE point. Thus in the MC beam model of the ELTR, only a divergent beam was considered. Similar beam focus point was reported in other eye tumour facilities, *e.g.* in CPO (Orsay, France) [Nauraye et al., 1995]. Such a type of the beam is typical for scattering systems, in contrast to beam waist shifted towards the patient and sensitive to the focusing magnets stability. It has been shown, however, that a convergent beam impinging on the scattering foil

Table 3.8. Beam parameters derived from the most favourable scattering set-ups. Set-up 1 - S1 60 μm *Ta* foil; set-up 2 - S1 25 μm *Ta* foil with S2 60 μm *Ta* foil; set-up 3 - 1 mm PMMA ring with $r_{S2} = 6$ mm *Ta* disk of $d_{S2} = 80$ μm for $\varnothing 25$ mm beam collimator with calculated uncertainties.

set-up	R_{90} $[mm]$	DFO_{90-10} $[mm]$	$FWHM_{BP}$ $[mm]$	$max/plateau$ **ratio**
1	31.7 ± 0.1	1.6 ± 0.1	5.3 ± 0.1	4.0 ± 0.1
2	31.7 ± 0.1	1.6 ± 0.1	5.3 ± 0.1	4.0 ± 0.1
3	31.9 ± 0.1	1.7 ± 0.1	5.5 ± 0.1	3.9 ± 0.1

results in a smaller field inhomogeneity [Takada, 1994]. In these terms, the considered scattering set-ups might result in higher dose rate with preserved or improved field flatness. In this work it has been omitted due to a lack of experimental data needed for the verification of parameters defining a convergent beam within the FLUKA code.

The symmetrised MC beam model with a beam size of σ^{MC}_{mean} and beam angular spread described by θ^{MC}_{mean} was used for the analysis of scattering system set-ups. As shown in **Figure 3.6** and **Table 3.6**, simulation results follow the measurement data with ± 1.1 mm agreement, with a maximum difference for the lateral penumbrae (P_{mean}). Differences in penumbrae might result from the diode positioning. When P_{mean} was calculated for $z = 207.0$ cm, results agreed with measured ones: ($P^{s}_{mean} = 2.0 \pm 0.2$ mm). Moreover, the absorbed dose was calculated in a thin water layer, while the measurements were performed in air. For the detailed analysis of the chosen scattering set-ups, separate non-symmetrical spot size and angular spread would be required, which was beyond the scope of this work.

3.4.3. Evaluated beam parameters

From the analysed scattering set-ups, lateral profiles were calculated both for $\varnothing 25$ and $\varnothing 35$ mm beam collimator. As combined in [Linz (ed.) and Kacperek, 2012], in **Table** 10.2 diameter of the beam collimator depends on the occurring tumour size in the given region and, for some facilities, additional research activities require broader beam. From the experience gathered at the AIC-cyclotron facility, $\varnothing 25$ mm is sufficient for ELTR patients, though $\varnothing 35$ mm beam profiles are also checked.

In this work requirements on the beam parameters might be artificially divided into two groups: fixed and and optimised beam parameters.

Fixed beam parameter should be possibly invariant and changes in the scattering foil thickness or shape should not significantly influence those beam parameters. These are: beam range R_{90} fulfilled by RS thickness adjustment, distal fall-off DFO_{90-10}, Bragg peak width $FWHM_{BP}$ or $max/plateau$ ratio. They are difficult to compare with other facilities, while they depend on given beam characteristics, needs and opportunities of a given site. Moreover, discrepancy in parameters calculation or lack of definition of given parameter assessment is observed. In **Table 3.8** the depth-dose parameters for the selected scattering set-ups $1 - 3$ are shown.

From **Table** 10.1 in [Linz (ed.) and Kacperek, 2012] the maximum range of the

proton beam in water or eye tissue ranges between 28 mm (AIC-based IFJ PAN treatment room) and 40.5 mm (at 90% of SOBP - CPO, Orsay, France). In ELTR $R_{90} = 31.8 \pm 0.2\ mm$ was set as it covers practically all depths of the eye tumours [Kacperek, 2009].
Dose distal fall-off DFO_{90-10} depends mainly on the initial beam degradation required to fulfil R_{90} constraint. For low-energy cyclotron-based facilities DFO_{90-10} is smaller (*e.g.* 0.9 mm in CAL, Niece, France [Hérault et al., 2005]), and for high energy beams it has a bigger energy spread resulting in higher DFO_{90-10} (*e.g.* $2.1 \pm 0.1\ mm(1\ SD)$ in CPO, Orsay, France [Nauraye et al., 1995], 3.2 mm in UFPTI, Jacksonville, USA [Slopsema et al., 2013], or 6.6 mm at MGH, Boston, USA [Linz (ed.) and Kacperek, 2012]) including $DFO_{90-10}(\varnothing 35\ mm) < 2.3\ mm$ constraint of the ELTR.
$Max/plateau$ ratio is difficult to compare between the facilities, since it is sensitive to the measurement set-up, such as size of the measuring chamber or final collimator-to-water surface distance. For all analysed set-ups $(1-3)$ $max/plateau$ ratio was above the constraint of 3.5, with a minimum value of 3.63, which is comparable with other facilities (*e.g.* 3.81 mm in UCSF, San Francisco, USA [Daftari et al., 1996] or 3.6 mm in CPO, Orsay, France [Nauraye et al., 1995]). For the irradiation of the eye ball, where beam passes typically only through aquenous humour, no additional dose delivered to the preceding healthy tissues must be considered (comparing to other PT-treated lesions where the $max/plateau$ ratio is more strictly maximised).

The width of the unmodulated Bragg peak, $FWHM_{BP}$, also depends on the initial beam degradation, however too thick scattering foils result in the surpassing the reference level ($FWHM_{BP} < 6\ mm$). Reported values ranged between 3.2 mm (CAL, Niece, France – $65MeV$ cyclotron [Hérault et al., 2005]) and 5.0 mm (UCSF, San Francisco, USA –67.5 MeV cyclotron [Daftari et al., 1996]).

Optimised beam parameters in this work included lateral field width L_{95}, lateral field flatness F_{90}, lateral field penumbrae P_{mean} together with maximum dose at the BP depth $D_{BP}(1\ nA)$ for two beam collimator sizes of $\varnothing 25$ or $\varnothing 35\ mm$. Similar main beam parameters given in the literature, apart from depth-dose beam parameters, are lateral field penumbrae, lateral field width, field symmetry/uniformity or flatness and dose (dose rate). Still, comparison is problematic due to differences in the measurement set-up (profiles acquired in air, in Perspex or at the entrance depth of a water phantom). Sometimes there is a lack of precise parameter definitions or discrepancies in parameter evaluation (*e.g.* not specified collimation width for reporting the penumbra, not specified flatness calculation method). **Table 3.9** presents the main beam characteristics of the world-wide eye tumour facilities based on the high-energy accelerators (isochronous cyclotrons or synchrocyclotrons) compared with calculated parameters averaged from set-ups $1-3$ ($\varnothing 25\ mm$ beam collimator). Field width and flatness were omitted due to a lack of corresponding data. In order to compare current results with the literature data, mean penumbrae value was calculated between 80% and 20% of the normalised lateral dose profile. MC-calculated ELTR values features comparably small DFO_{90-10} and superior lateral dose fall-off (P^{mean}_{80-20}) - the lowest from world-class facilities. The ELTR dose rate value was measured during the operational tests with current ELTR scattering system, described in **Section 3.2.5**. Taking into account that higher doses were obtained for MC scattering set-ups $1-3$, estimated

Table 3.9. Beam parameters of eye-lines based on high-energy cyclotrons or synchro-cyclotrons [Linz (ed.) and Kacperek, 2012] [Slopsema et al., 2013]. For ELTR data, averaged beam parameters from the most favourable set-ups $1-3$ are given for $\varnothing 25\ mm$ beam collimator.

	Acc. energy $[MeV]$	**Room energy** $[MeV]$	DFO_{90-10} $[mm]$	P_{80-20} $[mm]$	**dose rate** $[Gy/min]$
UFPTI, Jacksonville, USA	230	105	3.2	1.1	≥ 30
CPO, Orsay, France	200	76	2.3	1.9	$4 \div 30$
MGH-FHBPTC, Boston, USA	230	159	6.6	0.9	$6 \div 15$
PSI, Villingen, Switzerland	250	75	1.5	1.8	$5 \div 20$
TRIUMF, Vancouver, Canada	500	74	1.3	1.9	≤ 15
ELTR - MC simulations	230	70	1.7	0.7	11*

* averaged dose rate from operational test measurements performed at ELTR with the Markus IC in a water phantom in the reference conditions, with the IC positioned in the middle of the SOBP of modulation width 16 mm and range of 32 mm, with the currently accepted scattering system described in **Section 3.2.5**. [Courtesy of PTO]

dose rate value is comparable with other facilities given in **Table 3.9**, enabling to limit the irradiation time to 90 s (for delivery of 15 $GyRBE$ at ELTR).

3.4.4. Scattering system in terms of beam misalignment

Despite the advantage in absorbed dose or field flatness, the double scattering method is also considered as more sensitive to the stability of beam alignment [Paganetti, 2011]. During the AIC-cyclotron operation, a stable, symmetrical beam alignment was difficult to maintain during the entire therapy day and frequent QA checks were performed before each treatment to avoid the risk of beam inclination.

In order to verify the selected scattering set-ups $1-3$ in terms of the sensitivity to the beam misalignment, in the FLUKA code feasible hypothetical beam distortions were introduced to the source definition:

- shift in beam position of 0.5 mm or 1.0 mm in X direction (beam parallel to the original beam axis) - $\Delta x = +0.5\ mm, +1.0\ mm$;
- spot size change of $\pm 10\%$ ($\sigma^{MC}_{mean} \pm 10\%$).

The simulated entrance lateral dose profiles are shown in **Figures 3.13-3.14** and **Tables 3.10-3.11** compare considered lateral beam parameters (P_{mean}, L_{95}, F_{90}, D_{BP}) with constraints given in **Table 3.1**. For depth-dose profiles, the difference in extracted beam parameters (R_{90}, DFO_{90-10}, $FWHM_{BP}$, $max/plateau$ ratio) was negligible, as considered beam modifications had no significant impact on the energy distribution.

The applied shift in beam position did not affect lateral penumbrae P_{mean} for both single and double scattering set-ups $(1-3)$ for both considered beam collimator sizes. Relative dose difference of D_{BP} did not exceed 0.3% for both beam collimator sizes. Lateral field width $L_{95}(\varnothing 35\ mm) < 30.0\ mm$ was observed for single scattering set-ups 1 and 2; while $L_{95}(\varnothing 25\ mm) \geq 19.0\ mm$ was fulfilled in all set-ups. Lateral field flatness F_{90} did not exceeded the 5% constraint for 35 mm beam collimator,

Table 3.10. Beam parameters of three selected scattering set-ups. Set-up 1 - S1 60 μm *Ta*; set-up 2 - S1 25 μm *Ta* foil with S2 60 μm *Ta* foil; set-up 3 - 1 mm PMMA ring with $r_{S2} = 6$ mm *Ta* disk of $d_{S2} = 80$ μm after introduction of the source shift of $\Delta x = 0.5$ mm or 1.0 mm for $\varnothing 35$ mm and $\varnothing 25$ mm beam collimator.

	set-up	**collimation**	P_{mean} $[mm]$	$F_{90\%}$ [%]	L_{95} $[mm]$	$D_{BP}(1\ nA)$ $[Gy]$
$\Delta x = 0.5$ mm	1	$\varnothing 35$ mm	2.0 ± 0.01	4.2 ± 0.4	28.1 ± 0.1	0.64 ± 0.07
	2		2.0 ± 0.1	3.8 ± 0.4	30.2 ± 0.1	0.63 ± 0.07
	3		1.4 ± 0.1	3.8 ± 0.3	32.6 ± 0.1	0.81 ± 0.07
	1	$\varnothing 25$ mm	1.2 ± 0.1	5.0 ± 0.4	19.3 ± 0.1	0.64 ± 0.06
	2		1.3 ± 0.1	5.8 ± 0.4	19.0 ± 0.1	0.63 ± 0.08
	3		1.1 ± 0.1	5.0 ± 0.3	21.7 ± 0.1	0.81 ± 0.05
$\Delta x = 1.0$ mm	1	$\varnothing 35$ mm	1.7 ± 0.1	3.9 ± 0.4	29.7 ± 0.1	0.64 ± 0.06
	2		2.0 ± 0.1	3.7 ± 0.4	30.0 ± 0.1	0.63 ± 0.07
	3		1.6 ± 0.1	5.7 ± 0.4	30.1 ± 0.1	0.81 ± 0.07
	1	$\varnothing 25$ mm	1.2 ± 0.1	5.8 ± 0.4	19.8 ± 0.1	0.64 ± 0.05
	2		1.3 ± 0.1	5.7 ± 0.4	18.9 ± 0.1	0.63 ± 0.06
	3		1.2 ± 0.1	6.9 ± 0.4	23.4 ± 0.1	0.81 ± 0.05

Table 3.11. Beam parameters of three selected scattering set-ups: set-up 1 - S1 60 μm *Ta*; set-up 2 - S1 25 μm *Ta* foil with S2 60 μm *Ta* foil; set-up 3 - 1 mm PMMA ring with $r_{S2} = 6$ mm *Ta* disk of $d_{S2} = 80$ μm after change in the beam spot size of $\sigma \pm 10\%$ for $\varnothing 35$ mm and $\varnothing 25$ mm beam collimator.

	set-up	**collimation**	P_{mean} $[mm]$	$F_{90\%}$ [%]	L_{95} $[mm]$	$D_{BP}(1\ nA)$ $[Gy]$
$\sigma^{MC}_{mean} - 10\%$	1	$\varnothing 35$ mm	1.8 ± 0.1	3.4 ± 0.4	27.6 ± 0.1	0.64 ± 0.07
	2		2.1 ± 0.1	3.8 ± 0.4	30.2 ± 0.1	0.63 ± 0.06
	3		1.2 ± 0.1	2.9 ± 0.4	32.9 ± 0.1	0.80 ± 0.04
	1	$\varnothing 25$ mm	1.1 ± 0.1	5.1 ± 0.4	18.9 ± 0.1	0.64 ± 0.07
	2		1.3 ± 0.1	5.5 ± 0.4	18.5 ± 0.1	0.63 ± 0.08
	3		1.0 ± 0.1	4.0 ± 0.4	23.1 ± 0.1	0.80 ± 0.06
$\sigma^{MC}_{mean} + 10\%$	1	$\varnothing 35$ mm	2.0 ± 0.1	3.9 ± 0.4	29.4 ± 0.1	0.64 ± 0.08
	2		2.1 ± 0.1	3.4 ± 0.4	30.5 ± 0.1	0.63 ± 0.06
	3		1.2 ± 0.1	3.1 ± 0.4	32.6 ± 0.1	0.82 ± 0.07
	1	$\varnothing 25$ mm	1.1 ± 0.1	5.1 ± 0.4	20.1 ± 0.1	0.64 ± 0.05
	2		1.3 ± 0.1	5.2 ± 0.4	19.4 ± 0.1	0.63 ± 0.06
	3		1.1 ± 0.1	4.0 ± 0.3	22.0 ± 0.1	0.82 ± 0.06

however, for 25 mm beam collimator system it was above 4.3% for all three set-ups within the uncertainty level.

Likewise, changes in spot size also did not affect P_{mean} values, for both single and double scattering set-ups for both considered beam collimators. Relative dose difference of D_{BP} did not exceed 1.0% for both beam collimator sizes. $L_{95}(\varnothing 35\ mm) < 30.0\ mm$ was observed only for a single scattering set-up 1 with S1 scatterer; for $\varnothing 25\ mm$ beam collimator only set-up 2 did not fulfil the criteria of $L_{95}(\varnothing 25\ mm) \geq 19.0\ mm$. Requirement for $F_{90}(\varnothing 35\ mm) < 5.0\%$ parameter was met for all three set-ups, whereas for the $\varnothing 25\ mm$ beam collimator only scattering set-up 3 was characterised by F_{90} below 4.3% value.

In summary, the comparison to the basic values given in **Table 3.7** has shown persistence of the lateral penumbrae and maximum dose at BP depth for shifting the beam position or changing the spot size.
Beam source shift resulted in both lateral field width L_{95} contraction and field flatness F_{90} raise, exceeding the constraint values from **Table 3.1**. Single scattering set-ups were more sensitive to the beam source shift, with L_{95} maximum relative difference of 7.3% for set-up 2 ($\varnothing 35\ mm$, $\Delta x = +0.5\ mm$) and F_{90} maximum relative difference of 17.8% for set-up 2 ($\varnothing 25\ mm$, $\Delta x = +1.0\ mm$). For the double scattering set-up 3, beam source shift was observed in field flatness change, with maximum relative difference of 82.3% ($\varnothing 35\ mm$, $\Delta x = +1.0\ mm$). However, for set-up 3 lateral field width stayed within the constraints.
Changes in spot size did not affect the double scattering set-up 3 within the constraints values. For single scattering set-ups, the spot size change influenced lateral field width with the maximum relative difference of 9.1% ($\varnothing 35\ mm$, $\sigma = -10\%$) and the F_{90} maximum relative difference of 11.2% ($\varnothing 25\ mm$, $\sigma = -10\%$).

Field flatness F_{90} was the parameter most prone to beam distortions, even though its large uncertainties and 1D profile investigation hinders analysis. It was especially expressed for the double scattering set-up (3) because the beam did not hit centrally the high-Z disc of S2, a problem known and requiring additional beam position monitoring feedback [Takada, 1994]. A proposed solution is to enlarge the distance between S1 and S2 which lowers the set-up sensitivity to the beam distortions [Takada, 1994], however it was impossible in the case of ELTR geometry due to limited space on the optical bench. Summing up, lateral field width L_{95} and field flatness F_{90} are parameters sensitive to the beam distortions. Beam source shift or spot size change should be monitored to exclude the beam misalignment scenario. Beam source shift of $\Delta x \geq 0.5\ mm$ or spot size change $\sigma \geq \pm 10\%$ showed to be sufficient for the emergency beam stop within the considered scattering set-ups $1 - 3$.

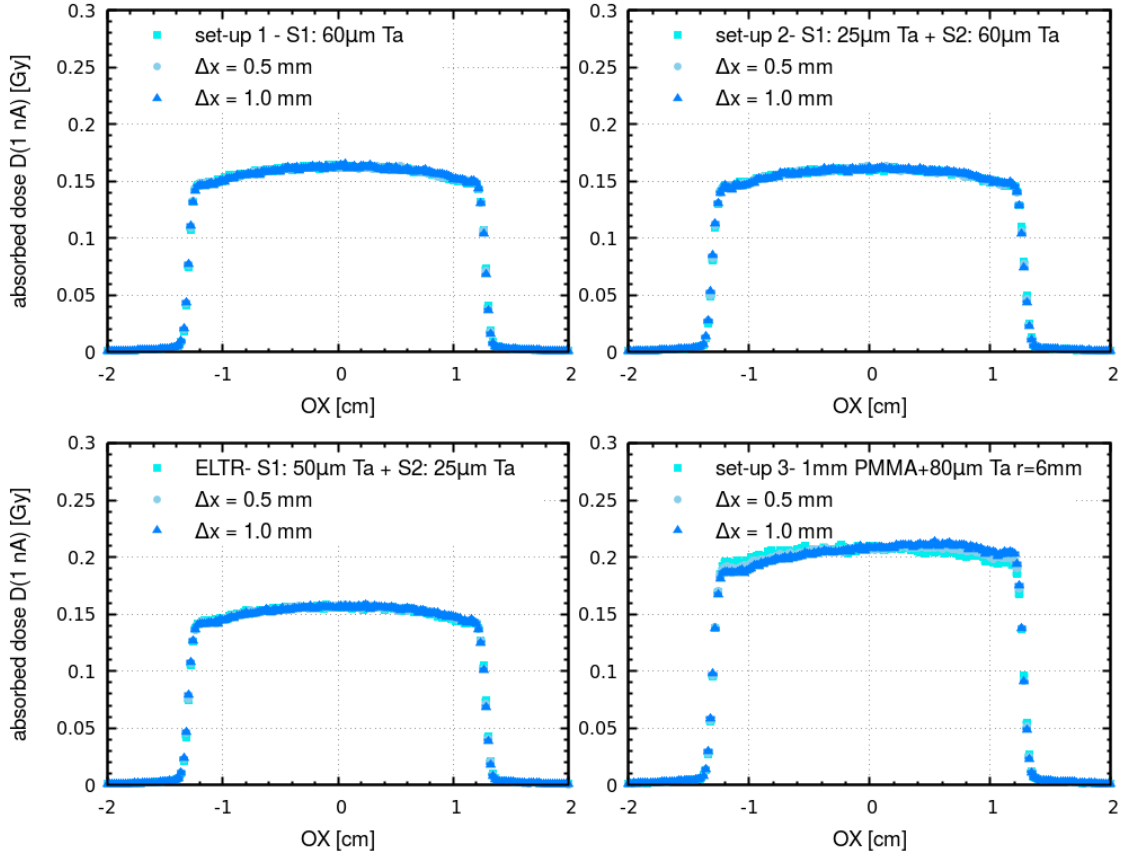

Figure 3.13. Entrance lateral dose profiles calculated for 1 nA beam current after implementing beam source deviation of $\Delta x = 0.5$ or 1.0 mm for the selected scattering set-ups: set-up 1 - S1 60 μm Ta (top left); set-up 2 - S1 25 μm Ta foil with S2 60 μm Ta foil (top right); set-up 3 - 1 mm PMMA ring with $r_{S2} = 6$ mm Ta disk of $d_{S2} = 80$ μm (bottom right). In bottom left panel, current ELTR geometry (S1 50 μm Ta + S2 25 μm Ta) was also calculated in the FLUKA code. beam collimator is $\varnothing 25$ mm.

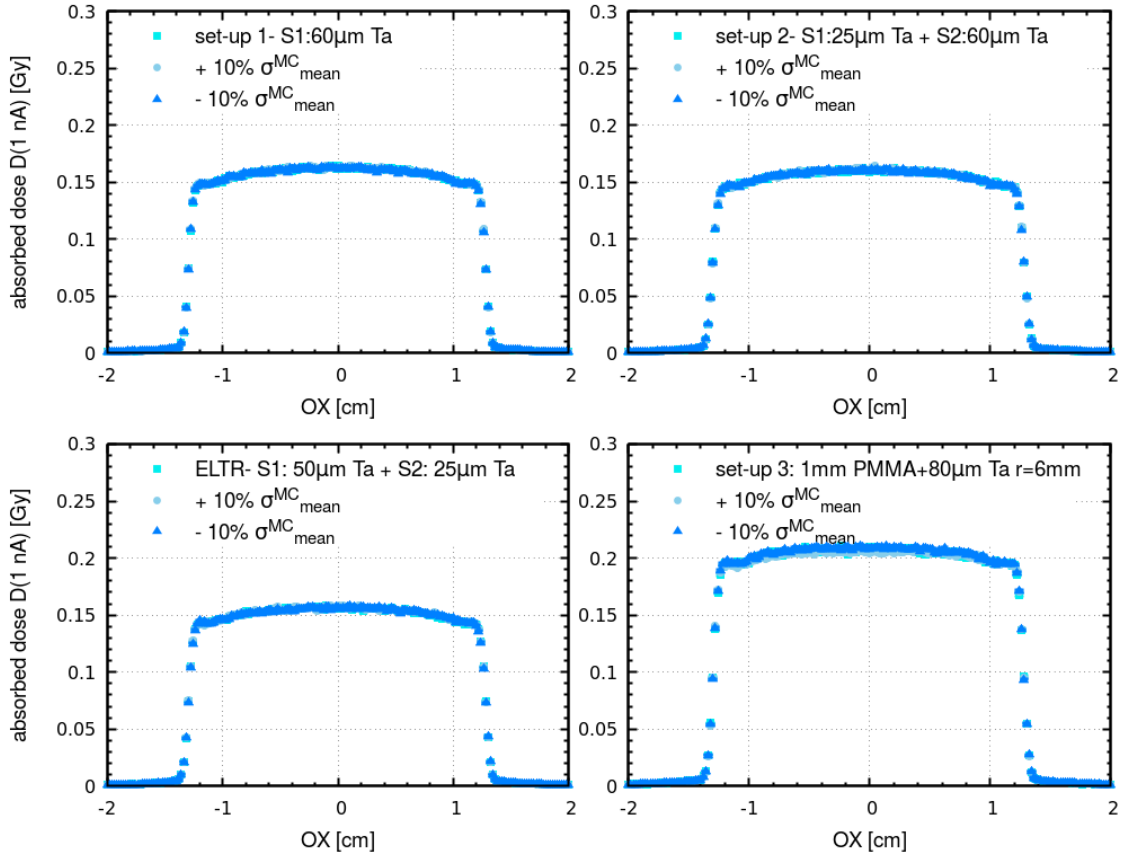

Figure 3.14. Entrance lateral dose profiles calculated for 1 nA beam current after implementing beam spot size deviation of $\sigma^{MC}_{mean} \pm 10\%$ for the most favourable scattering solutions: for the selected scattering set-ups: set-up 1 - S1 60 μm Ta (top left); set-up 2 - S1 25 μm Ta foil with S2 60 μm Ta foil (top right); set-up 3 - 1 mm PMMA ring with $r_{S2} = 6$ mm Ta disk of $d_{S2} = 80$ μm (bottom right). In bottom left panel, current ELTR geometry (S1 50 μm Ta + S2 25 μm Ta) was also calculated in the FLUKA code. beam collimator is $\varnothing 25$ mm.

3.5. Conclusions

For high-energy cyclotron-based facilities, one of the most demanding issues is the maximisation of dose rate while preserving the required beam characteristics. The main purpose of MC simulations presented in this chapter was to study various scattering set-up geometries developed for ELTR of CCB at IFJ PAN.

The analysis of the scattering system for the ELTR was based on the beam model built in the FLUKA particle transport code. Corresponding beam energy, momentum spread, spot size and beam angular distributions were established, creating MC beam model of pristine ELTR beam. This MC beam model was positively verified with measurements performed with Bragg Peak Chamber in *BluePhantom*^{2}, a CCD-based *ProBImS* system and with the Markus ionisation chamber. The beam parameters stayed in agreement of ± 0.1 mm with experimental values, except beam size σ_y of 1 mm difference (181.5 cm from the IGE).

The symmetrised MC beam model of the ELTR was next verified against current ELTR measurement data showing differences of $0.1 \div 1.1$ mm for R_{90}, DFO_{90-10}, $FWHM_{BP}$, P_{mean}, L_{95}. For $max/plateau$ ratio the difference was within 0.2. Field flatness F_{90} difference was 2%. The symmetrised MC beam model was accepted for analysis of the ELTR scattering system. The FLUKA input file containing the symmetrised MC beam model of the ELTR beam was given in **Appendix A**.

With the symmetrised MC beam model 87 scattering set-ups were studied, divided in three groups: S1 - single *Ta* foil, S1+S2- two *Ta* foils positioned 30 cm from each other and dual ring method as *Ta* disk surrounded by PMMA ring forming only S2 scatterer. For each set-up 1D lateral and depth-dose profiles were calculated, corresponding to measurements performed with a rectifier diode in the X-scanner or with the Markus IC in the 3D-scanner. From the extracted profiles, mean penumbrae P_{mean}, lateral field flatness F_{90} and lateral field width L_{95} were evaluated, together with absorbed dose at the BP depth D_{BP} (recalculated for 1 nA beam current $D_{BP}(1\ nA)$), to select most favourable scattering solution. Reducing the optimisation to four beam parameters was found sufficient in the scattering system analysis. The lateral field flatness F_{90} was suggested to be an auxiliary factor due to its sensitivity to dose fluctuations coming from the parameter definition (**Chapter 1.3.2**). The best set-ups $1-3$ were presented in **Table 3.7** and **Figures 3.11**. These were: set-up 1 - S1 60 μm *Ta* foil; set-up 2 - S1 25 μm *Ta* foil with S2 60 μm *Ta* foil; set-up 3 - 1 mm PMMA ring with $r_{S2} = 6$ mm *Ta* disk of $d_{S2} = 80$ μm. For all three solutions, the beam parameter constraints (**Table 3.1**) were fulfilled. The calculated relative difference of maximum dose D_{BP}, when compared to the reference value for the current ELTR scattering set-up, was 6%, 4% and 33% for set-up 1, 2 and 3, respectively.

It was demonstrated that the technique of single scattering was less efficient in terms of beam utilisation as most of the beam is cut out to provide demanded dose uniformity. Double scattering systems give a higher dose at the BP depth, simultaneously having sharper beam penumbrae, comparable lateral field flatness and similar or better lateral field width. However, double scattering systems require very stable beam delivery. With variation of beam position, the double scattering system appeared less stable because the beam was partly passig through the central disk. Therefore, the present scattering set-up of ELTR at CCB IFJ PAN is equipped with a single

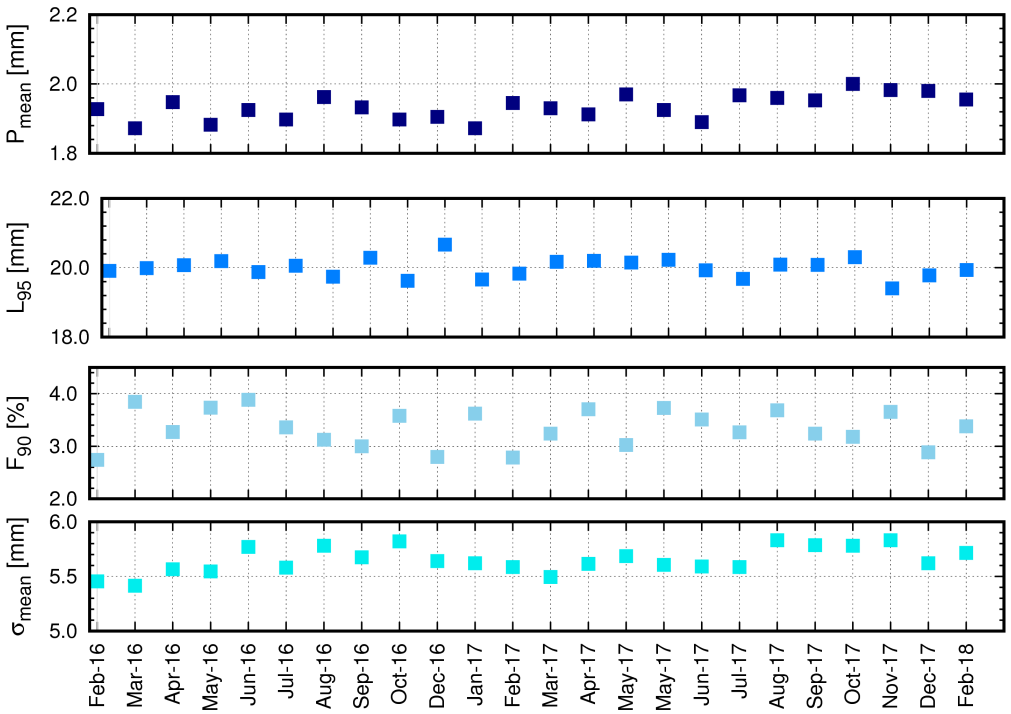

Figure 3.15. Mean values of lateral field flatness F_{90}, lateral field width L_{95} and mean penumbrae P_{mean} measured at the ELTR between *Feb.* 2016 and *Feb. 2018* for $\varnothing 25$ mm beam collimator (top three). Bottom panel shows mean beam size (σ_{mean}) measured by the BPM positioned at the IGE. Uncertainty level of ± 0.1 mm was not marked to retain plot readability. [Courtesy of PTO]

scattering system. **Figure 3.15** shows the measured beam parameters of the ELTR from *Feb.* 2016, since eye cancer patients have been treated at the ELTR in CCB IFJ PAN, assessed till *Feb.* 2018. The average from X and Y profiles result in the following beam parameters: mean lateral penumbrae $P_{mean} = 1.9 \pm 0.1$ mm, mean lateral field width $L_{95} = 20.0 \pm 0.3$ mm, mean field flatness $F_{90} = 3.3 \pm 0.4\%$ and mean spot size $\sigma_{mean} = 5.6 \pm 0.1$.

Chapter 4

Modelling an active scanned proton pencil beam in the CCB gantry room

4.1. Introduction

After widespread use of passively scattered beams in treatment modalities, the advanced technique of Pencil Beam Scanning (PBS) was introduced for protons in PSI (Villingen, Switzerland) [Lomax et al., 2004] and at the GSI (Darmstadt, Germany) with carbon-ions [Amaldi and Kraft, 2005]. At present, treatment units with Pencil Beam Scanning are becoming a new standard in proton facilities world-wide [www.ptcog.ch]. This advanced technology enables higher efficiency in dose planning and delivery, homogeneous target dose coverage with significant decrease in dose delivered to shallower healthy tissues preceding the target region competing with passively scattered proton beams or photon radiotherapy techniques for image-guided and adaptive radiotherapy (*e.g.* [Schippers and Lomax, 2011] [Kooy et al., 2010] [Lomax et al., 1999]). When compared to the scattering system delivery, PBS is found easier and safer in terms of the dose delivery while no beam perturbations such as proton interactions with the materials of the delivery systems have to be accounted for [Clasie et al., 2012]. Concomitantly, dosimetry of single pencil-beams is not covered currently by used codes of practice in reference dosimetry such as TRS-398 protocol [TRS-398, 2001].

Therefore, each proton facility develops own strategy of the facility commissioning – a process in which treatment delivery system is characterised to provide accurate and secure treatments. The commissioning of the facility combines a variety of functional tests of the system, documentation of the verified and accepted technical procedures, work instructions, forms, etc., and extensive verification of the dose calculation algorithms against the measured dose [TRS-430, 2004]. The dosimetric verification encompasses the commissioning of the local treatment planning system (TPS) requiring

not only vendor- but even site-specific dosimetry data which characterises a particular proton beam. With some additional information on the vendor-specific characteristics of the beam delivery (*e.g.* such as the distance between scanning magnets and the isocentre or distance between the main beam monitor and the isocentre), the TPS forms a dedicated beam model applied for dose calculations in all treatment plans. The required input data differs depending on a given TPS, however general data may be distinguished as (*e.g.* [Grevillot et al., 2011] [Pedroni et al., 2005] [Gillin et al., 2010]):

- set of lateral beam shape, preferably in several distances from the isocentre (for the measurements along the beam axis),
- set of the depth-dose profiles for the therapeutic energy range,
- calibration of the beam monitor (in Monitor Units (MU)) in reference to absolute dose (in Gy).

Lateral beam shape is typically registered with CCD-based scintillating screens (such as Lynx PT detector, IBA Dosimetry, Schwarzenbruck, Germany), with film dosimetry (such as Gafchromic EBT Film, International Specialty Products, Wayne, NJ or Kodak XV films, Eastman Kodak, Rochester, NY) and with ionisation chambers (such as pin point type 31014, PTW, Freiburg, Germany) [Anand et al., 2012] [Pedroni et al., 2005] [Grevillot et al., 2011] [Gillin et al., 2010].

For lateral measurements of the single pencil-beam, the detection area is large enough to cover whole lateral fluence or dose distribution of the spot (*e.g.* at CCB for 70 MeV beam size $\sigma = 6.5\ mm$ at the isocentre). The equipment limitations appear for depth-dose profiles performed regularly with dedicated Bragg Peak Chamber (BPC, TW34070 PTW, Freiburg, Germany). The size of the chamber ($r = 4.08\ cm$) is too small to account for the entire pencil-beam as observed first by [Pedroni et al., 2005]. So-called *core* of a single proton pencil beam broadens with depth due to the multiple Coulomb scattering (MCS) and primary protons are slowed down by multiple collisions with atomic electrons [Gottschalk et al., 2015]. Additionally, the core is surrounded by a low dose component, the effect termed as the *beam halo* [Pedroni et al., 2005] or low-dose envelope [Sawakuchi et al., 2010b]. It comes from the secondary particles (mainly secondary protons) as products of the elastic interactions on hydrogen, and from elastic, inelastic and non-elastic interactions with oxygen in water [Gottschalk et al., 2015].

Figure 4.1 shows depth-dose distribution (DDD) of a single 180 MeV proton pencil-beam in water, simulated in the FLUKA code. The beam parameters of the GTR3 room of the CCB were applied in this simulation. To illustrate the dose not accounted for due to the detector size limitations, a diameter $\varnothing 8.16\ cm$ of the BPC is marked. Skipping the contribution of nuclear interactions may result in dose underestimation during the treatment planning process up to $8-10\%$ depending on the target volume and number of pencil-beams [Pedroni et al., 2005] [Sawakuchi et al., 2010a]. Thus providing reliable Integral Depth Dose (IDD, also noted as Planar Integral Spot Doses - PISD [Anand et al., 2012]) to the TPS becomes essential for correct dose calculation.

Several approaches have been developed to correct for the limited dimensions of the IC: the analytical model development based on experimentally acquired data [Pedroni et al., 2005] [Gottschalk et al., 2015] [Anand et al., 2012], calculation of the correction

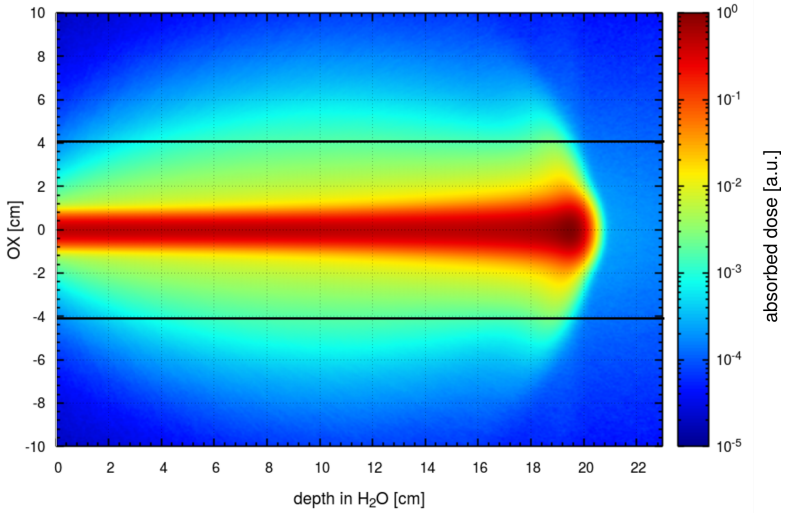

Figure 4.1. Depth-dose distribution of 180 MeV proton beam impinging a water phantom with absorbed dose normalised to the maximum value. Black lines indicate the size of the Bragg Peak Chamber (PTW) of radius $r = 4.08$ cm routinely used for depth-dose distribution assessment.

factors for the IC-measured Bragg peaks [Clasie et al., 2012] or analytical modification of the IDD distributions [Zhang et al., 2011]. The complementary method was the usage of Monte Carlo simulations.

MC methods are found useful in the characterisation of a large number of therapeutic beam energies required for the TPS, reducing measurement burden (*e.g.* [Anand et al., 2012] [Gillin et al., 2010]). Moreover, MC calculation provides controlled level of precision when difficulty in dosimetry of narrow pencil-beams appears [Anand et al., 2012]. Heretofore reported MC codes employed in the PBS commissioning of proton facilities were MCNP(X) [Sawakuchi et al., 2010a] [Ardenfors et al., 2017] or Geant4/GATE [Clasie et al., 2012] [Grevillot et al., 2011]. Recently FLUKA code joined MC PBS modelling [Fiorini et al., 2018].

This chapter presents the development of the Monte Carlo-based beam model for commissioning of the Eclipse ver. 13.6 Treatment Planning System (TPS) at the CCB facility. First, a MC beam model was developed based on beam depth-dose and phase space measurements. Next, dose correction factors were calculated for IDD $r = 20$ cm simulation. The impact of the calculated IDD corrections was estimated in the TPS and the corrected MC-based beam model was accepted for routine patient treatment planning at the CCB facility. Some simplifications applied for MC gantry beam model assessment, *e.g.* skipped nozzle modelling, simplified source definition, single Gaussian spot shape or beam divergence, are considered in the discussion.

4.2. Materials and Methods

Figure 4.2 illustrates the measurements of the GTR beam performed during the commissioning (left), together with corresponding simulation geometry in the FLUKA code (right). In the middle of **Figure 4.2**, extracted data with evaluated beam parameters are outlined.

4.2.1. Dosimetry of Pencil Scanning Beam at the GTR

Depth-Dose Distribution

For the measurements of the depth-dose distribution (DDD) the *Blue Phantom*^{2} (IBA Dosimetry) was positioned at the technical table in the gantry room (GTR3). The measurement details are given in **Chapter 2.1.4**. A parallel-plate ionisation chamber (IC) called the Bragg Peak Chamber TW34070 (PTW) of radius $r = 4.08\ cm$ was mounted inside the phantom to be moved along the beam axis. The beam impinged on the water tank from the top (*i.e.* at the gantry angle $\phi_G = 0°$), omitting irradiation through the phantom walls. The isocentre was set at 2 cm below the water surface with 44.5 cm nozzle-to-water air gap. The IC was connected to a Common Control Unit (CCU) with integrated two-channel electrometer. The output of the beam monitors IC2 and IC3 was also connected to the CCU with an entrance beam signal for beam fluctuations correction (IC2 and IC3 are located in the nozzle). Collected charge was then calculated as relative dose in water, corrected to the entrance beam current fluctuations. The DDDs were then normalised to the maximum dose value at the BP depth, resulting in a set of Percentage Depth-Dose curves ($PDD^{BPC}(E)$). For DDDs normalised at 2 cm depth in water, they will be referenced as $IDD^{BPC}(E)$.

The $IDD^{BPC}(E)$ were acquired each 10 MeV for available therapeutic energy range ($70\ MeV \leq E \leq 220\ MeV$) and additionally for 225 MeV and 226.08 MeV. Depending on the BP region (plateau, BP, distal fall-off), measurements were performed every $0.2\ mm \div 3\ mm$ steps.

The same measurement method was redone in the second gantry room (GTR4). The detailed dosimetric procedure is described in the set of operational procedures of [CCB Quality Book, 2015]. Total experimental uncertainty for the DDD beam parameters assessment was estimated to 0.5 mm by [Mojżeszek, 2018],including chamber positioning precision, water vaporisation, precision of the $BluePhantom^2$ positioning and uncertainty of the BPC cover WET value. For the relative dose read-out, the assumed precision was $u(IDD^{BPC}(z) = 0.9\%$, given in [Mojżeszek, 2018]. The left side of **Figure 4.2 A** illustrates the DDDs measurements with BPC immersed in *Blue Phantom*^{2}.

Spot lateral dose profiles

For the measurements of the spot size in air as a function of the distance from the isocentre, the scintillation detector Lynx PT (IBA Dosimetry) was applied, according to the measurement method described in **Chapter 2.1.4**). The detector was placed on the treatment couch in such a way that the scintillator surface was positioned perpendicularly to the beam axis, at 5 locations: at the isocentre ($z = 0\ cm$) and at $\pm 10\ cm$,$\pm\ 20\ cm$ from the isocentre along the beam axis. Gantry angle was set

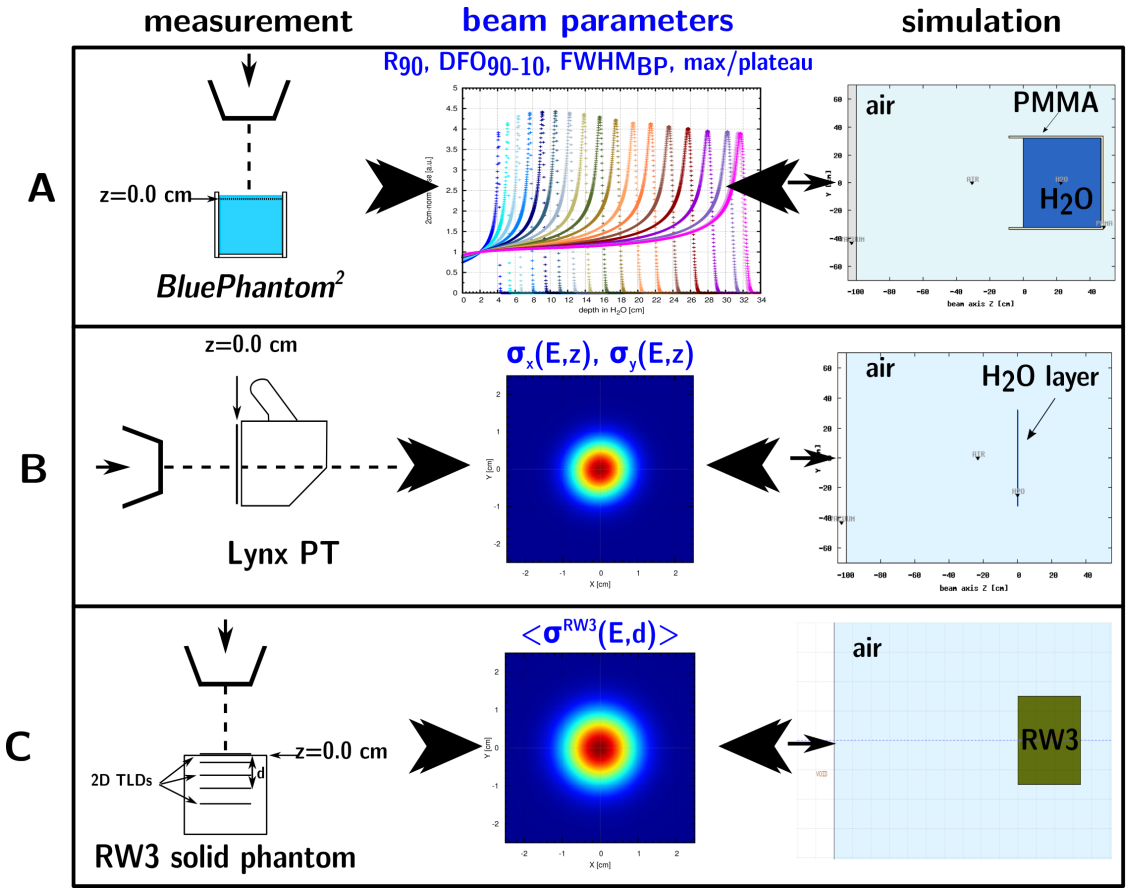

Figure 4.2. GTR measurement set-up (left), corresponding MC simulation geometry (right) and evaluated beam parameters for the MC beam model verification (middle). A: Beam range measurements in a water-filled *BluePhantom*^{2} with BPC, with 44.5 cm nozzle-water surface air gap, with isocenter $z = 0.0cm$ at 2 cm depth in water. Gantry angle was $\phi_G = 0°$. Simulation geometry with horizontal beam direction included water cube surrounded by PMMA walls of 1.5 cm thickness.
B: Spot size measurements in air with Lynx PT positioned at the isocentre $z = 0.0cm$ with gantry angle $\phi_G = 270°$. Simulation geometry included water layer in position defined at the isocenter, perpendicularly to the beam axis.
C: 2D TLD measurements of the spot size in RW3 solid phantom. Gantry angle was $\phi_G = 0°$ and upper surface of the solid phantom was positioned at the isocentre $z = 0.0$ cm. Foils were placed between adjacent RW3 plates. Simulation geometry included RW3 phantom of 30 $cm \times 30$ $cm \times 34$ cm (XYZ) with frontal surface positioned at the isocentre with horizontal beam axis.

to $\phi_G = 270°$ and no angle-spot shape dependency was checked during this measurements. Likewise for BPC measurements, spot images were captured for 18 available therapeutic ranges (each 10 MeV for 70 $MeV \div 220$ MeV, additionally for 225 MeV and 226.08 MeV), at each of the 5 positions from the isocentre.

Spot images $I^{Lynx}(x, y)$ were acquired by the Lynx PT with 0.5 mm resolution. According to **Equation 2.2**, the spot centre of mass $\overrightarrow{CM}$ was derived from 8 $cm \times 8$ cm region of interest and 1D lateral spot profiles X and Y were extracted (**Equation 2.3**). By fitting 1D Gaussian curve with **Equation 2.4**, separately for X and Y profile measured (m) spot sizes described by $\sigma_x^m(E, z)$ and $\sigma_y^m(E, z)$ were derived. Spot size measurements accuracy was assumed to 0.1 mm, following [Grevillot et al., 2011]. The left side of **Figure 4.2 B** illustrates spot size measurements with the Lynx PT.

4.2.2. Simulations of GTR pencil-beams

All radiation transport calculations were performed using the FLUKA transport code. Each input settings in FLUKA included HADROTHE(rapy) card option defining the physics of the particle transport, such as particle transport and energy cut-offs, type of followed particles etc., as described in detail in **Chapter 2.3.3**.

To compose a reliable MC beam model, the following simulations were performed:

- beam depth-dose distribution – to adjust the initial source energy and momentum spread (E^{MC}, $(dp/p)^{MC}$);
- spot size – to adjust initial source spatial distribution ($\sigma_x^{MC}(E)$, $\sigma_y^{MC}(E)$).

Simplified geometry of the gantry treatment rooms was modelled in FLUKA but the influence of walls, floor or ceiling was neglected in calculations. Two separate MC beam models were developed for GTR3 and GTR4, respectively.

The simulation geometry included: horizontal pencil-beam transported along the OZ axis, with source positioned in vacuum. The nozzle (treatment head) was not modelled in the simulations, mainly due to the limited access to the nozzle specification. Therefore, no beam monitor, entrance window nor the vicinity of the X-ray tube located in the nozzle were included in the simulations. Water Equivalent Thickness (WET) of the nozzle was replaced by an air-gap of 100.0 cm between the beam source position and point $z = 0.0$ cm, referred as isocentre in the experimental data. The right side of **Figure 4.2** illustrates the simulation geometry used for MC gantry beam model development and verification. For the calculation of the absorbed dose in water the mean excitation energy 75 eV was applied, recommended by [ICRU37, 1984], and discussed in **Chapter 2.3.4**.

Depth-dose distribution simulations

For the DDD simulations, a water phantom was implemented, with exterior dimensions: 67.5 $cm \times 64.7$ $cm \times 56.3$ cm. Default water material was used, with water density of 1 g/cm^3 assumed according to the FLUKA Material Database [Ferrari et al., 2011]. The PMMA walls of 1.5 cm were set from the FLUKA Material Database, as pre-defined "Plexiglas/Lucite/Perspex" of density $\rho = 1.19$ g/cm^3 according to ICRU recommendations and FLUKA manual [ICRU37, 1984] [Ferrari et al., 2011]. The entrance window was not implemented as the set-up was for gantry $\phi_G = 0°$ angle with the beam coming from the top and passing through the water solely. The dimensions of

the water phantom correspond to the $BluePhantom^2$ specification [Dosimetry, 2013]. While in the FLUKA code beam axis is horizontally defined, the whole phantom was rotated by 90° (as shown on the right side of **Figure 4.2 A**).

The scoring region was defined as a horizontal cylinder of 34 cm length, defined axially along the beam axis. Depth-dose curves were scored in slices 0.01 cm thick for energies 70 $MeV \leq E \leq 220$ MeV with 10 MeV step, additionally for 225 MeV and 226.08 MeV. In the first stage, the cylinder radius was equal to the radius of the BPC ($r = 4.08$ cm) to adjust the parameters of the beam model. The simulated number of protons was $6 \cdot 10^6$ run in 25 parallel runs to keep the statistical uncertainty of MC simulations below 1% of the determined dose.

Resulting $IDD_4^{MC}(E)$ curves were normalised at the Bragg peak maximum. Simulated (s) beam range $R_{90}^s(E)$ and distal fall-off $DFO_{80-20}^s(E)$ were determined with accuracy equal to the bin size of 0.1 mm. In the FLUKA code, beam energy E^{MC} was adjusted to reproduce the measured beam range ($R_{90}^m(E)$). The pencil beam momentum spread was assumed to have Gaussian distribution and $(dp/p)^{MC}$ parameter described by $FWHM$ was adapted to correspond the measured distal fall-off $DFO_{80-20}^m(E)$. Additionally, full-widths at half-maximum of the Bragg peak $FWHM_{BP}^s(E)$ and $max/plateau^s(E)$ ratios were calculated and compared with corresponding parameters from the BPC measurements. Uncertainty $u(FWHM_{BP}^s(E))$ was equal to the bin size of 0.1 mm. Uncertainty of the $max/plateau^s(E)$ ratios was calculated with the variance formula with $u(D_{max})$ and $u(D_{plateau})$ obtained from the simulation results.

Spot size simulations

A water layer of 30 $cm \times 30$ cm and 0.2 cm (XYZ) was defined at the isocentre, perpendicularly to the beam axis, 100 cm in air from the source position at $z = 0.0$ cm. Default water material was used, with water density of 1 g/cm^3 was assumed according to the FLUKA Material Database [Ferrari et al., 2011]. Though the spot size measured with the Lynx PT were acquired along the beam axis at $z = \pm 10.0$ cm and ± 20.0 cm from the isocentre, precision of the measurements was not satisfactory to determine the beam divergence, as discussed in **Subsection 4.4.3**. Thus, simulations were carried out only for the spot size at the isocentre ($z = 0.0$ cm). Only a divergent beam was assumed in the simulations, with zero angular spread of the pencil-beam, accounting solely for proton scatterings in air. The spatial beam distribution was assumed to follow Gaussian distribution and source parameters $\sigma_x^{MC}(E)$ and $\sigma_y^{MC}(E)$ were adjusted. The simulated number of protons was $5 \cdot 10^6$ run in 25 parallel runs to keep the statistical uncertainty of MC simulations below 1% of the determined dose.

From the simulated 2D absorbed dose distribution $I^{MC}(x, y)$, 1D X and Y profiles were extracted through the point $\vec{P}[0, 0]$ with voxel size of 0.2 $mm \times 0.2$ $mm \times 0.2$ mm. For each profile, a Gaussian curve was fitted, assuming $(0, 0)$ position of the centre of the peak:

$$f(x, E) = A_x \cdot exp\Big(\frac{-x^2}{2\sigma_x(E)^2}\Big),$$
$$f(y, E) = A_y \cdot exp\Big(\frac{-y^2}{2\sigma_y(E)^2}\Big) \tag{4.1}$$

with A_x, A_y normalised to the spot maximum value, and $\sigma_x^s(E)$, $\sigma_y^s(E)$ were simulated spot sizes to follow the spot sizes ($\sigma_x^m(E)$, $\sigma_y^m(E)$) obtained from the Lynx PT measurements. The right side in **Figure 4.2 B** illustrates geometry of the spot size simulations.

Integral depth-dose (IDD) distribution simulations

Empirical adjustment of the FLUKA source parameters (beam energy E^{MC}, beam momentum spread $(dp/p)^{MC}$, spot size $\sigma_x^{MC}(E)$, $\sigma_y^{MC}(E)$), enabled to develop MC-based gantry beam model. To derive the dose correction factor due to the improvement in DDD measurements with BPC, two additional integral depth-dose distributions were calculated, with radius $r = 10\ cm$ ($IDD_{10}^{MC}(E)$) and with $r = 20\ cm$ ($IDD_{20}^{MC}(E)$). The simulated number of protons was $6 \cdot 10^6$ run in 25 parallel runs to keep the statistical uncertainty of MC simulations below 1% of the determined dose.

The scoring was defined as a cylinder of 34 cm length with the slice thickness of 0.01 cm, scored for 18 gantry beam energies. The obtained results were normalised to $IDD_{20}^{MC}(E)$, IDD^{BPC}/IDD_{20}^{MC} ratio was calculated for BPC comparison. All IDD ratios depth-dose curves were normalised at 2 cm depth in water in order to minimise any perturbations connected to build-up effect and still at the plateau region of the DDD. This depth corresponds to the dose measurements performed for MUs calibration with Markus IC (PTW) as described in [Liszka et al., 2018].

4.2.3. Verification of the beam model

Pencil beam scattering in RW3 solid phantom

To verify the pencil-beam scattering in a medium other than air, spot sizes determined from the FLUKA MC simulations were compared with the spot sizes measured in the GTR3 at various depths of the RW3 solid phantom (PTW), described in **Chapter 2.1.4**. The measurements were performed with 2D TLD foils by Jan Gajewski, PhD, and a detailed description can be found in [Gajewski, 2016].

2D TLD foils type MCP were placed between RW3 phantom plates, while phantom upper surface was placed at the isocentre level with gantry angle $\phi_G = 0^\circ$ (*i.e.* irradiation from the top), as shown in **Figure 2.7**. The measurements were performed for single pencil-beams of the therapeutic energies: 80 MeV, 150 MeV, 170 MeV and 225 MeV. For each energy, spot size at the given depth in phantom was recalculated for corresponding water depth with $WET^{RW3} = 1.025 \pm 0.011$ and $WET^{TLD} = 1.64 \pm 0.05$ with given 1 SD [Gajewski, 2016]. The left side of **Figure 4.2 C** schematically illustrates the measurement set-up.

The resulting 2D lateral dose profiles were fitted with a 2D Gaussian distribution with rotation (R), according to **Equation 2.5**. The derived spot sizes σ_x^{m-R} and σ_y^{m-R} were used for comparison with the MC simulation results. While spot symmetry S^R, calculated as:

$$S^R = \frac{\sigma_x^R - \sigma_y^R}{\sigma_x^R + \sigma_y^R} \cdot 100\%, \tag{4.2}$$

was below 5%, the measured spot size was analysed as mean value of σ_x^{m-R} and σ_y^{m-R}, $\langle sigma_{RW3}^{m-R} \rangle$ [Gajewski, 2016].

The corresponding FLUKA calculations of the pencil proton beam impinging on the cuboid phantom of 30 $cm \times 30\ cm \times 34\ cm$ were performed for energies of 80 MeV, 150 MeV, 170 MeV and 225 MeV. The dedicated RW3 material with density of 1.045 g/cm^3 has been defined in the FLUKA code as polystyrene C_8H_8 containing 2% TiO_2 (*cf.* **Subsection 2.1.4**). 2D lateral profiles were extracted in 1 mm slices along the beam axis, each with 0.25 $mm \times 0.25\ mm$ pixel size. The same analysis method was applied: 2D Gaussian curve with rotation was fitted to the calculated images $I^{MC}(x, y)$ (**Equation 2.5**) resulting in the mean value of the spot size, $\langle \sigma^{s-R}_{RW3} \rangle$ from σ^{s-R}_x and σ^{s-R}_y. The fitting procedure was performed by Jan Gajewski. Water equivalent depth was calculated with $WET^{RW3} = 1.025\ cm \pm 0.011\ cm$ given by [Gajewski, 2016]. The simulated number of protons was $10 \cdot 10^6$ run in 30 parallel runs to keep the statistical uncertainty of MC simulations below 1% of the determined dose.

TPS beam model verification

To commission the Eclipse ver. 13.6 Treatment Planning System (Varian Medical Systems Inc., Palo Alto, CA, USA) the following data were required: in-air lateral beam profiles, calibration factors relating dose with MUs, CT calibration curves and the set of $IDD(E)$ curves [Systems, 2013]. Based on the above mentioned input data, TPS builds its own beam model separately for each treatment room.

The main goal of the MC simulations was to obtain a set of complete $IDD(E)$ curves as compared to those measured using BPC (denoted as $IDD^{BPC}(E)$). The MC-simulated normalised $IDD^{MC}_{20}(E)$ curves were multiplied by the calibration dose $D_{calib}(E)$ measured in 10 $cm \times 10\ cm$ field scanned spot-by-spot (2.5 mm spot spacing) with Markus ionisation chamber (PTW, Freiburg, Germany) immersed 2 cm below the water surface. The measurements geometry was described in [Liszka et al., 2018]. The procedure was repeated for 18 proton energies from 70 MeV to 226.08 MeV, in 10 MeV steps, with dedicated $D_{calib}(E)$ factor for each corresponding energy.

In the Eclipse TPS, two beam models were defined: $IDD^{BPC}(E)$-based from BPC measurements and $IDD^{MC}_{20}(E)$-based from Mc calculations. Both models have added dose correction depending on the range and modulation width, called DDNCF, described in **Section 4.4.4**. The comparison could not be performed for GTR3, and thus it was done for GTR4 beam data only. Several single field box-shaped treatment plans were prepared in Eclipse ver. 13.6 TPS, with various range (R), modulation width of the SOBP (M), and field size (F). **Table 4.1** compiles all considered treatment plans.

In the Eclipse ver.13.6 TPS a water phantom was defined as 30 $cm \times 30\ cm \times 30\ cm$ cuboid with voxel resolution of 1.17 mm and layer spacing of 1 mm. TPS calculation grid was set to 1.5 mm. Default spot spacing of 6.25 mm was applied, a value which is used in everyday treatment planning. Prescribed dose to the target region was set to 2 Gy. First, plan was calculated with $IDD^{MC}_{20}(E)$-based TPS beam model. Next, the TPS beam model was switched to the $IDD^{BPC}(E)$-based TPS beam model with unchanged settings of the spot positions and weights. Depth-dose profiles were extracted along the beam axis as the calculated dose from the axial line of voxels, each 1.17 $mm \times 1.00\ mm \times 1.17\ mm$. For two TPS beam models, $D^{BPC}_{TPS}(d)$ and $D^{MC}_{TPS}(d)$ point doses were extracted at depths: $d = 2\ cm$, in the middle of SOBP $d = R - M/2$ and at the distal end of the SOBP $d = R - 0.5\ cm$ (see **Figure 4.3**).

Table 4.1. List of treatment plans with various field size (F), modulation (M) and range (R) used for comparison of the BPC-based and MC-based TPS beam model.

Field size $F[cm \times \ cm]$	**Range** $R[cm]$	**Modulation** $M[cm]$	**Plan name**
3×3	10	5	R10M5F3
5×5	10	5	R10M5F5
10×10	10	5	R10M5F10
	15	5	R15M5F10
	20	5	R20M5F10
	25	5	R25M5F10
	25	10	R25M10F10
	25	15	R25M15F10
	25	20	R25M20F10

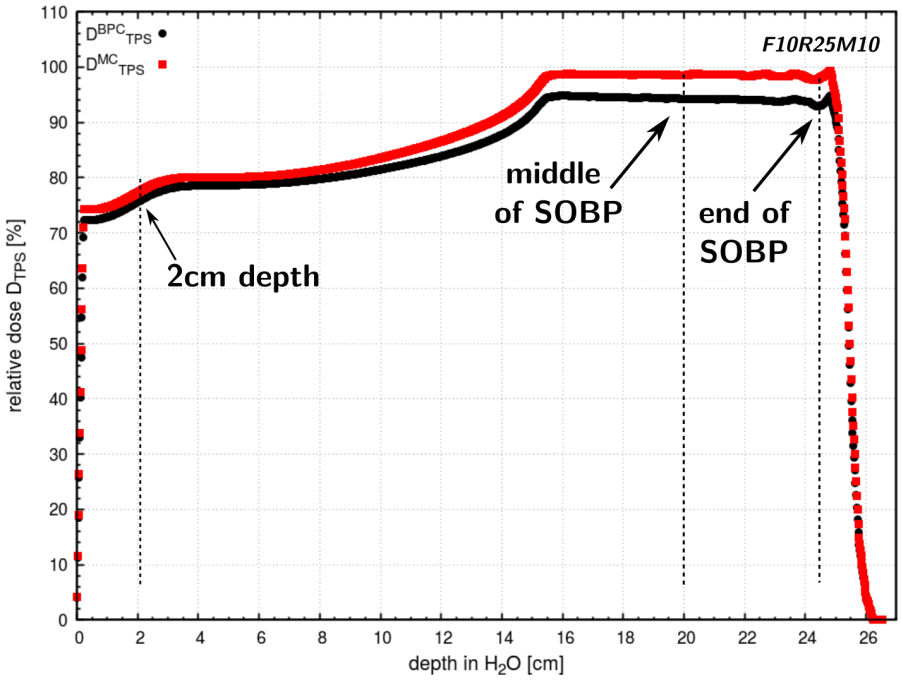

Figure 4.3. Relative depth-dose distributions calculated with the Eclipse TPS for two TPS beam models: $IDD^{BPC}(E)$-based (black circles) and $IDD^{MC}_{20}(E)$-based (red squares). Three analysed depths d of the calculated dose $D_{TPS}(d)$ are illustrated.

4.3. Results

Both treatment rooms, GTR3 and GTR4, are characterised by similar but not identical beam parameters. The so-called beam matching is planned at the CCB facility to allow for the performance of the same treatment plan in both treatment rooms. While the beam parameters are similar for both gantry rooms, in the following section only the results for the GTR3 treatment unit will be presented. The same was done for the GTR4.

4.3.1. Monte Carlo-based gantry beam model

The spot sizes calculated ($\sigma_x^s(E)$, $\sigma_y^s(E)$) and measured with the Lynx PT ($\sigma_x^m(E)$, $\sigma_y^m(E)$) are presented in **Figure 4.4**. For the whole range of analysed energies ($70 \div 226.08\ MeV$) maximum difference between measured and calculated σ_x ans σ_y was within $\pm 0.1\ mm$. While Gaussian spread was applied in the FLUKA code for the source spatial distribution, uncertainty of the fitted spot size $\sigma^s(E)$ was negligible (around $0.001\ mm$). Applied source spatial distribution parameters, σ_x^{MC} and σ_y^{MC} were therefore integrated for MC-based gantry beam model.

Beam energy and momentum spread were found by iterative method, resulting in E^{MC} and $(dp/p)^{MC}$ values for each nominal energy E. **Figure 4.5** presents $IDD_4^{MC}(E)$ curves normalised to the dose at 2 cm depth and compared to the measured IDD^{BPC} distributions. The maximum relative dose difference, calculated according to **Equation 2.7** with reference value $IDD^{BPC}(E, z)$ was 5.6% for 225 MeV.

For the verification of the MC-based beam model, range, distal fall-off, Bragg peak width and peak to entrance dose ratio are compared with the experimental data in **Figures 4.6-4.9**. Difference between measured and simulated range R_{90} did not exceed $0.12\ mm$. Results are shown in **Figure 4.6**. the calculated and measured distal fall-off DFO_{80-20} differ by not more than $0.2\ mm$, apart from 3 highest energies difference below $0.5\ mm$ (*cf.* **Figure 4.7**). Difference in Bragg peak width $FWHM_{BP}$ did not exceed $0.2\ mm$ (**Figure 4.8**). For $max/plateau$ ratio, differences were below 0.2 for 18 analysed energies. The calculated uncertainties $u(max/plateau)$ were below 0.001 for the MC simulations. Results are shown in **Figure 4.9**. It was demonstrated that the MC gantry beam model including E^{MC}, $(dp/p)^{MC}$, σ_x^{MC} and σ_y^{MC}, reproduced experimental beam parameters within $0.5\ mm$ (0.2 for $max/plateau$ ratio). This MC gantry beam model was used for all the further calculations. An exemplary FLUKA input file for IDD calculation was enclosed in **Appendix B**. The GTR3 beam model parameters are given in **Appendix C**.

4.3.2. Correction to the BPC measured curves from simulated IDD

Figure 4.10 presents $IDD^{MC}(E)$ for three detector sizes and two beam energies of $E = 70\ MeV$ and $E = 226.08\ MeV$. The effect of the detector radius increase is negligible for the lowest energy of $70\ MeV$, which is also visible in the plot of IDD/IDD_{20}^{MC}. For $70\ MeV$ proton beam energy fraction of long-distance nuclear interactions products is negligible and results in insignificant dose differences (IDD^{BPC}/IDD_{20}^{MC} below 2% of relative dose difference). On the contrary, for the highest energy of $226.08\ MeV$, as presented in bottom panel of **Figure 4.10**, the dose difference reaches 8.8% in the

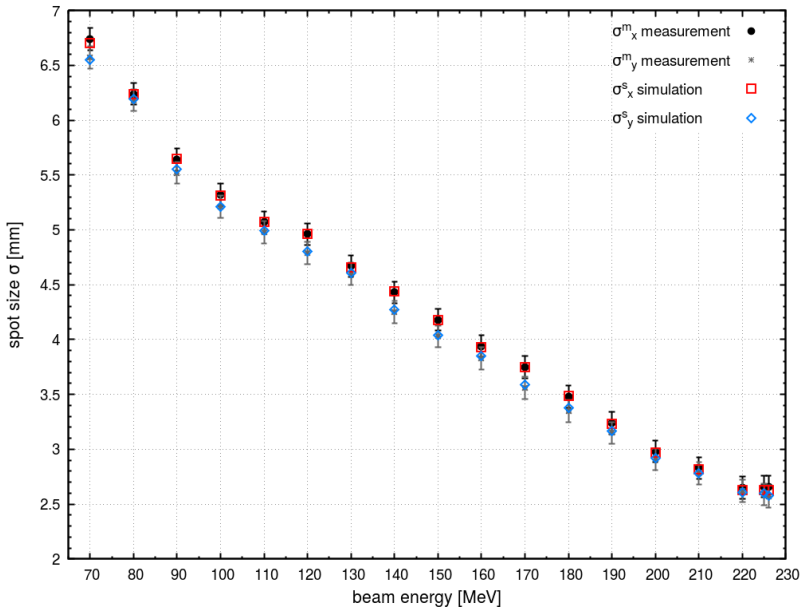

Figure 4.4. GTR3 spot sizes measured with Lynx PT (black circles and grey stars, for σ_x^m and σ_y^m, respectively) and simulated with MC gantry beam model (red hollow squares and blue hollow diamonds, for σ_x^s and σ_y^s respectively), as a function of 18 analysed nominal beam energies with uncertainties. [Measurement data from PDKJ]

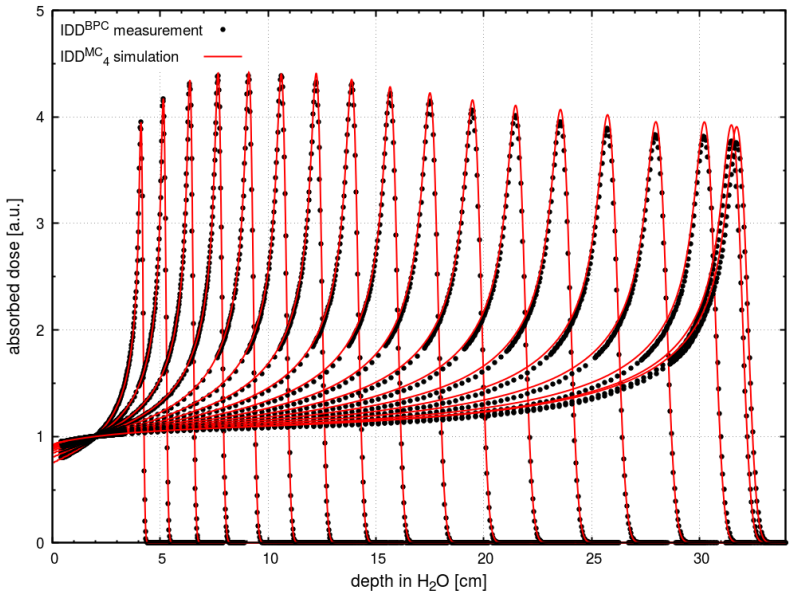

Figure 4.5. GTR3 $IDD^{BPC}(E)$ distributions acquired with BPC (black circles) and IDD_4^{MC} simulated curves with MC gantry beam model (red lines) for 18 analysed nominal beam energies, normalised at 2 cm depth. [Measurement data from PDKJ]

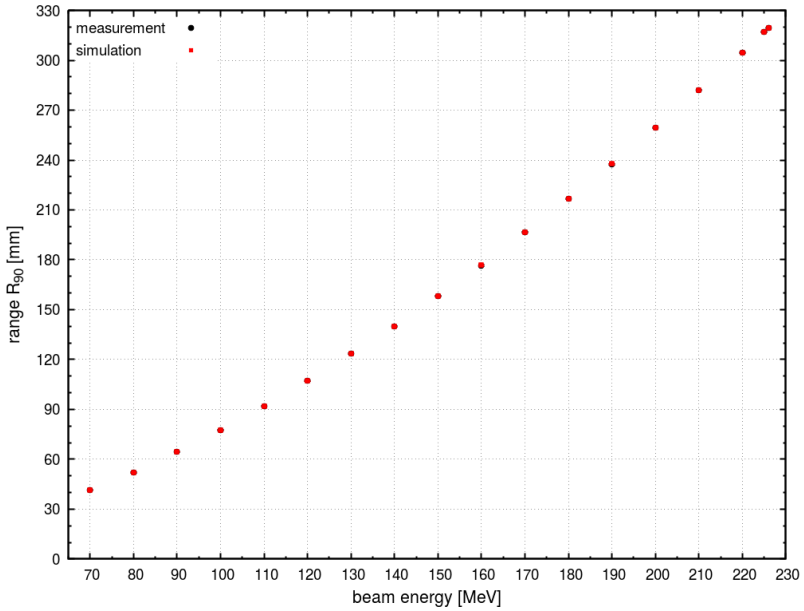

Figure 4.6. Proton beam range simulated (R^s_{90} - red squares) and measured with BPC (R^m_{90} - black circles). Uncertainties were 0.1 mm for MC simulation and 0.5 mm for BPC measurements, covered by data points. [Measurement data from PDKJ]

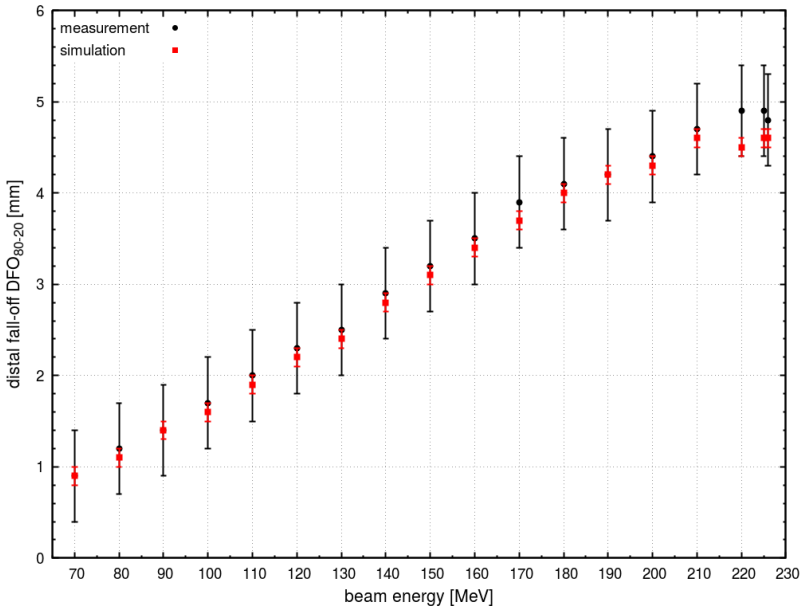

Figure 4.7. Distal dose fall-off $80\% - 20\%$ for both simulated (DFO^s_{80-20} -red squares) and measured with BPC (DFO^m_{80-20} - black circles) as a function of 18 analysed nominal proton beam energies. Uncertainties were 0.1 mm for MC simulation and 0.5 mm for BPC measurements. [Measurement data from PDKJ]

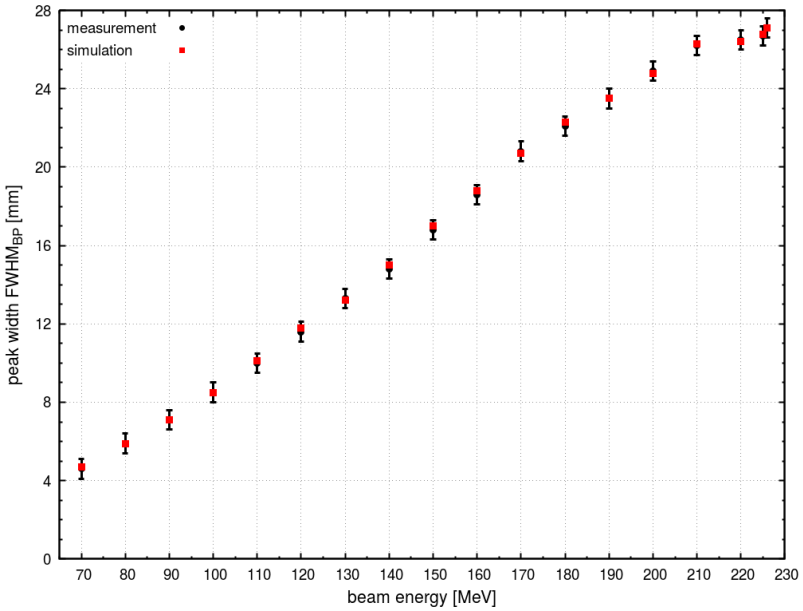

Figure 4.8. Bragg peak width at the level of 50% for both simulated ($FWHM^s_{BP}$ - red squares) and measured with BPC ($FWHM^m_{BP}$ - black circles) as a function of 18 analysed nominal beam energies. Uncertainties were 0.1 mm for MC simulation and 0.5 mm for BPC measurements. [Measurement data from PDKJ]

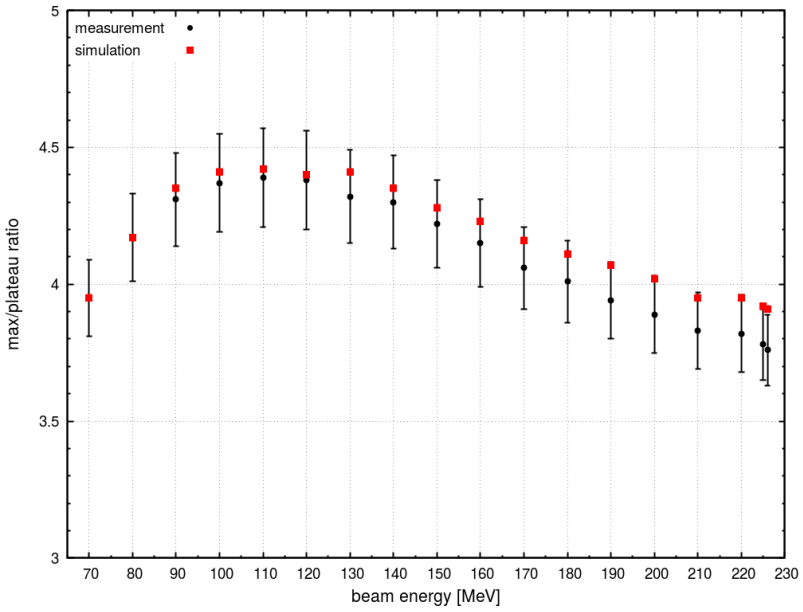

Figure 4.9. *Max/plateau* ratio for both simulated (red squares) and experimental (black circles) values, measured with BPC as a function of 18 analysed nominal beam energies with calculated uncertainties. [Measurement data from PDKJ]

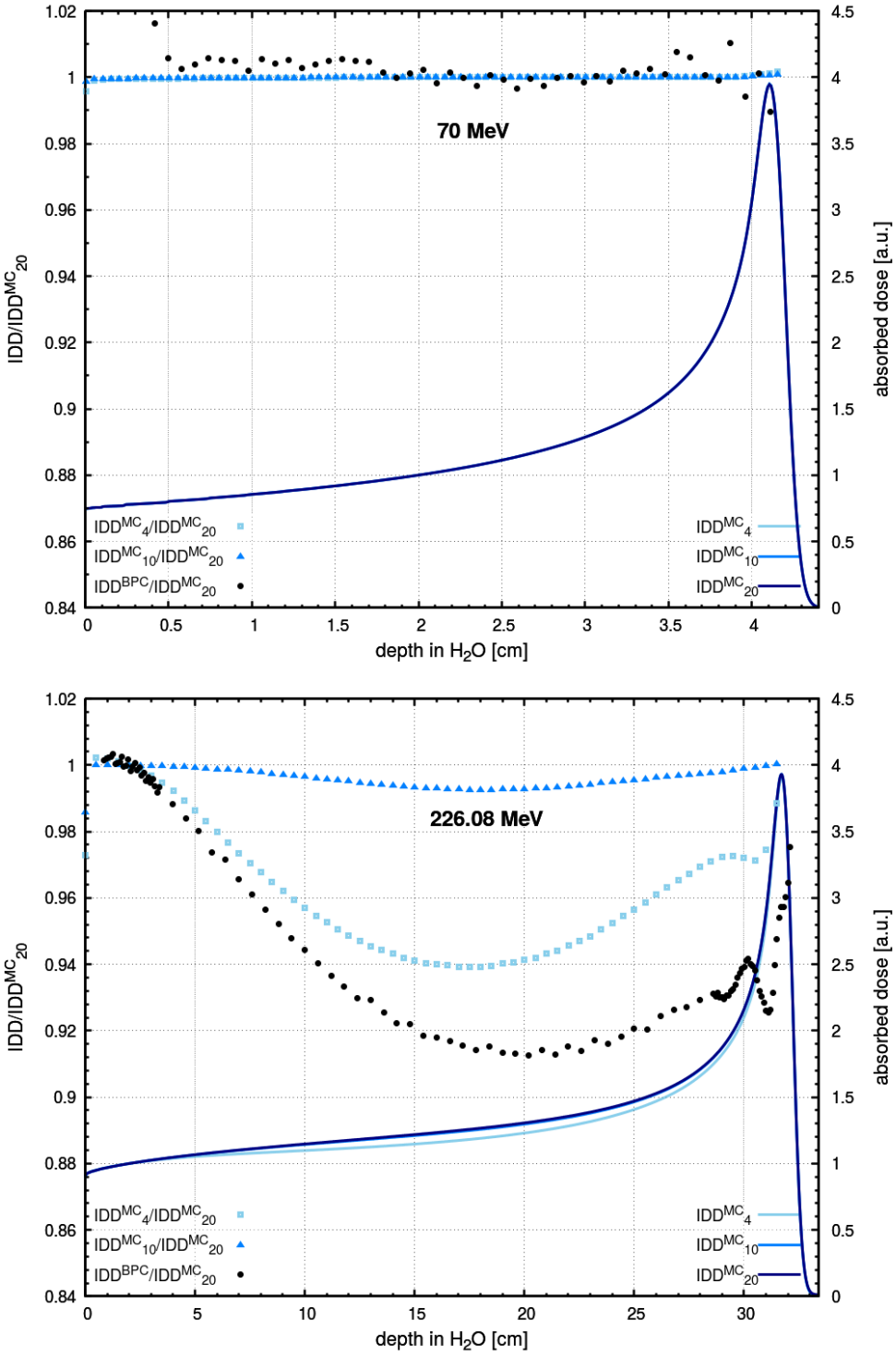

Figure 4.10. Ratio of the simulated IDD_4^{MC}/IDD_{20}^{MC} (light blue hollow squares), $IDD_{10}^{MC}/IDD_{20}^{MC}$ (blue triangles) and measured with BPC IDD^{BPC}/IDD_{20}^{MC} (black circles) distributions, normalised at 2 cm depth for two nominal beam energies: 70 MeV (top) and 226.08 MeV (bottom). Integral depth-dose distribution simulated with MC gantry beam model for three detector radii: $r = 4.08$ cm (IDD_4^{MC} -light blue), $r = 10$ cm (IDD_{10}^{MC} - blue) and $r = 20$ cm (IDD_{20}^{MC} - dark blue) correspond to the right axis. For 70 MeV IDD curves overlap with each other. For beam energy of 226.08 MeV IDD_{10}^{MC} and IDD_{20}^{MC} also overlap with each other. [Measurement data from PDKJ]

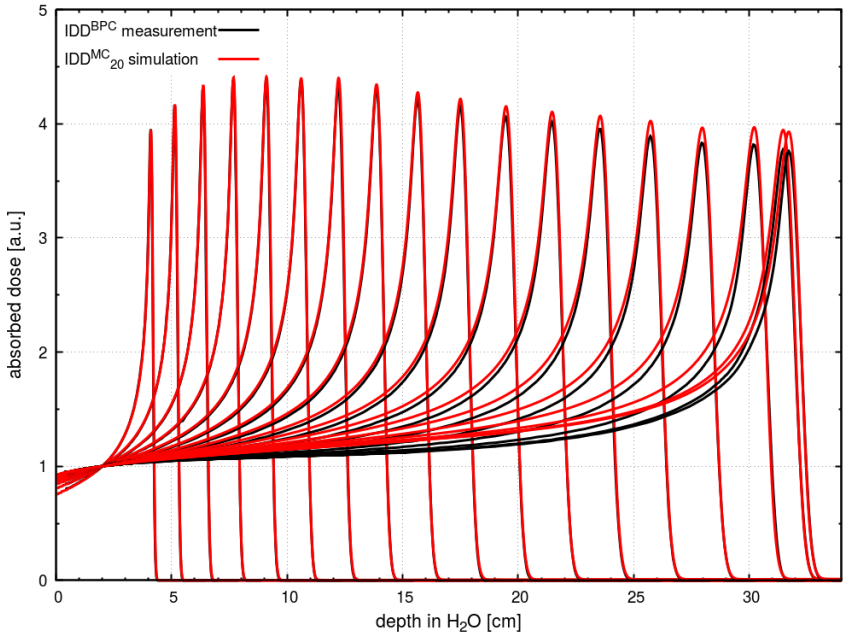

Figure 4.11. Depth-dose curves for GTR3 calculated with MC gantry beam model for detector size $r = 20\ cm$ (IDD_{20}^{MC} -red lines). For comparison, experimental data from the BPC (IDD^{BPC} - black lines) are plotted for 18 analysed nominal beam energies, normalised at 2 cm depth. [Measurement data from PDKJ]

region preceding the Bragg peak. It must be noted, however, that the depth-dose curves were normalised at 2 cm depth in water.

A set of 18 simulated $IDD_{20}^{MC}(E)$ curves is plotted in **Figure 4.11** together with experimental $IDD^{BPC}(E)$ distributions measured with the BPC detector ($r = 4.08\ cm$). All curves were normalised at the 2 cm depth. The additional dose from the long-distance nuclear interactions products is visible in the medium part of the BPs, for energies above 140 MeV ($R_{90} > 14.0\ cm$). The highest relative dose difference, calculated according to **Equation 2.7** with IDD_{20}^{MC} as reference, reached 8.8%, 6.1% and 1.4% for $IDD^{BPC}(E)$, $IDD_{4}^{MC}(E)$ and $IDD_{10}^{MC}(E)$, respectively for energy $E = 226.08\ MeV$.

4.3.3. Verification of the GTR beam model

Spot size in RW3 phantom

In **Figure 4.12** the mean spot size $\langle\sigma_{RW3}^{m-R}\rangle$ measured in the GTR3 in RW3 phantom with 2D TLD foils is shown as a function of depth recalculated for water depth equivalent. For all energies, a broadening of the beam is observed due to protons multiple-Coulomb scattering with maximum spot size prior to the Bragg peak depth. For the proton beam energies between 80 MeV and 225 MeV, the spot size at BP depth ranges between 5.4 mm and 6.6 mm, regardless the entrance spot size. Corresponding spot sizes calculated in the FLUKA code $\langle\sigma_{RW3}^{s-R}\rangle$ with MC GTR3 beam

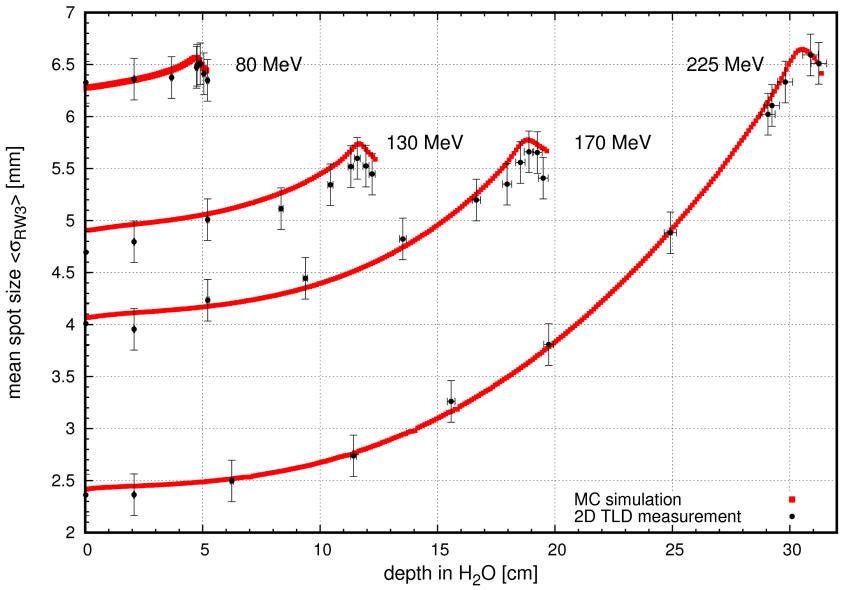

Figure 4.12. Calculated spot size $\langle \sigma_{RW3}^{s-R} \rangle$ (red squares) simulated in RW3 phantom, recalculated for water equivalent depth for GTR3 MC beam model. Mean spot size measured with 2D TLD foils $\langle \sigma_{RW3}^{m-R} \rangle$ are marked with black circles - data from [Gajewski, 2016].

model are also shown, with maximum spot size difference below 0.3 mm and mean difference of 0.1 mm.

TPS beam model verification

9 box-shape treatment plans with varying range, modulation and field size were analysed for calculated point dose comparison in the Eclipse TPS. 2% dose uncertainty was assumed as suggested in [Systems, 2013]. The top panel in **Figure 4.13** shows the dose differences obtained at $d = 2$ cm depth in the region proximal to SOBP. The relative dose differences between two beam models are relatively small, up to 1.8%. Higher dose differences are observed in the middle of the SOBP (middle panel in **Figure 4.13**) and at the end of the SOBP (bottom panel in **Figure 4.13**). For the analysed treatment plans, the dose difference does not change with the field size. The influential parameter is the distal range, as the dose envelope increases with the beam energy (as shown *e.g.* in **Figure 4.11**). Additionally, by increasing the SOBP modulation width, the number of pencil-beams rises, each contributing to the low-dose envelope component. The highest observed dose difference obtained from two TPS beam models reached 5.2% for 10 $cm \times 10$ cm field with 25 cm range and 20 cm modulation width (F10R25M20 plan).

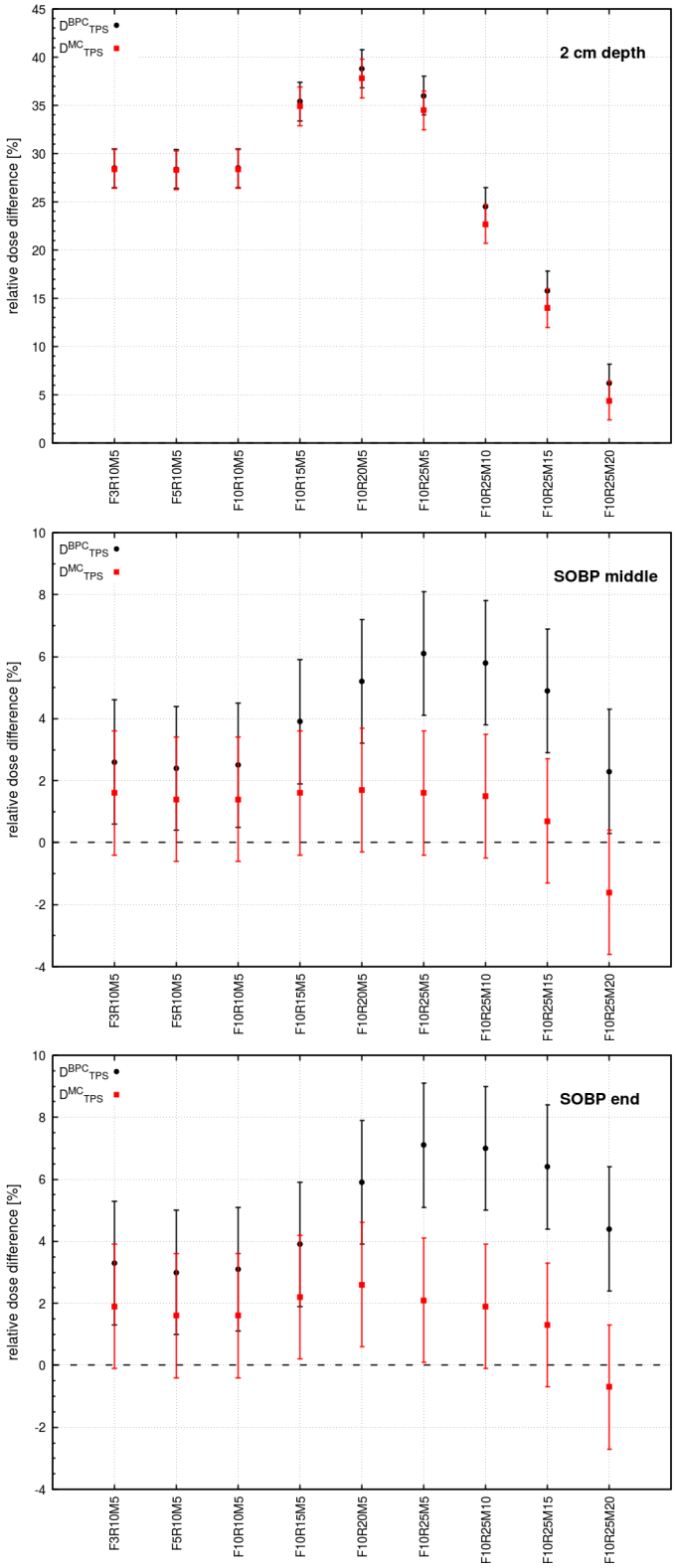

Figure 4.13. Relative dose difference calculated in the Eclipse TPS with IDD^{BPC}-based beam model (D^{BPC}_{TPS}, black circles) and with IDD^{MC}_{20}-based (D^{MC}_{TPS}, red squares) for single field treatment plans of given field size (F), range (R) and SOBP width (M). The dose was extracted at three depths: at the $d = 2\ cm$ (top panel), in the middle of the SOBP as $d = R - M/2$ (middle panel) and at the end of the SOBP as $d = R - 0.5\ cm$ (bottom panel). Data analysed with GTR4 beam model data.

4.4. Discussion

The aim of work presented in this chapter was to develop a reliable MC beam model of the GTR unit and calculate IDD distributions required in TPS commissioning for more precise dose calculation during the treatment planning process. In this section applicability of the FLUKA code is discussed for MC-based modelling of PBS proton beam. The obtained dose corrections from IDD calculations are analysed in terms of applied detector radii. Next, MC beam model improvements and further model verification are considered.

4.4.1. MC-based PBS modelling

For MC-based calculation of the dose distribution in PBS, two main MC codes were applied: MCNP(X) [Sawakuchi et al., 2010a] [Ardenfors et al., 2017] and Geant4/GATE [Clasie et al., 2012] [Grevillot et al., 2011]. The codes were tested against experimental data demonstrating overall good consistency with the experimental data, *e.g.* [Grevillot et al., 2011] [Sawakuchi et al., 2010a]. The FLUKA particle transport code has been broadly validated for PT applications, *e.g.* [Böhlen et al., 2014] [Battistoni et al., 2016]. Raster scanning has been modelled in FLUKA for synchrotron-based facility, *e.g.* [Parodi et al., 2010] [Parodi et al., 2012]. [Fiorini et al., 2018] employed FLUKA for cyclotron-based PBS modelling, though without chamber size correction calculation for the TPS beam model which excludes any comparison with the results of this work.

The empirically adjusted energy value in the FLUKA beam model E^{MC} exceeds systematically nominal beam energy E of $1 \div 2\ MeV$ as it was tailored to agree with the empirical R_{90} parameter. To shift the range, the mean excitation energy I can be modified from the user-level in the FLUKA code. It influences stopping power of protons, according to **Equation 1.4**. As it was shown in **Chapter 2.3.4**, ICRU-recommended value of $I = 75\ eV$ for water provides a constant range shift for nominal beam energies and was used in this work. Moreover, the nominal energy E is the estimated energy value at the room entrance, *i.e.* at the nozzle end and does not necessarily have to agree with particular energy-range tables. Therefore, the observed discrepancy between E^{MC} and E is acceptable.

The developed within this work MC gantry beam model was compared with BPC measurements for depth-dose profiles and with the Lynx PT measurements for lateral beam profiles in air, similarly to other works [Sawakuchi et al., 2010a] [Grevillot et al., 2011] [Ardenfors et al., 2017] [Clasie et al., 2012]. While no standard of the MC beam model is established, various beam parameters are reported from several research groups disabling for a full comparison.

As shown in **Figures 4.6-4.7**, the difference between measured and simulated range R_{90} was below 0.2 mm and for distal fall-off DFO_{80-20} difference was below 0.2 mm for 15 out of 18 analysed energies (apart from 3 highest energies where the DFO_{80-20} difference was below 0.5 mm). The obtained results are comparable with other MC-based PBS models: within 0.1 mm for R_{90} [Ardenfors et al., 2017]; R_{90} below 0.3 mm for $> 80\%$ of analysed points with maximum range difference of 0.6 mm in [Grevillot et al., 2011].

The difference between simulated and measured peak widths $FWHM_{BP}$ was within 0.2 mm being much smaller than 1.5 mm reported by [Sawakuchi et al., 2010a].

In **Figure 4.9** the measured and MC-simulated $max/plateau$ ratios are plotted as a function of proton energy, with maximum difference below 0.2. The highest difference of 0.15 is observed for 225 and $E = 226.08\ MeV$, calculated between the dose at the BP depth and plateau dose at 2 cm depth. The beam parameter $max/plateau$ ratio is either not specified in the literature or in the specification integration volume or shape in formations are missing. The reason for the observed discrepancy might be two-fold: the discrepancies in peak and plateau dose, as follows.
For the peak dose spot size at the Bragg peak depth for CCB high energy pencil-beam would be around $\sigma_{BP}(E = 225\ MeV) \approx 6.6\ mm$. Following [Grevillot et al., 2011], $\pm 3\ \sigma$ gives 39.6 mm, taking into account 99.7% of primary protons which is half below BPC diameter of $\varnothing_{BPC} = 81.6\ mm$. Therefore, additional dose shown in MC may not originate from scattered primary protons but rather from non-elastic hadronic collisions and light fragments not registered by the chamber [Grevillot et al., 2011]. This would generate higher $max/plateau$ ratio for the MC calculated curves, increasing with beam energy as does the fraction dose from the nuclear interactions, shown by [Pedroni et al., 2005].
On the other hand, the dose increase at the entrance region of the DDD is caused by the contamination of the primary beam with secondary particles, mainly low-energy protons and neutrons produced in the nozzle due to the scattering on the specific beam line components [Sawakuchi et al., 2010a] [Lin et al., 2014].This effect is observed at CCB as measured entrance dose is higher when compared to the TPS-calculated values. In other PT facilities in Europe the same effect has been observed with various solutions proposed. One of the approaches proposed in MC PBS modelling is the insertion of the constant low-energy component up to the beam energy [Ardenfors et al., 2017] [Grassberger et al., 2015], which may be considered as the enhancement of the MC gantry beam model with single Gaussian energy distribution.

For lateral spot size in-air, differences between measured at the CCB and simulated values did not exceed 0.1 mm for the isocentre plane. The agreement was better or comparable with other MC-based PBS models: within $\pm 0.7\ mm$ for 5 positions around the isocentre (mean difference of 0.1 mm) by [Ardenfors et al., 2017]; within 0.15 mm for 27 analysed energies [Grevillot et al., 2011].

It must be noted that the MC gantry beam model presented here was simplified. Modelling of beam waist (as discussed below in **Section 4.4.3**) was omitted, with zero divergence beam simulations referring only to the measurements performed at the isocentre plane. Moreover, no nozzle modelling was attempted due to limited access to the nozzle specification, similarly to other groups [Grevillot et al., 2011]. No additional FLUKA code modifications were carried out to adjust the calculated results to the measured ones. Nonetheless, the obtained results agree with experimental data and are comparable with other proton therapy facilities. Hence, the good reproducibility of the experimental data obtained from the MC simulations justifies FLUKA relevance in PBS modelling of the cyclotron-based facility.

4.4.2. MC-based corrections to experimental data

For IDD calculation of the Bragg peak, there is no standard for the virtual chamber radius calculated in the MC codes. Unquestionably, detector radius $r = 4.08\ cm$

referring to the commercially available BPC may eventually lead to dose discrepancies up to 10%, depending on the size of the target volume [Pedroni et al., 2005]. However, large detector radii, *e.g.* of $r = 25\ cm$ [Ardenfors et al., 2017], borders with phantom or human size limitations.

[Anand et al., 2012] indicated radial limit of the lateral pencil-beam integration. The radius was set to agree with 0.1% of the peak dose, with larger radii showing negligible influence on the IDD shape. This corresponds to 16.3 cm radius simulated with GTR3 beam model for the beam energy $E = 226.08\ MeV$ at depth of $d = 16\ cm$. This radius agrees with [Gottschalk et al., 2015] recommending rough value of 1/3 of the beam distal range to be the low-dose envelope range (thus for $E = 226.08\ MeV$ the dose halo reaches 11 cm from the beam axis). In [Mojżeszek et al., 2017b] the MC gantry beam model presented in this work was applied for calculation of the geometrical efficiency of ionisation chambers. For beam energy $E = 226.08\ MeV$, shown in **Figure 4.14**, drop in dose difference below 1% for detector radius above 10 cm is visible (read out at 16 cm depth in water). The detector size of $r = 20\ cm$ applied in this work for reference IDD_{20}^{MC} calculation shall account for secondaries from nuclear interactions with safe margin. For the measurements a large chamber radius is not always necessary, while dose difference stays below 1% for energies up to 140 MeV and 190 MeV, for commercially available chamber sizes of $r = 4.08\ cm$ and $r = 6\ cm$, respectively [Mojżeszek et al., 2017b].

As shown in **Figure 4.10** a dose difference of $IDD^{BPC}(E = 226.08\ MeV)$ and $IDD_4^{MC}(E = 226.08\ MeV)$ with reference to $IDD_{20}^{MC}(E = 226.08\ MeV)$ reaches 8.8% and 6.1%, respectively, which is in agreement with other reported MC-based BPC corrections of $7 - 8\%$ [Ardenfors et al., 2017] [Grevillot et al., 2011] [Clasie et al., 2012]. Obtained dose difference up to 1.4% for $IDD_{10}^{MC}(E = 226.08\ MeV)$ with reference to $IDD_{20}^{MC}(E = 226.08\ MeV)$, is identical to corrections of 1.4% dose difference for $r = 10\ cm$ and $E = 221.8\ MeV$ reported by [Sawakuchi et al., 2010a]. For reliable IDD assessment, the need for a simulations with detector radius bigger than $r = 10\ cm$ has been proven.

4.4.3. Improvements of the MC gantry beam model

Introducing pencil-beam waist

As shown in **Figure 4.4**, the assumption of zero angular beam spread in the FLUKA code was sufficient to obtain a difference below 0.1 mm in spot size (σ) for all analysed energies at the isocentre. The reason for omitting divergence modelling in the FLUKA code was not equivocal experimental data from the Lynx PT measured at 5 positions along the beam axis with gantry angle $\phi = 270°$, as presented in **Figure 4.15** for four exemplary beam energies of 80, 130, 170 and 225 MeV. Still, the experimental values of spot size as a function of the isocentre distance were taken as an input for the TPS beam model of the spot shape in-air. To expand the developed MC gantry beam model with beam divergence parameters (θ_x^{MC}, θ_y^{MC}) more systematic measurements are required.

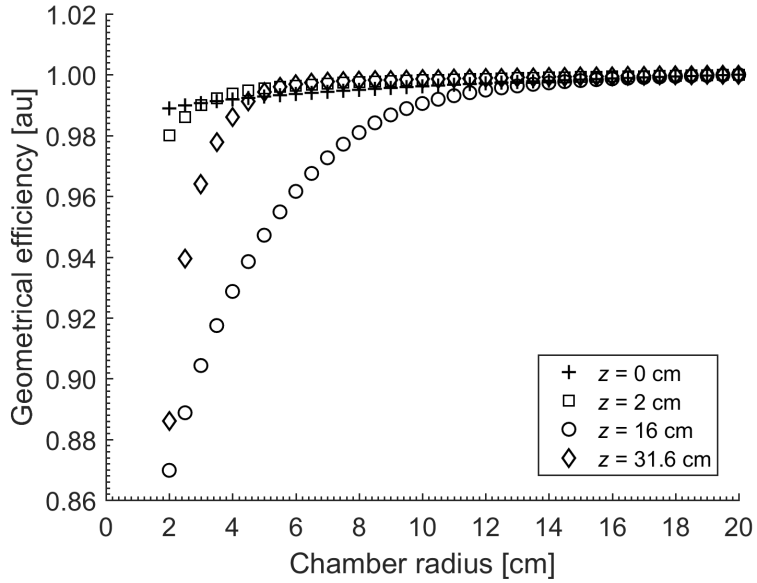

Figure 4.14. Geometrical efficiency of the chamber calculated as ratio between $IDD_r^{MC}(z)$ and $IDD_{20}^{MC}(z)$ as a function of detector radii for various depths in water (z) simulated for 226.08 MeV nominal proton beam with MC GTR3 beam model from this thesis. Reprinted from [Mojżeszek et al., 2017b]]

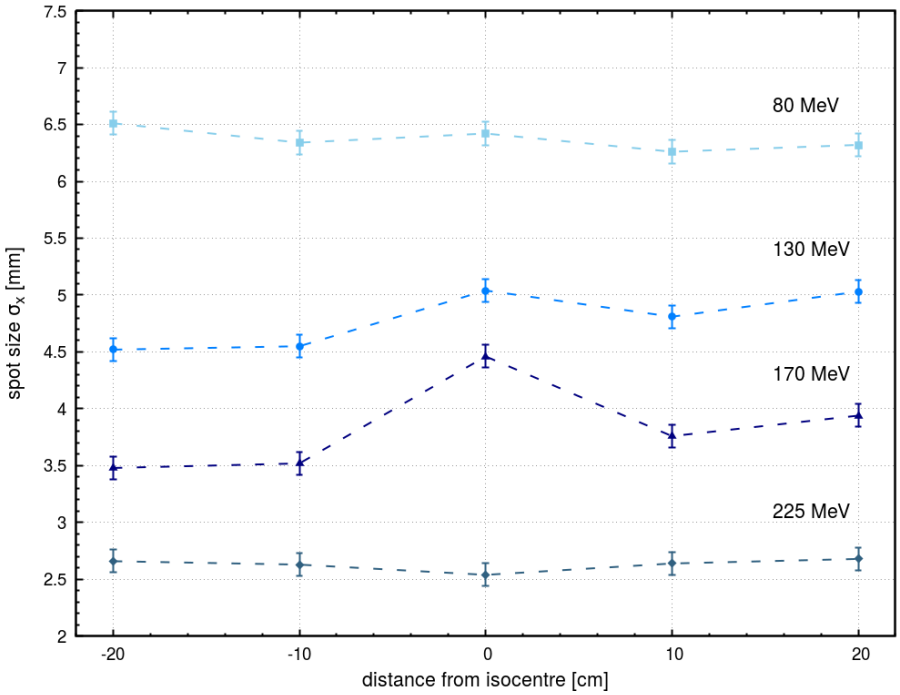

Figure 4.15. Spot size (σ_x) measured in-air with the Lynx PT detector at several distances from the isocentre, along the beam axis for 4 therapeutic proton beam energies and gantry angle $\phi = 270°$. The corresponding dotted lines are only guide to the eye. [Data adopted from PDKJ measurements]

Introducing higher Gaussian components - 2G model

It was observed that omitting in calculation the low-intensity tails around the spot can result in dose underestimation for shallow depths, especially for higher beam energies [Ardenfors et al., 2017].It was proposed in the literature that the low energy tail may be parametrised by a double-Gaussian function [Sawakuchi et al., 2010b].Since the tail intensity is typically $10^3 \div 10^6$ times lower compared to the spot centre [Grassberger et al., 2015] it cannot be determined with the Lynx PT, due to limited detector sensitivity.

At GTR3, PDKJ group measured these dose tails of pencil beams in air with highly sensitive TLD MCP detectors, positioned in the PMMA plate perpendicularly to the beam axis [Krzempek et al., 2016]. The measurements were performed for energy range $70 \div 220\ MeV$, every $20\ MeV$, and for $225\ MeV$. For each energy, 5 positions along the beam axis with regard to the isocentre,were selected: at $z = 0\ cm$, $\pm 10\ cm$ and $\pm\ 20\ cm$, in order to improve the required lateral beam shape input data for the Eclipse TPS. The TL detectors were placed every $2\ cm$ inside first Gaussian region ($[-3.5\ cm : 3.5\ cm]$) and every $7\ mm$ beyond it ($[-14.5\ cm : -3.5\ cm]$;$[3.5\ cm : 14.5\ cm]$). The obtained results were then merged with Lynx PT profiles, interpolated and symmetrised for X and Y beam profiles, independently for X and Y. Missing beam energies were interpolated by piece-wise cubic Hermite interpolating polynomial in the MATLAB environment. Next, high-dose profiles from the Lynx PT measurements, described in **Section 4.2.1**, together with MCP-based low-dose tails were parametrised by Varian Medical Systems Inc. team and introduced to the Eclipse ver. 13.6 TPS as a new beam model called $TPS - 2G$, with first and second Gaussian weights dedicated for each spot as a function of energy.

To verify the influence of the secondary Gaussian component on the depth-dose distribution, a 2^{nd} Gaussian component was introduced in the source of the MC gantry beam model. For this purpose, $\sigma_x^{MC-2G}(E)$ and $\sigma_y^{MC-2G}(E)$ were empirically adjusted to fit the MCP measured curves for 16 proton beam energies $70 \div 220\ MeV$ with $10\ MeV$ step. The number of primary protons was increased from 5×10^6 in 25 runs to 10×10^6 in 30 runs to assure statistical uncertainty level below 2% for the halo region of the spot. Preserving the same configuration of the scoring region (the same as for the Lynx PT, described in **Section 4.2.2**), the output files were then merged with results from the MC gantry beam model developed within this work, here called $1G$ model. For each energy, sum of two dose distributions with corresponding weights taken from the TPS parametrisation formed double Gaussian MC model of the GTR3 beam, denoted as $2G$ model. The selected results for the profile Y changes between $1G$ and $2G$ MC beam model are shown in **Figure 4.16** for $80\ MeV$, $150\ MeV$ and $220\ MeV$ proton beam energies. Implementing the 2^{nd} Gaussian component to the spot profile enhances the dose at the distance of $2 - 3\ cm$ from about 0.01% to 0.1% of the maximum dose at the spot centre. The introduced secondary Gaussian component in $2G$ model does not take into account low dose tails above $8\ cm$ for energies $E \geq 100\ MeV$.

For the developed double-Gaussian MC beam model, IDD_4^{MC-2G}, IDD_{10}^{MC-2G} and IDD_{20}^{MC-2G} were simulated to check its influence on the overall depth-dose profile shape. The results are presented in **Figure 4.17** as $2G/1G$ ratio of the integral

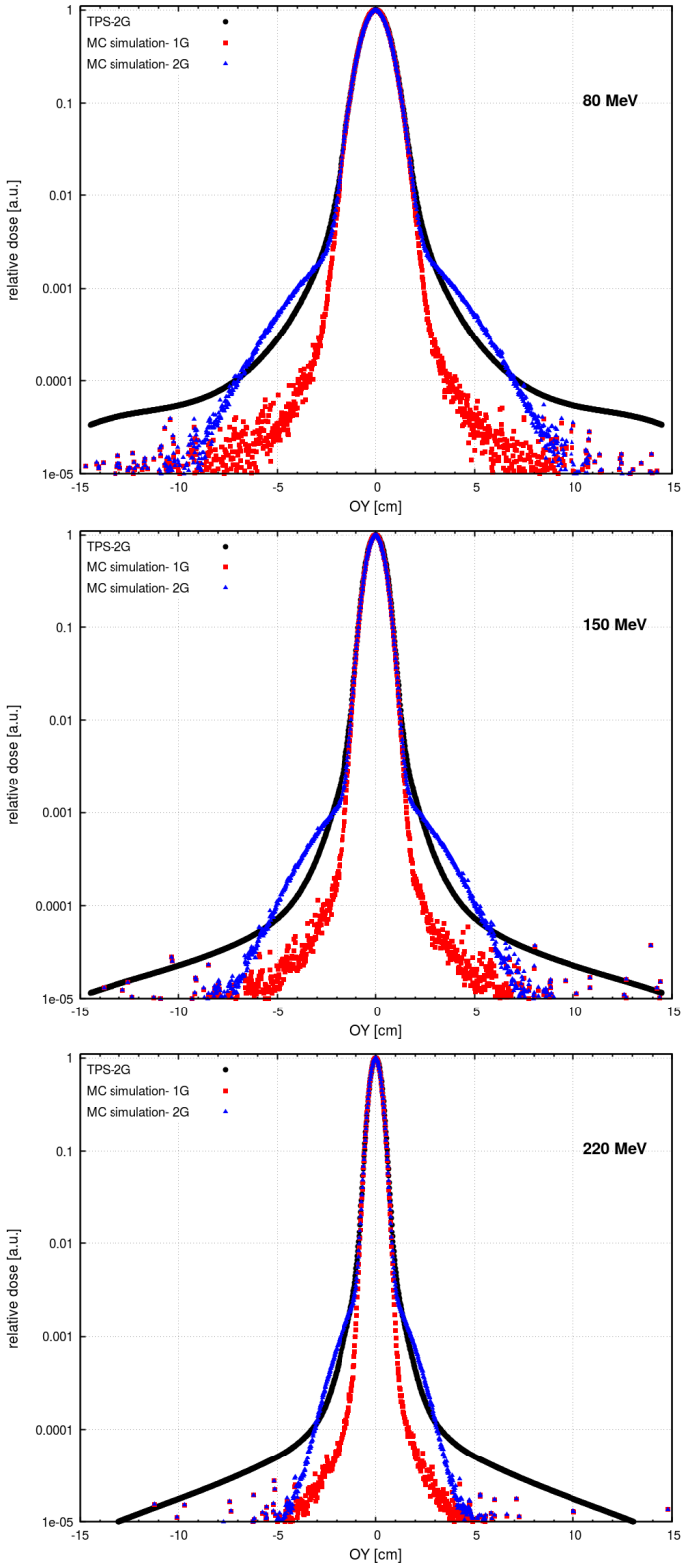

Figure 4.16. Lateral dose profile of the 80 MeV (top), 150 MeV (middle) and 220 MeV (bottom) proton beam for 1G and 2G MC beam model, in red squares and blue triangles, respectively. The simulation data are compared with beam shape calculated in TPS (black circles), based on Lynx with TLDs measurements ($TPS - 2G$) [Krzempek et al., 2016].

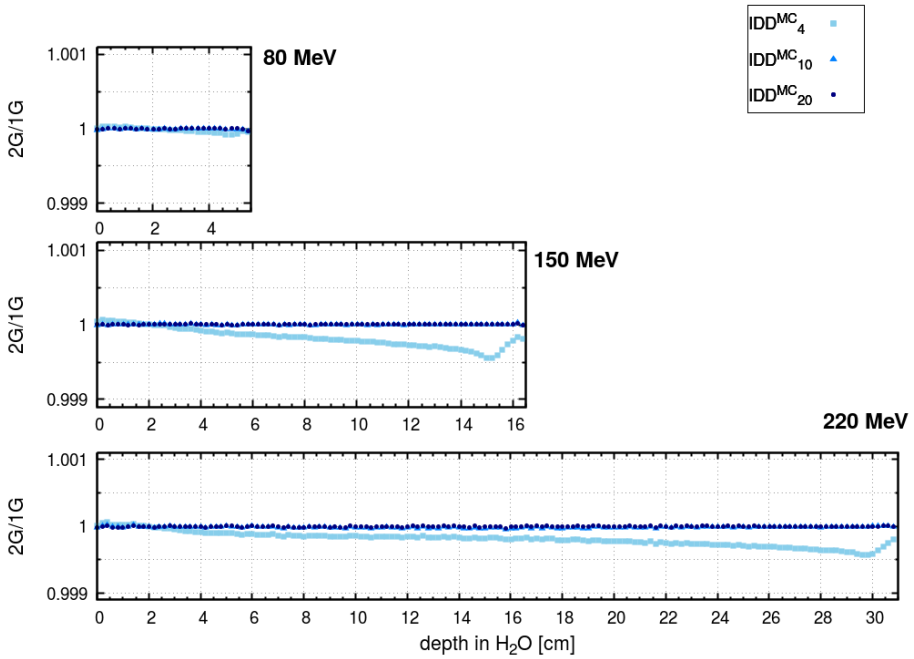

Figure 4.17. Ratio of $IDD(E)$ distributions calculated with 2G and 1G MC beam models for three detector radii: 4.08 cm (IDD_4^{MC} - light blue squares), 10 cm (IDD_{10}^{MC} - blue triangles) and 20 cm (IDD_{20}^{MC} - dark blue circles) and for three proton beam energies (80 MeV -top, 150 MeV - middle, 220 MeV - bottom). For IDD_{10}^{MC} and IDD_{20}^{MC} the curves overlap with each other.

depth-dose distributions (*e.g.* $IDD_4^{MC-2G}/IDD_4^{MC-1G}$) for three energies: 80 MeV, 150 MeV and 220 MeV. Only for IDD_4^{MC} $2G/1G$ model comparison dose differences are visible, increasing with the beam energy. However, the maximum dose difference between two models does not exceed 0.1% for the highest beam energy $E = 220$ MeV for a detector radius of $r = 4.08$ cm. For bigger detector sizes the effect is diminished. From the results obtained by [Gillin et al., 2010] MC calculated correction factor for IDD curves at 2 cm depth was of 1.14 for 72.5 MeV and of 1.01 for 221.8 MeV. Higher values were obtained for synchrotron-based facility [Gillin et al., 2010]. An additional reason for the discrepancy may be caused by different fractions of secondary particles scattered in the nozzle or unlike spot shapes being specific to each site configuration [Ardenfors et al., 2017]

Based on the above-mentioned simulation results, the 2^{nd} Gaussian beam component (described by $\sigma_x^{MC-2G}(E)$ and $\sigma_y^{MC-2G}(E)$) was found to have negligible impact on the $IDD(E)$ curves and was not introduced to the developed MC gantry beam model. Nevertheless, in the Eclipse ver. 13.6 TPS, $TPS - 2G$ model of the lateral beam shape acquired with TLD measurements serve as basis for the TPS beam model definition, applied for patient treatment planning.

4.4.4. MC beam model verification against TPS-calculated and measured data

The comparison between two TPS beam models, BPC-based and MC-based, shown in **Figure 4.13** illustrates how chamber size correction affects the dose calculation. The estimation of the true dose correction introduced by MC-calculated IDD_{20}^{MC} curves presented in this work cannot be directly related to the measured data. This is mainly due to the fact that the Eclipse TPS applies analytic models for dose calculation to speed the dose calculation of the TPS, where only several characteristic points from the physical input data are used.

It would also be valuable to show a comparison between experimental data, TPS plan and MC simulation results, especially for box-shaped SOBPs or, even more interesting, for patient treatment plans, where additive effect of the small dose corrections may lead to large dose discrepancies [Sawakuchi et al., 2010a] [Grevillot et al., 2011]. This requires, however, additional corrections for both the TPS and current MC gantry beam model.
From the TPS side this improvement is termed as field size effect, with correction dependent on the target volume, introduced customarily as a separate table (*e.g.* field size factor in [Grevillot et al., 2011]). For the Eclipse TPS beam model of the CCB beams correction due to the field modulation width and distal range was introduced as depth-dose normalisation correction factor (DDNCF) table [Pędracka et al., 2016]. Possible improvement of the MC gantry beam model requires better modelling of the spot shape (*cf.* **Section 4.4.1**) and introduction of direction cosines of the source particles for non-single pencil-beam calculations. Moreover, for absolute dose comparison, calibration of the MC results would be required. Though beyond the scope of this work, extensive TPS, improved MC beam model and comparison with measurements, *e.g.* as carried out by [Grevillot et al., 2011], could lead to the application of the developed MC beam model as a complementary tool in *e.g.* individual patient dosimetry.

4.5. Conclusions

In the FLUKA code, the MC beam model of the CCB gantry treatment room has been developed. It was validated against measured data, both for lateral and depth-dose distributions. In-air spot sizes at the isocentre were consistent within $\pm 0.1\ mm$ for σ_x and σ_y parameters. For depth-dose profiles, analysed beam parameters (R_{90}, $FWHM_{BP}$, DFO_{80-20}) agreed within $\pm 0.3\ mm$ or within ± 0.2 ($max/plateau$ ratio) interval, except for 3 highest energies, where DFO_{80-20} difference was below $0.5\ mm$, similarly for GTR3 and GTR4 MC beam model. The GTR3 expemplary FLUKA input file for BPC measurement simulations was enclosed in **Appendix B**. The developed GTR3 beam model parameters can be found in **Appendix C**.

FLUKA MC code was found adequate for development of the MC gantry beam model. The implemented physics of proton interactions was cross-checked with spot size measurements in the RW3 phantom and with the BPC measurements in water. For spot size in the RW3 phantom, analysis of 2D TLD images stayed within $\pm 5.5\%$ agreement to the simulated beam size values. For depth-dose IDD_4^{MC} curves in water, differences did not exceed 6% when compared to IDD^{BPC} data for dose normalised at

2 cm depth. The difference obtained might be due to the normalisation point or to MC beam model simplifications made on the definition of the source energy distribution.

The established MC gantry beam model was used for the simulation of the IDD_{20}^{MC} distributions. Calculated IDD_{20}^{MC} curves were introduced as input data for the Eclipse TPS beam model which led to dose correction up to 8.8% when compared with hitherto IDD^{BPC}-based TPS beam model. The maximum dose difference between BPC-based and MC-based TPS beam models was 5.2% for box-shape plans calculated in the Eclipse TPS.

The gantry beam model developed in the FLUKA MC code was validated and applied for the GTR3 and GTR4 treatment rooms of the CCB facility. Implemented model lead to better agreement between the dose measured and calculated in the TPS. Since 2016 treatment plans of all patients at CCB are performed with Eclipse ver. 13.6 TPS commissioned with curves of the MC beam model prepared within this work. Additionally, developed MC gantry beam model was applied in CCB for resolving dosimetry issues, as follows.

One of them was the estimation of the ion recombination factor (k_s) calculated for CCB gantry PBS system done by [Liszka et al., 2018]. The MC gantry beam model presented in this work was applied to estimate single spot contribution to the absolute dose in water measured by the Markus ionisation chamber (PTW) positioned at the isocentre at 2 cm plateau depth in water, in a 10 $cm \times 10$ cm irradiation field with 2.5 mm spot spacing. The evaluated ion recombination corrections were found to be substantial for the obtained gantry high dose rates (1.18 Gy/s at 70 MeV, 6.57 Gy/s at 150 MeV, and 13.40 Gy/s at 225 MeV) [Liszka et al., 2018].

The effect of spot shape distortion introduced to the MC gantry beam model developed in this work was investigated in [Kłodowska et al., 2016]. The effect appears when the spot is rotated, and spot major and minor axes do not cover with the in-room coordinate system. The rotated spot may preserve the identical spot size σ as those defined in the TPS, but in fact has a different shape *e.g.* due to specific gantry position. In the FLUKA code, spot asymmetry was introduced to the MC gantry beam model, by varying the spot size up to 50% in width (σ) and up to $\alpha = 45^{\circ}$ of spot rotation, while preserving the volume integral under the spot curve [Kłodowska et al., 2016]. The simulation results showed the need of spot measurements for different gantry angles with *e.g.* 2D TLD foils (IFJ PAN), considered in detail by [Gajewski, 2016].

The present MC gantry beam model was also used for the calculation of the geometrical efficiency of the commercially available ionisation chambers, analysed in detail by [Mojżeszek et al., 2017b] [Mojżeszek, 2018]. The MC study showed no need for MC correction for the chamber size up to 150 MeV for chamber of radius $r = 4.08$ cm (like BPC from PTW) and up to 190 MeV for chamber radius $r = 6$ cm (like Stingray, IBA Dosimetry).

With suggested improvements to the current MC gantry beam model, it can be used as a tool for dosimetric study on the beam modification, *e.g.* additional beam collimation or minimising the nozzle-to-patient distance for minimising the proton scattering in air. It can be also the source of an additional TPS plan verification - *e.g.* in case of large inhomogeneities due to implants. MC models are also employed for state-of-the-art *in-vivo* PET verification of dose delivery position by simulating the signal from radioactivity induced by proton beam in the target volume.

Chapter 5

Summary and outlook

5.1. Summary

Radiotherapy with light ions results in better tumour dose conformation concomitantly with a lower integral dose delivered to healthy tissues. Advantages of the dose deposition linked with the development of the medical technologies (accelerators in medicine, diagnostics, patient positioning and monitoring during the treatment) have led to a growing number of hadron therapy facilities world-wide, especially proton therapy facilities. The Pencil Beam Scanning technique has become a new state-of-the-art standard in proton radiotherapy, available in a growing number of facilities world-wide [`www.ptcog.ch`]. As this technique is relatively new, no broadly-accepted standard is known for PBS beam commissioning, forcing each treatment site to establish its own commissioning strategy. Specific dose distribution demands more complex quality assurance procedures in terms of dosimetry and treatment planning. Complementary to dosimetric procedures applied so far, the dedicated Monte Carlo (MC) methods have demonstrated their potential for helping in the assessment of the required quantities, shortening the required beam-time burden to derive the correction factors for the measured data, in the design of the beam line and for radiation protection purposes. Although the MC-based beam model for treatment units has become a common practice reported in the literature, no clear method of MC beam model development and validation has been described so far in details.

Within this work, beam models for CCB therapeutic units (eye line ELTR and gantry GTR) were derived with the FLUKA MC code. The models advancement have been described step-by-step, separately for passively scattered beams and scanned pencil-beams. Characteristic beam parameters were selected from the experimental lateral and depth-dose distributions to establish the source parameters such as the beam energy E^{MC}, beam momentum spread $(dp/p)^{MC}$ and spot size σ_x^{MC}, σ_y^{MC},

for ELTR and GTR respectively. The models were cross-checked against the beam range R_{90}, distal fall-off DFO_{90-10} or DFO_{80-20}, Bragg peak width $FWHM_{BP}$, $max/plateau$ ratio between the maximum and entrance dose, spot size σ in-air and in medium at several depths. Beam parameters of R_{90}, DFO_{90-10} or DFO_{80-20}, $FWHM_{BP}$ agreed within ± 0.2 mm. Spot size σ agreed within $\pm 0.2mm$ for ELTR and within ± 0.1 mm for GTR, both for the in-air calculations. For GTR3, difference in spot size measured with 2D TLD foils and calculated in the RW3 solid phantom did not exceed 0.3 mm. Agreement in $max/plateau$ ratio for GTR was within ± 0.2. Beam models defined in the FLUKA code have been made available in **Appendices A** and **B**. Source parameters of the simplified GTR3 beam model are available in **Appendix C**.

The ELTR beam model was used for the analysis of single and double scattering systems in multiple configurations: with single Ta foil, with two Ta foils or with dual ring scatterer defined as Ta disk surrounded by PMMA ring. Various scatterer thicknesses ($20 \div 90$ μm of Ta) and disk radii ($3 \div 7$ mm) were considered. Optimised beam parameters were extracted from the beam lateral and depth-dose distributions: lateral penumbrae, lateral profile flatness, lateral field width and the maximum dose. The most convenient set-ups in terms of the analysed beam parameters were selected: single foil of 60 μm Ta, two foils of 25 μm and 60 μm Ta and dual ring of $r = 6$ mm 80 μm Ta disk with 1 mm PMMA ring. The maximum dose for the double scattering set-up was up to 28% higher when compared to single scattering set-ups $1 - 2$ and to 33% higher when compared to the current ELTR scattering system. Additionally, the selected scattering set-ups were tested in case of beam misalignment: in beam shift of $\Delta x = 0.5$ or 1 mm and in spot size change of $\Delta\sigma \pm 10\%$, introduced in the simulations. The dual ring solution turned out to be the most sensitive to beam misalignment, exceeding the acceptable level of field flatness. This analysis enabled to define beam misalignment limits under which clinical beam constraints of the scattered beam are fulfilled.

With the established GTR3 and GTR4 beam models, the integral depth-dose (IDD) distributions were calculated for 18 beam energies between 70 and 226.08 MeV, with lateral detector radius of $r = 10$ cm and $r = 20$ cm. The maximum dose difference between the simulated and measured IDD was 8.8% for nominal beam energy $E = 226.08$ MeV. Measurement-based and simulation-based TPS beam models, compared in Eclipse ver. 13.6 TPS, led to a maximal dose difference of 5.2%. The calculated IDD curves of $r = 20$ cm were taken as an input for commissioning of the Eclipse TPS. Since 2016, cancer patients of CCB have been successfully treated within this TPS beam model.

The FLUKA MC code was found relevant for modelling proton beam transport in the field of proton radiotherapy. MC-based beam models were developed for CCB therapeutic beams: a fixed beam at ELTR and a rotating beam of GTR (within this thesis only GTR3 beam model was shown). For the ELTR, the scattering system was optimised. For GTR, the dose corrections of the depth-dose distributions were calculated and used for the Eclipse TPS commissioning.

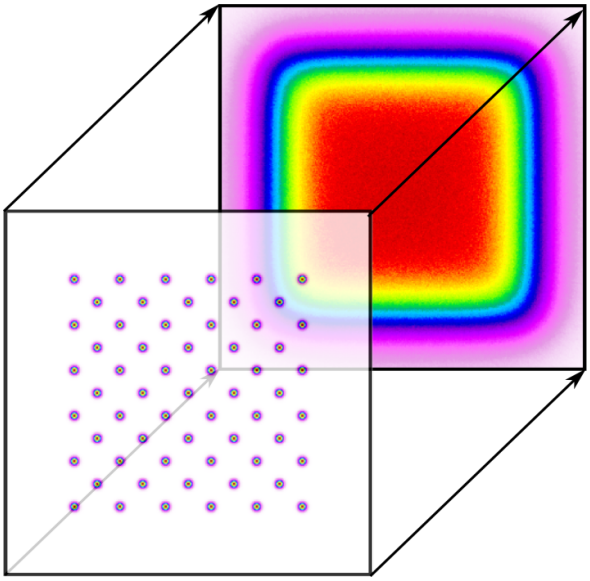

Figure 5.1. A scheme of proton MRT concept with narrow pencil-beam at the entrance resulting in homogeneous dose distribution at the desired depth. Details are given in [Kłodowska et al., 2015].

5.2. Outlook

The development of the ELTR and GTR MC-based beam models not only enabled this work to answer current dosimetry requests, but could in the future facilitate research at the CCB beam lines.

Similarly to synchrotron-based microbeam radiation therapy (MRT) with highly collimated photon beams [Bräuer-Krisch et al., 2010], a concept of proton micro- and mini-beam therapy has been proposed [Prezado and Fois, 2013] [Kłodowska et al., 2015]. In this technique, the dose can be delivered in spatially spaced narrow beams which overlap in the target volume. Healthy tissues preceding the tumour irradiated with spatially spaced beams show a reduced probability of the normal tissue complications. Due to proton scattering, dose peaks and valleys at the tumour depth diminish [Kłodowska et al., 2015], as is schematically shown in **Figure 5.1**. In proton therapy of eye melanoma, grid therapy might be beneficial for patients irradiated through the eyelid in case they cannot keep their eyelid open during the irradiation. For this approach a special grid collimator was proposed for ELTR to produce a set of parallel microbeams [Tobola-Galus et al., 2018].

The simplified GTR beam model might be further improved, as discussed in **Chapter 4.4**. This includes modelling of the beam waist, extension of the single Gaussian spot shape or introduction of the beam direction cosines to reproduce pencil-beam scanning mode of the gantry beam. The goal of such work would be a separate and precise tool for the TPS plan verification especially in case of large inhomogeneities within the patient body like in head and neck cases or implants [Grevillot et al., 2011].

The MC-calculated dose distributions are used for PET verification, as shown by [Parodi and Enghardt, 2000]. The MC gantry beam model can also be used for dosimetric studies such as additional beam collimation or the nozzle-to-patient distance

minimisation. To speed up the calculation time strain, GPU-based MC codes are favourable. At CCB, the FRED TPS [Schiavi et al., 2017] is benchmarked for this purpose [Ruciński et al., 2017].

Within the European Radiation Dosimetry Group (EURADOS) [`www.eurados.org`], Working Group 9 (WG9) *Radiation dosimetry in radiotherapy i.a.* deals with measurements of the stray radiation generated during proton radiotherapy. Results of the experimental campaign in the PBS facility ATreP (Trento, Italy) were reported by [Farah et al., 2015] and by [Stolarczyk et al., 2018] and compared to the results of the simplified MC simulations. The measurements were continued at CCB, in Kraków in 2014. The RW3 slab phantom was irradiated in PBS mode with various beam ranges, field sizes and SOBP modulation widths and stray neutron doses were measured [Mojżeszek et al., 2017a]. The application of the GTR beam model is planned for further assessment of patient exposure to the stray radiation, currently neglected in the TPS dose calculations.

Moreover, experimental campaign of WG9 for grid therapy with the PBS technique took place at the CCB in *Sept.* 2018. For the evaluation of the obtained dose distributions, the MC-based GTR beam model will be a valuable tool.

Appendix A: FLUKA file example for ELTR geometry

The exemplary FLUKA file given below contains the geometry of the ELTR dual ring set-up of the double scattering technique. The $S2$ scatterer consists of $r = 6\ mm$ $80\ \mu m$ Ta disk with a $1\ mm$ PMMA ring. The geometry includes: titanium vacuum window ($VacWin$), PMMA range shifter (RS), PE biological shield ($neutro$), steel snout with an aluminium base ($snout$) and brass collimator for $\varnothing 35\ mm$ field collimation ($col35$). The absorbed dose is calculated in a Cartesian grid in the water phantom positioned 202 cm from the vacuum window.

```
   TITLE phd_appA.inp
GLOBAL 1.0 1.0
DEFAULTS HADROTHE
BEAM -0.0702 -0.003931 -3.0 -0.91 -0.91 1.0PROTON
BEAMPOS 0.0 0.0 -290.00 0.0 0.0
GEOBEGIN COMBNAME
0 0
SPH blkbody 0.0 0.0 0.0 100000.0
SPH void 0.0 0.0 0.0 10000.0
BOX surround -200.0 -200.0 0.0 400.0 0.0 0.0 0.0 400.0 0.0 0.0 0.0 500.0
RPP VacWin -5.0 5.0 -5.0 5.0 -0.0050 0.00
RCC scatt2a 0.00 0.00 60.00 0.0 0.0 0.10 2.5
RCC scat2air 0.00 0.00 60.0080 0.0 0.0 0.092 0.6
RCC scatt2b 0.0 0.0 60.00 0.0 0.0 0.008 0.6
RPP rs -5.0 5.0 -5.0 5.0 19.0 19.47
RPP neutro -25.00 25.00 -21.50 20.00 63.00 103.00
RCC nHole 0.0 0.0 63.00 0.0 0.0 40.0 3.5
RCC snout1a 0.00 0.00 177.5 0.00 0.00 18.0 2.75
RCC snout1b 0.00 0.00 177.5 0.00 0.00 18.0 2.0
RPP snout2 -11.5 11.5 -21.5 11.5 177.5 179.5
RPP waterman -10.0 10.0 -10.0 10.0 202.00 222.0
RCC col35 0.0 0.0 195.5 0.0 0.0 0.6 2.75
RCC col35air 0.0 0.0 195.1 0.0 0.0 1.0 1.75
RCC col35in 0.0 0.0 195.1 0.0 0.0 1.0 2.0
END
BLKBODY 5 +blkbody -void
VOID 5 +void -surround-VacWin
SOURR 5 (surround -neutro-snout1a -snout2 -scatt2a -rs
```

```
-waterman-col35-col35in)|(nHole|(snout1b-col35in)|col35air|scat2air)
VacWIN 5 +VacWin
SCATT2A 5 +scatt2a-scatt2b -scat2air
SCATT2B 5 +scatt2b
nShield 5 +neutro -nHole
RS 5 +rs
SNOUTbas 5 +snout2 -snout1a
SNOUTpip 5 +snout1a -snout1b
K35 5 (+col35|col35in)-col35air
WATERMAN 5 +waterman
END
GEOEND
MATERIAL 1.19 Polymeth
COMPOUND 8.0 HYDROGEN 5.0 CARBON 2.0 OXYGENPolymeth
MATERIAL 30.  65.39 7.133 ZINC
MATERIAL 8.52 Brass
COMPOUND 62.0 COPPER 35.0 ZINC 3.0 LEADBrass
MATERIAL 24.  51.9961 7.18 CHROMIUM
MATERIAL 25.  54.938049 7.21 MANGANES
MATERIAL 15.  30.973761 1.82 PHOSPHO
MATERIAL 16.  32.066 2.07 SULFUR
MATERIAL 7.8 SS316LN
COMPOUND -0.67145 IRON -0.185 CHROMIUM -0.1125 NICKELSS316LN
COMPOUND -0.02 MANGANES -0.01 SILICON -0.00045 PHOSPHOSS316LN
COMPOUND -0.0003 SULFUR -0.0003 CARBON SS316LN
MAT-PROP 19.0 SS316LN DPA-ENER
ASSIGNMA BLCKHOLE BLKBODY
ASSIGNMA VACUUM VOID
ASSIGNMA AIR SOURR
ASSIGNMA TITANIUM VacWIN
ASSIGNMA POLYETHY nShield
ASSIGNMA Polymeth SCATT2A
ASSIGNMA Polymeth RS
ASSIGNMA ALUMINUM SNOUTbas
ASSIGNMA SS316LN SNOUTpip
ASSIGNMA WATER WATERMAN
ASSIGNMA TANTALUM SCATT2B
ASSIGNMA Brass K35
USRBIN 10.  DOSE -50.  2.5 0.05 202.1diode
USRBIN -2.5 -0.05 202.0 250.  1.  1.  &
USRBIN 11.  DOSE -51.  0.256 0.0 207.0Markus
USRBIN 0.0 0.0 202.0 1.  1.  500.  &
RANDOMIZ 1.  2018.
START 5000000.  0.0
STOP
```

Appendix B: FLUKA file example for GTR geometry

The exemplary FLUKA file given below contains the geometry of the GTR pencil beam of 70 MeV scored in water phantom. The walls of the water phantom are from PMMA, with a density of $\rho = 1.19\ g/cm^3$. The absorbed dose is scored in cylinders with three different radii: $r = 4\ cm$, $r = 10\ cm$ and $r = 20\ cm$.

```
   TITLE phd_appB.inp
GLOBAL 1.0 1.0
DEFAULTS HADROTHE
BEAM -0.07191 -0.002876 0.0 -1.4377 -1.3967 1.0PROTON
BEAMPOS 0.0 0.0 -100.01
GEOBEGIN COMBNAME
0 0
SPH blkbody 0.0 0.0 0.0 100000.0
SPH void 0.0 0.0 0.0 10000.0
RPP air -200.0 200.0 -200.0 200.0 -100.00 200.0
RPP surface -30.75 30.75 -32.25 32.25 -10.20 -2.00
RPP waterman -30.75 30.75 -32.25 32.25 -2.0 44.4
RPP walls -32.25 32.25 -33.75 33.75 -10.10 45.9
END
BLKBODY 5 +blkbody -void
VOID 5 +void -air
AIR 5 +(air -walls)|surface
WALLS 5 +walls-waterman-surface
WATERMAN 5 +waterman-surface
END
GEOEND
MATERIAL 1.19 PLEXIGLA
COMPOUND -0.080538 HYDROGEN -0.599848 CARBON -0.319614 OXYGENPLEXIGLA
MAT-PROP 74.0 PLEXIGLA
STERNHEI 3.3297 0.1824 2.6681 0.11433 3.3836 PLEXIGLA
ASSIGNMA BLCKHOLE BLKBODY
ASSIGNMA VACUUM VOID
ASSIGNMA AIR AIR
ASSIGNMA PLEXIGLA WALLS
ASSIGNMA WATER WATERMAN
USRBIN 11.  DOSE -50.  4.08 0.0 32.0R4cm
USRBIN 0.0 0.0 -2.0 1.  1.  3400.  &
USRBIN 11.  DOSE -51.  10.0 0.0 32.0R10cm
USRBIN 0.0 0.0 -2.0 1.  1.  3400.  &
```

```
USRBIN 11.  DOSE -52.  20.0 0.0 32.0R20cm
USRBIN 0.0 0.0 -2.0 1.  1.  3400.  &
RANDOMIZ 1.0 2018.
START 6000000.  STOP
```

Appendix C: MC beam model of GTR3

Energy	**source energy**	**source momentum spread**	**source spot size**	
$E\ [MeV]$	$E^{MC}\ [MeV]$	$(dp/p)^{MC}\ [\%]$	$\sigma_x^{MC}\ [mm]$	$\sigma_y^{MC}\ [mm]$
70	71.91	4.00	6.11	5.93
80	81.32	3.80	5.74	5.69
90	91.47	3.40	5.21	5.10
100	101.42	3.20	4.92	4.82
110	111.50	3.08	4.74	4.64
120	121.46	3.00	4.67	4.50
130	131.53	2.70	4.39	4.34
140	141.24	2.67	4.20	4.02
150	151.28	2.62	3.95	3.81
160	161.19	2.47	3.72	3.63
170	171.34	2.31	3.55	3.38
180	181.19	2.12	3.30	3.18
190	191.07	1.87	3.04	2.98
200	201.07	1.63	2.78	2.73
210	211.02	1.48	2.64	2.60
220	220.65	0.95	2.45	2.43
225	225.92	0.75	2.47	2.42
226.08	226.95	0.77	2.46	2.41

Bibliography

[Agostinelli et al., 2003] Agostinelli, S., Allison, J., Amako, K., Apostolakis, J., Araujo, H., Arce, P., Asai, M., Axen, D., Banerjee, S., Barrand, G., et al. (2003). Geant4—a simulation toolkit. *Nuclear Instruments and Methods in Physics Research Section A: Accelerators, Spectrometers, Detectors and Associated Equipment*, 506(3):250–303.

[Akagi et al., 2003] Akagi, T., Higashi, A., Tsugami, H., Sakamoto, H., Masuda, Y., and Hishikawa, Y. (2003). Ridge filter design for proton therapy at Hyogo Ion Beam Medical Center. *Physics in Medicine & Biology*, 48(22):N301.

[Allison et al., 2006] Allison, J., Amako, K., Apostolakis, J., Araujo, H., Dubois, P. A., Asai, M., Barrand, G., Capra, R., Chauvie, S., Chytracek, R., Cirrone, G. A. P., et al. (2006). Geant4 developments and applications. *IEEE Transactions on Nuclear Science*, 53(1):270–278.

[Amaldi and Kraft, 2005] Amaldi, U. and Kraft, G. (2005). Radiotherapy with beams of carbon ions. *Reports on Progress in Physics*, 68(8):1861.

[Anand et al., 2012] Anand, A., Sahoo, N., Zhu, X. R., Sawakuchi, G. O., Poenisch, F., Amos, R. A., Ciangaru, G., Titt, U., Suzuki, K., Mohan, R., and Gillin, M. T. (2012). A procedure to determine the planar integral spot dose values of proton pencil beam spots. *Medical Physics*, 39(2):891–900.

[Appleton and Bridge, 2010] Appleton, J. P. and Bridge, P. (2010). Comparing plaque brachytherapy and proton therapy for choroidal melanoma: a review of the literature. *Journal of Radiotherapy in Practice*, 9(1):53–61.

[Ardenfors et al., 2017] Ardenfors, O., Dasu, A., Kopeć, M., and Gudowska, I. (2017). Modelling of a proton spot scanning system using MCNP6. *Journal of Physics: Conference Series*, 860(1):012025.

[Attix, 1986] Attix, F. H. (1986). *Ionizing Radiation*. Wiley-VCH Verlag GmbH.

[Bakewicz et al., 2003] Bakewicz, E., Budzanowski, A., and Taraszkiewicz, R. (2003). AIC-144 cyclotron: present status. 48(Supplement 2):117–121.

[Bassler et al., 2014] Bassler, N., Hansen, D. C., Lühr, A., Thomsen, B., Petersen, J. B., and Sobolevsky, N. (2014). SHIELD-HIT12a - a Monte Carlo particle transport program for ion therapy research. *Journal of Physics: Conference Series*, 489(1):012004.

[Battistoni et al., 2016] Battistoni, G., Bauer, J., Boehlen, T. T., Cerutti, F., Chin, M. P. W., Dos Santos Augusto, R., Ferrari, A., Ortega, P. G., Kozłowska, W., Magro, G., et al. (2016). The FLUKA Code: An Accurate Simulation Tool for Particle Therapy. *Frontiers in Oncology*, 6.

[Berger et al., 2009] Berger, M., Coursey, J., Zucker, M., and Chang, J. (2009). Stopping-Power & Range Tables for Electrons, Protons, and Helium Ions (version 1.2.3).

[Besemer et al., 2013] Besemer, A., Paganetti, H., and Bednarz, B. (2013). The clinical

impact of uncertainties in the mean excitation energy of human tissues during proton therapy. *Physics in Medicine and Biology*, 58(4):887–902.

[Bilski, 2012] Bilski, P. (2012). *Detektory termoluminescencyjne w pomiarach promieniowania kosmicznego i akceleratorowych wiązek jonów*. Rozprawa habilitacyjna, Institute of Nuclear Physics (IFJ PAN), Kraków.

[Böhlen et al., 2014] Böhlen, T. T., Cerutti, F., Chin, M. P. W., Fassò, A., Ferrari, A., Ortega, P. G., Mairani, A., Sala, P. R., Smirnov, G., and Vlachoudis, V. (2014). The FLUKA Code: Developments and Challenges for High Energy and Medical Applications. *Nuclear Data Sheets*, 120:211–214.

[Bonnett et al., 1993] Bonnett, D. E., Kacperek, A., Sheen, M. A., Goodall, R., and Saxton, T. E. (1993). The 62 MeV proton beam for the treatment of ocular melanoma at Clatterbridge. *The British Journal of Radiology*, 66(790):907–914.

[Bragg and Kleeman, 1905] Bragg, W. and Kleeman, R. (1905). XXXIX. On the alpha particles of radium, and their loss of range in passing through various atoms and molecules. *Philosophical Magazine*, 10(57):318–340.

[Bräuer-Krisch et al., 2010] Bräuer-Krisch, E., Serduc, R., Siegbahn, E. A., Le Duc, G., Prezado, Y., Bravin, A., Blattmann, H., and Laissue, J. A. (2010). Effects of pulsed, spatially fractionated, microscopic synchrotron X-ray beams on normal and tumoral brain tissue. *Mutation Research*, 704(1-3):160–166.

[CCB, 2014] CCB (2014). System terapii protonowej – Podręcznik użytkownika klinicznego dla IFJ PAN w Krakowie. Tom 1 Sesja terapeutyczna.

[CCB Quality Book, 2015] CCB Quality Book (2015). *KSIĘGA JAKOŚCI Dokument organizacji systemu zarządzania jakością Centrum Cyklotronowego Bronowice Instytutu Fizyki Jądrowej PAN w Krakowie według PN-EN ISO 9001:2009*. 1 edition.

[Cerutti et al., 2006] Cerutti, F., Battistoni, G., Capezzali, G., Colleoni, P., Ferrari, A., Gadioli, E., Mairani, A., and Pepe, A. (2006). Low energy nucleus-nucleus reactions: the BME approach and its interface with FLUKA 11th. In *Proceedings of 11th international conference on nuclear reaction mechanism*, pages pp 507–511, Varenna.

[Chu et al., 1993] Chu, W. T., Ludewigt, B. A., and Renner, T. R. (1993). Instrumentation for treatment of cancer using proton and light ion beams. *Review of Scientific Instruments*, 64(8):2055–2122.

[Cirrone et al., 2003] Cirrone, G. A. P., Cuttone, G., Guatelli, S., Nigro, S. L., Mascialino, B., Pia, M. G., Raffacle, L., Russo, G., and Sabini, M. G. (2003). Implementation of a new Monte Carlo simulation tool for the development of a proton therapy beam line and verification of the related dose distributions. In *2003 IEEE Nuclear Science Symposium. Conference Record (IEEE Cat. No.03CH37515)*, volume 3, pages 1756–1758 Vol.3.

[Cirrone et al., 2004] Cirrone, G. A. P., Cuttone, G., Lojacono, P. A., Nigro, S. L., Mongelli, V., Patti, I. V., Privitera, G., Raffaele, L., Rifuggiato, D., Sabini, M. G., et al. (2004). A 62-MeV proton beam for the treatment of ocular melanoma at Laboratori Nazionali del Sud-INFN. *IEEE Transactions on Nuclear Science*, 51(3):860–865.

[Clasie et al., 2012] Clasie, B., Depauw, N., Fransen, M., Gomà, C., Panahandeh, H. R., Seco, J., Flanz, J. B., and Kooy, H. M. (2012). Golden beam data for proton pencil-beam scanning. *Physics in Medicine and Biology*, 57(5):1147–1158.

[Daartz et al., 2009] Daartz, J., Bangert, M., Bussière, M. R., Engelsman, M., and Kooy, H. M. (2009). Characterization of a mini-multileaf collimator in a proton beamline. *Medical Physics*, 36(5):1886–1894.

[Daftari et al., 1996] Daftari, I. K., Renner, T. R., Verhey, L. J., Singh, R. P., Nyman, M., Petti, P. L., and Castro, J. R. (1996). New UCSF proton ocular beam facility at the

Crocker Nuclear Laboratory Cyclotron (UC Davis). *Nuclear Instruments and Methods in Physics Research Section A: Accelerators, Spectrometers, Detectors and Associated Equipment*, 380(3):597–612.

[Dosimetry, 2013] Dosimetry, I. (2013). Blue Phantom^2 User's Guide.

[Fano, 1954] Fano, U. (1954). Inelastic Collisions and the Moliere Theory of Multiple Scattering. *Phys.Rev.*, 93:117–120.

[Farah et al., 2015] Farah, J., Mares, V., Romero-Expósito, M., Trinkl, S., Domingo, C., Dufek, V., Klodowska, M., Kubancak, J., Knežević, Ž., Liszka, M., Majer, M., et al. (2015). Measurement of stray radiation within a scanning proton therapy facility: EURADOS WG9 intercomparison exercise of active dosimetry systems. *Medical Physics*, 42(5):2572–2584.

[Farr et al., 2013] Farr, J. B., Dessy, F., De Wilde, O., Bietzer, O., and Schönenberg, D. (2013). Fundamental radiological and geometric performance of two types of proton beam modulated discrete scanning systems. *Medical Physics*, 40(7):072101.

[Ferrari and Sala, 1998] Ferrari, A. and Sala, P. R. (1998). The physics of high energy reactions. *Proceedings of the workshop on nuclear reaction data and nuclear reactors. Physics, design and safety. In 2 volumes.*

[Ferrari and Sala, 2002] Ferrari, A. and Sala, P. R. (2002). Nuclear reactions in Monte Carlo codes. *Radiation Protection Dosimetry*, 99(1-4):29–38.

[Ferrari et al., 2011] Ferrari, A., Sala, P. R., Fassò, A., and Ranft, J. (2011). Fluka: a multi-particle transport code.

[Ferrari et al., 2005] Ferrari, A., Sala, P. R., Fasso, A., Ranft, J., Européenne, O., La, P., Nucléaire, R., Ferrari, A., Sala, P. R., Fassò, A., and Ranft, J. (2005). FLUKA: a multi-particle transport code. In *Cern 2005-10 (2005), Infn/Tc 05/11, Slac-R-773.*

[Fimel, 2015] Fimel (2015). User Manual Lynx PT.

[Fiorini et al., 2018] Fiorini, F., Schreuder, N., and Van den Heuvel, F. (2018). Technical Note: Defining cyclotron-based clinical scanning proton machines in a FLUKA Monte Carlo system. *Medical Physics*, 45(2):963–970.

[Fippel and Soukup, 2004] Fippel, M. and Soukup, M. (2004). A Monte Carlo dose calculation algorithm for proton therapy. *Medical Physics*, 31(8):2263–2273.

[Fuss et al., 2001] Fuss, M., Loredo, L. N., Blacharski, P. A., Grove, R. I., and Slater, J. D. (2001). Proton radiation therapy for medium and large choroidal melanoma: preservation of the eye and its functionality. *International Journal of Radiation Oncology*Biology*Physics*, 49(4):1053–1059.

[Gajewski, 2016] Gajewski, J. (2016). *Rozwój dwuwymiarowego, termoluminescencyjnego systemu dozymetrycznego dla zapewnienia jakości w jonoterapii nowotworów.* PhD Thesis, Institute of Nuclear Physics (IFJ PAN), Kraków.

[Gajewski et al., 2016] Gajewski, J., Kłosowski, M., and Olko, P. (2016). Two-dimensional thermoluminescence dosimetry system for proton beam quality assurance. *Radiation Measurements*, 90:224–227.

[Gillin et al., 2010] Gillin, M. T., Sahoo, N., Bues, M., Ciangaru, G., Sawakuchi, G., Poenisch, F., Arjomandy, B., Martin, C., Titt, U., Suzuki, K., et al. (2010). Commissioning of the discrete spot scanning proton beam delivery system at the University of Texas M.D. Anderson Cancer Center, Proton Therapy Center, Houston. *Medical Physics*, 37(1):154–163.

[Goitein and Miller, 1983] Goitein, M. and Miller, T. (1983). Planning proton therapy of the eye. *Medical Physics*, 10(3):275–283.

[Gottschalk, 2011] Gottschalk, B. (2011). Lectures (BGtalks.zip) and a draft textbook (PBS.pdf in BGdocs.zip) available for free download.

[Gottschalk et al., 2015] Gottschalk, B., Cascio, E. W., Daartz, J., and Wagner, M. S. (2015). On the nuclear halo of a proton pencil beam stopping in water. *Physics in Medicine & Biology*, 60(14):5627.

[Gottschalk et al., 1993] Gottschalk, B., Koehler, A. M., Schneider, R. J., Sisterson, J. M., and Wagner, M. S. (1993). Multiple Coulomb scattering of 160 MeV protons. *Nuclear Instruments and Methods in Physics Research Section B: Beam Interactions with Materials and Atoms*, 74(4):467–490.

[Gragoudas et al., 1977] Gragoudas, E. S., Goitein, M., Koehler, A. M., Verhey, L., Tepper, J., Suit, H. D., Brockhurst, R., and Constable, I. J. (1977). Proton irradiation of small choroidal malignant melanomas. *American Journal of Ophthalmology*, 83(5):665–673.

[Grassberger et al., 2015] Grassberger, C., Lomax, A., and Paganetti, H. (2015). Characterizing a proton beam scanning system for Monte Carlo dose calculation in patients. *Physics in Medicine and Biology*, 60(2):633–645.

[Grevillot et al., 2011] Grevillot, L., Bertrand, D., Dessy, F., Freud, N., and Sarrut, D. (2011). A Monte Carlo pencil beam scanning model for proton treatment plan simulation using GATE/GEANT4. *Physics in Medicine & Biology*, 56(16):5203.

[Grubbé, 1933] Grubbé, E. H. (1933). Priority in the Therapeutic Use of X-rays. *Radiology*, 21(2):156–162.

[Grusell et al., 1994] Grusell, E., Montelius, A., Brahme, A., Rikner, G., and Russell, K. (1994). A general solution to charged particle beam flattening using an optimized dual-scattering-foil technique, with application to proton therapy beams. *Physics in Medicine & Biology*, 39(12):2201.

[Haberer et al., 1993] Haberer, T., Becher, W., Schardt, D., and Kraft, G. (1993). Magnetic scanning system for heavy ion therapy. *Nuclear Instruments and Methods in Physics Research Section A: Accelerators, Spectrometers, Detectors and Associated Equipment*, 330(1):296–305.

[Haberer et al., 2004] Haberer, T. h., Debus, J., Eickhoff, H., Jäkel, O., Schulz-Ertner, D., and Weber, U. (2004). The Heidelberg Ion Therapy Center. *Radiotherapy and Oncology: Journal of the European Society for Therapeutic Radiology and Oncology*, 73 Suppl 2:S186–190.

[Haettner, 2006] Haettner, E. (2006). Experimental study on carbon ion fragmentation in water using GSI therapy beams. Master's thesis, KTH, Stockholm.

[Hara et al., 2012] Hara, Y., Takada, Y., Hotta, K., Tansho, R., Nihei, T., Suzuki, Y., Kosuke Nagafuchi, Kawai, R., Tanabe, M., et al. (2012). Improvement of spread-out Bragg peak flatness for a carbon-ion beam by the use of a ridge filter with a ripple filter. *Physics in Medicine & Biology*, 57(6):1717.

[Hérault et al., 2005] Hérault, J., Iborra, N., Serrano, B., and Chauvel, P. (2005). Monte Carlo simulation of a protontherapy platform devoted to ocular melanoma. *Medical Physics*, 32(4):910–919.

[Horwacik et al., 2016] Horwacik, T., Michalec, B., Grzanka, L., Durlak, E., Ogrodowicz, E., Nowak, T., Ptaszkiewicz, M., Kajdrowicz, T., Swakoń, J., and Olko, P. (2016). Commissioning of ELTR the new proton ocular facility at the IFJ PAN. In *Proceedings 55 th Annual Meeting of the Particle Therapy Cooperative Group (PTCOG)*, Prague.

[Hrbacek et al., 2016] Hrbacek, J., Mishra, K. K., Kacperek, A., Dendale, R., Nauraye, C., Auger, M., Herault, J., Daftari, I. K., Trofimov, A. V., Shih, H. A., et al. (2016). Practice

Patterns Analysis of Ocular Proton Therapy Centers: The International OPTIC Survey. *International Journal of Radiation Oncology, Biology, Physics*, 95(1):336–343.

[ICRU37, 1984] ICRU37 (1984). Stopping powers for electrons and positrons. Technical Report ICRU Report 37.

[ICRU49, 1993] ICRU49 (1993). Stopping-Power & Range Tables for Electrons, Protons, and Helium Ions. Technical Report ICRU Report 49.

[ICRU59, 1998] ICRU59 (1998). Clinical Proton Dosimetry Part I: Beam Production, Beam Delivery and Measurement of Absorbed Dose. Technical Report ICRU Report 59.

[ICRU78, 2007] ICRU78 (2007). Prescribing, recording, and reporting proton-beam therapy. Technical Report ICRU Report 78.

[ICRU90, 2014] ICRU90 (2014). Key Data For Ionizing-Radiation Dosimetry: Measurement Standards And Applications. Technical Report ICRU Report 90.

[Jan et al., 2011] Jan, S., Benoit, D., Becheva, E., Carlier, T., Cassol, F., Descourt, P., Frisson, T., Grevillot, L., Guigues, L., Maigne, L., et al. (2011). GATE V6: a major enhancement of the GATE simulation platform enabling modelling of CT and radiotherapy. *Physics in Medicine and Biology*, 56(4):881–901.

[Jan et al., 2004] Jan, S., Santin, G., Strul, D., Staelens, S., Assié, K., Autret, D., Avner, S., Barbier, R., Bardiès, M., Bloomfield, P. M., et al. (2004). GATE: a simulation toolkit for PET and SPECT. *Physics in Medicine & Biology*, 49(19):4543.

[Janni, 1982] Janni, J. F. (1982). Energy loss, range, path length, time-of-flight, straggling, multiple scattering, and nuclear interaction probability. *Atomic Data and Nuclear Data Tables*, 27(2):147–339.

[Jelen et al., 2014] Jelen, U., Radoń (Kłodowska), M., Santiago, A., Wittig, A., and Ammazzalorso, F. (2014). A Monte Carlo tool for raster-scanning particle therapy dose computation. *Journal of Physics: Conference Series*, 489:012013.

[Kacperek, 2009] Kacperek, A. (2009). Protontherapy of eye tumours in the UK: A review of treatment at Clatterbridge. *Applied Radiation and Isotopes*, 67(3):378–386.

[Kanai et al., 1997] Kanai, T., Furusawa, Y., Fukutsu, K., Itsukaichi, H., Eguchi-Kasai, K., and Ohara, H. (1997). Irradiation of Mixed Beam and Design of Spread-Out Bragg Peak for Heavy-Ion Radiotherapy. *Radiation Research*, 147(1):78–85.

[Kang and Kim, 2009] Kang, B. and Kim, J. (2009). Monte Carlo Design Study of a Gamma Detector System to Locate Distal Dose Falloff in Proton Therapy. *IEEE Transactions on Nuclear Science*, 56(1):46–50.

[Kimstrand et al., 2008] Kimstrand, P., Tilly, N., Ahnesjö, A., and Traneus, E. (2008). Experimental test of Monte Carlo proton transport at grazing incidence in GEANT4, FLUKA and MCNPX. *Physics in Medicine and Biology*, 53(4):1115–1129.

[Kłodowska et al., 2016] Kłodowska, M., Gajewski, J., Skowrońska, K., and Olko, P. (2016). Criteria of spot asymmetry in proton radiotherapy pencil beam scanning - a Monte Carlo study. *Radiotherapy and Oncology*, 118:S57–S58.

[Kłodowska et al., 2015] Kłodowska, M., Olko, P., and Waligórski, M. P. R. (2015). Proton microbeam radiotherapy with scanned pencil-beams–Monte Carlo simulations. *Physica medica: PM: an international journal devoted to the applications of physics to medicine and biology: official journal of the Italian Association of Biomedical Physics (AIFB)*, 31(6):621–626.

[Koehler et al., 1977] Koehler, A. M., Schneider, R. J., and Sisterson, J. M. (1977). Flattening of proton dose distributions for large-field radiotherapy. *Medical Physics*, 4(4):297–301.

[Kooy et al., 2010] Kooy, H. M., Clasie, B. M., Lu, H.-M., Madden, T. M., Bentefour, H., Depauw, N., Adams, J. A., Trofimov, A. V., Demaret, D., Delaney, T. F., and Flanz, J. B.

(2010). A Case Study in Proton Pencil-Beam Scanning Delivery. *International Journal of Radiation Oncology*Biology*Physics*, 76(2):624–630.

[Krämer et al., 2000] Krämer, M., Jäkel, O., Haberer, T., Kraft, G., Schardt, D., and Weber, U. (2000). Treatment planning for heavy-ion radiotherapy: physical beam model and dose optimization. *Physics in Medicine and Biology*, 45(11):3299–3317.

[Krzempek et al., 2016] Krzempek, D., Komenda, W., Mojżeszek, N., Gajewski, J., Kłodowska, M., Liszka, M., Pędracka, A., Stolarczyk, L., and Olko, P. (2016). Experimental characterization of proton pencil beam spot profiles including the lowdose envelope measurement. In *Proceedings 55 th Annual Meeting of the Particle Therapy Cooperative Group (PTCOG)*, Prague.

[Larsson, 1962] Larsson (1962). *Application of a 185 MeV proton beam to experimental cancer therapy and neurosurgery: A biophysical study.* PhD Thesis, University of Uppsala.

[Lin et al., 2014] Lin, L., Ainsley, C. G., Solberg, T. D., and McDonough, J. E. (2014). Experimental characterization of two-dimensional spot profiles for two proton pencil beam scanning nozzles. *Physics in Medicine and Biology*, 59(2):493–504.

[Linz (ed.) and Kacperek, 2012] Linz (ed.), U. and Kacperek, A. (2012). Chapter 10: Ocular Proton Therapy Centres. In *Ion Beam Therapy*, Biological and Medical Physics, Biomedical Engineering. Springer-Verlag, Berlin Heidelberg.

[Liszka et al., 2018] Liszka, M., Stolarczyk, L., Kłodowska, M., Kozera, A., Krzempek, D., Mojżeszek, N., Pędracka, A., Waligórski, M. P. R., and Olko, P. (2018). Ion recombination and polarity correction factors for a plane-parallel ionization chamber in a proton scanning beam. *Medical Physics*, 45(1):391–401.

[Lomax, 1999] Lomax, A. (1999). Intensity modulation methods for proton radiotherapy. *Physics in Medicine and Biology*, 44(1):185–205.

[Lomax et al., 2004] Lomax, A. J., Böhringer, T., Bolsi, A., Coray, D., Emert, F., Goitein, G., Jermann, M., Lin, S., Pedroni, E., Rutz, H., et al. (2004). Treatment planning and verification of proton therapy using spot scanning: initial experiences. *Medical Physics*, 31(11):3150–3157.

[Lomax et al., 1999] Lomax, A. J., Bortfeld, T., Goitein, G., Debus, J., Dykstra, C., Tercier, P.-A., Coucke, P. A., and Mirimanoff, R. O. (1999). A treatment planning inter-comparison of proton and intensity modulated photon radiotherapy. *Radiotherapy and Oncology*, 51(3):257–271.

[Mayles et al., 2007] Mayles, P., Nahum, A., Rosenwald, J. C., Nahum, A., and Rosenwald, J. C. (2007). *Handbook of Radiotherapy Physics : Theory and Practice.* CRC Press.

[Michalec et al., 2010] Michalec, B., Swakoń, J., Sowa, U., Ptaszkiewicz, M., Cywicka-Jakiel, T., and Olko, P. (2010). Proton radiotherapy facility for ocular tumors at the IFJ PAN in Kraków Poland. *Applied Radiation and Isotopes*, 68(4):738–742.

[Mirandola et al., 2015] Mirandola, A., Molinelli, S., Vilches Freixas, G., Mairani, A., Gallio, E., Panizza, D., Russo, S., Ciocca, M., Donetti, M., Magro, G., et al. (2015). Dosimetric commissioning and quality assurance of scanned ion beams at the Italian National Center for Oncological Hadrontherapy. *Medical Physics*, 42(9):5287–5300.

[Mojżeszek, 2018] Mojżeszek, N. (2018). *Dozymetria i kontrola jakości skanującej wiązki protonowej na stanowisku gantry.* PhD Thesis, Institute of Nuclear Physics (IFJ PAN), Kraków.

[Mojżeszek et al., 2017a] Mojżeszek, N., Farah, J., Kłodowska, M., Ploc, O., Stolarczyk, L., Waligórski, M. P. R., and Olko, P. (2017a). Measurement of stray neutron doses inside the treatment room from a proton pencil beam scanning system. *Physica medica: PM: an*

international journal devoted to the applications of physics to medicine and biology: official journal of the Italian Association of Biomedical Physics (AIFB), 34:80–84.

[Mojżeszek et al., 2017b] Mojżeszek, N., Kłodowska, M., Komenda, W., Stolarczyk, L., Kopeć, R., and Olko, P. (2017b). Geometrical efficiency of plane-parallel ionization chambers in proton scanning beam. *Radiation Protection Dosimetry*, pages 1–4.

[Molière, 1947] Molière, G. (1947). Theorie der Streuung schneller geladener Teilchen I. Einzelstreuung am abgeschirmten Coulomb-Feld. *Z.Naturforsch.*, A2:133–145.

[Molière, 1948] Molière, G. (1948). Theorie der Streuung schneller geladener Teilchen II. Mehrfach- und Vielfachstreuung. *Zeitschrift Naturforschung Teil A*, 3:78–97.

[Montelius et al., 1991] Montelius, A., Blomquist, E., Naeser, P., Brahme, A., Carlsson, J., Carlsson, A. C., Graffman, S., Grusell, E., Hallén, S., and Jakobsson, P. (1991). The narrow proton beam therapy unit at the the Svedberg Laboratory in Uppsala. *Acta Oncologica (Stockholm, Sweden)*, 30(6):739–745.

[Moyers et al., 1999] Moyers, M. F., Galindo, R. A., Yonemoto, L. T., Loredo, L., Friedrichsen, E. J., Kirby, M. A., Slater, J. D., and Slater, J. M. (1999). Treatment of macular degeneration with proton beams. *Medical Physics*, 26(5):777–782.

[Nauraye et al., 1995] Nauraye, C., Mazal, A., Delacroix, S., Bridier, A., Chavaudra, J., and Rosenwald, J. C. (1995). An experimental approach to the design of a scattering system for a proton therapy beam line dedicated to ophthalmological applications. *International Journal of Radiation Oncology, Biology, Physics*, 32(4):1177–1183.

[Newhauser and Zhang, 2015] Newhauser, W. D. and Zhang, R. (2015). The physics of proton therapy. *Physics in medicine and biology*, 60(8):R155–R209.

[Olko et al., 2006] Olko, P., Marczewska, B., Czopyk, L., Czermak, M. A., Klosowski, M., and Waligórski, M. P. R. (2006). New 2-D dosimetric technique for radiotherapy based on planar thermoluminescent detectors. *Radiation Protection Dosimetry*, 118(2):213–218.

[Paganetti, 2011] Paganetti, H. (2011). *Proton Therapy Physics*. Series in Medical Physics and Biomedical Engineering.

[Paganetti et al., 2004] Paganetti, H., Jiang, H., Lee, S. Y., and Kooy, H. M. (2004). Accurate Monte Carlo simulations for nozzle design, commissioning and quality assurance for a proton radiation therapy facility. *Medical Physics*, 31(7):2107–2118.

[Paganetti et al., 2002] Paganetti, H., Niemierko, A., Ancukiewicz, M., Gerweck, L. E., Goitein, M., Loeffler, J. S., and Suit, H. D. (2002). Relative biological effectiveness (RBE) values for proton beam therapy. *International Journal of Radiation Oncology, Biology, Physics*, 53(2):407–421.

[Parodi and Enghardt, 2000] Parodi, K. and Enghardt, W. (2000). Potential application of PET in quality assurance of proton therapy. *Physics in Medicine & Biology*, 45(11):N151.

[Parodi et al., 2007a] Parodi, K., Ferrari, A., Sommerer, F., and Paganetti, H. (2007a). Clinical CT-based calculations of dose and positron emitter distributions in proton therapy using the FLUKA Monte Carlo code. *Physics in medicine and biology*, 52(12):3369–3387.

[Parodi et al., 2012] Parodi, K., Mairani, A., Brons, S., Hasch, B. G., Sommerer, F., Naumann, J., Jäkel, O., Haberer, T., and Debus, J. (2012). Monte Carlo simulations to support start-up and treatment planning of scanned proton and carbon ion therapy at a synchrotron-based facility. *Physics in Medicine and Biology*, 57(12):3759–3784.

[Parodi et al., 2010] Parodi, K., Mairani, A., Brons, S., Naumann, J., Krämer, M., Sommerer, F., and Haberer, T. (2010). The influence of lateral beam profile modifications in scanned proton and carbon ion therapy: a Monte Carlo study. *Physics in Medicine and Biology*, 55(17):5169–5187.

[Parodi et al., 2007b] Parodi, K., Paganetti, H., Cascio, E., Flanz, J. B., Bonab, A. A.,

Alpert, N. M., Lohmann, K., and Bortfeld, T. (2007b). PET/CT imaging for treatment verification after proton therapy: a study with plastic phantoms and metallic implants. *Medical Physics*, 34(2):419–435.

[Paul, 2007a] Paul, H. (2007a). The mean ionization potential of water, and its connection to the range of energetic carbon ions in water. *Nuclear Instruments and Methods in Physics Research Section B: Beam Interactions with Materials and Atoms*, 255(2):435–437.

[Paul, 2007b] Paul, H. (2007b). New developments in stopping power for fast ions. *Nuclear Instruments and Methods in Physics Research Section B: Beam Interactions with Materials and Atoms*, 261(1):1176–1179.

[Pędracka et al., 2016] Pędracka, A., Stolarczyk, L., Liszka, M., Komenda, W., Sadowski, B., Skowrońska, K., and Olko, P. (2016). Dosimetric verification as a part of commissioning of treatment planning system in proton spot scanning pencil beam radiotherapy.

[Pedroni et al., 1995] Pedroni, E., Bacher, R., Blattmann, H., Böhringer, T., Coray, A., Lomax, A., Lin, S., Munkel, G., Scheib, S., and Schneider, U. (1995). The 200-MeV proton therapy project at the Paul Scherrer Institute: conceptual design and practical realization. *Medical Physics*, 22(1):37–53.

[Pedroni et al., 2005] Pedroni, E., Scheib, S., Böhringer, T., Coray, A., Grossmann, M., Lin, S., and Lomax, A. (2005). Experimental characterization and physical modelling of the dose distribution of scanned proton pencil beams. *Physics in Medicine and Biology*, 50(3):541–561.

[Pelowitz, 2011] Pelowitz, ed., D. (2011). MCNPX User's Manual.

[Perl et al., 2011] Perl, J., Schümann, J., Shin, J., Faddegon, B., and Paganetti, H. (2011). TOPAS: A Fast and Easy to Use Tool for Particle Simulation. *Medical Physics*, 38(6Part28):3754–3755.

[Pirruccello and Tobias, 1980] Pirruccello, M. C. and Tobias, C. A. (1980). Biological and medical research with accelerated heavy ions at the Bevalac, 1977-1980. Technical Report LBL–11220, California Univ.

[Prezado and Fois, 2013] Prezado, Y. and Fois, G. R. (2013). Proton-minibeam radiation therapy: A proof of concept. *Medical Physics*, 40(3).

[PTW, 2015] PTW (2015). User Manual RW3 Slab Phantom T29672 and T40006.1.001.

[Randeniya et al., 2009] Randeniya, S. D., Taddei, P. J., Newhauser, W. D., and Yepes, P. (2009). Intercomparision of Monte Carlo Radiation Transport Codes MCNPX, GEANT4, and FLUKA for Simulating Proton Radiotherapy of the Eye. *Nuclear Technology*, 168(3):810–814.

[Robert et al., 2013] Robert, C., Dedes, G., Battistoni, G., Böhlen, T. T., Buvat, I., Cerutti, F., Chin, M. P. W., Ferrari, A., Gueth, P., Kurz, C., et al. (2013). Distributions of secondary particles in proton and carbon-ion therapy: a comparison between GATE/Geant4 and FLUKA Monte Carlo codes. *Physics in Medicine and Biology*, 58(9):2879–2899.

[Romanowska-Dixon et al., 2012] Romanowska-Dixon, B., Pogrzebielski, A., Bogdali, A., Markiewicz, A., Swakoń, J., Olko, P., Jeżabek, M., Sas-Korczyńska, B., and Pluta, E. (2012). Radioterapia protonowa czerniaka błony naczyniowej - wstępne wyniki leczenia. , 114, 3, s. 173- 179. *Klin. Oczna.*

[Röntgen, 1895] Röntgen, W. C. (1895). Über Eine Neue Art von Strahlen. *Sitzungsberichte der Würzburger Physikalischmedicinischen Gesellschaft*, page 137:41.

[Ruciński et al., 2017] Ruciński, A., Gajewski, J., Olko, P., Rinaldi, I., Patera, V., and Schiavi, A. (2017). GPU-accelerated Monte Carlo code for fast dose recalculation in proton beam therapy. 48:1625–1630.

[Rydygier, 2016] Rydygier, M. (2016). *Wyznaczanie rozkładów przestrzennych fluencji*

protonowych wiązek terapeutycznych. PhD Thesis, Institute of Nuclear Physics (IFJ PAN), Kraków.

[Rydygier et al., 2015] Rydygier, M., Mierzwińska, G., Czaderna, A., Swakoń, J., and Waligórski, M. P. R. (2015). Studies of scintillator response to 60 MeV protons in a proton beam imaging system. *Nukleonika*, 60(3):683–687.

[Sawakuchi et al., 2010a] Sawakuchi, G. O., Mirkovic, D., Perles, L. A., Sahoo, N., Zhu, X. R., Ciangaru, G., Suzuki, K., Gillin, M. T., Mohan, R., and Titt, U. (2010a). An MCNPX Monte Carlo model of a discrete spot scanning proton beam therapy nozzle. *Medical Physics*, 37(9):4960–4970.

[Sawakuchi et al., 2010b] Sawakuchi, G. O., Titt, U., Mirkovic, D., Ciangaru, G., Zhu, X. R., Sahoo, N., Gillin, M. T., and Mohan, R. (2010b). Monte Carlo investigation of the low-dose envelope from scanned proton pencil beams. *Physics in Medicine and Biology*, 55(3):711–721.

[Schiavi et al., 2017] Schiavi, A., Senzacqua, M., Pioli, S., Mairani, A., Magro, G., Molinelli, S., Ciocca, M., Battistoni, G., and Patera, V. (2017). Fred: a GPU-accelerated fast-Monte Carlo code for rapid treatment plan recalculation in ion beam therapy. *Physics in Medicine and Biology*, 62(18):7482–7504.

[Schippers and Lomax, 2011] Schippers, J. M. and Lomax, A. J. (2011). Emerging technologies in proton therapy. *Acta Oncologica*, 50(6):838–850.

[Schneider et al., 2002] Schneider, U., Agosteo, S., Pedroni, E., and Besserer, J. (2002). Secondary neutron dose during proton therapy using spot scanning. *International Journal of Radiation Oncology*Biology*Physics*, 53(1):244–251.

[Schwaab et al., 2011] Schwaab, J., Brons, S., Fieres, J., and Parodi, K. (2011). Experimental characterization of lateral profiles of scanned proton and carbon ion pencil beams for improved beam models in ion therapy treatment planning. *Physics in Medicine and Biology*, 56(24):7813–7827.

[Seco and Verhaegen, 2016] Seco, J. and Verhaegen, F. (2016). *Monte Carlo Techniques in Radiation Therapy*. imaging in Medical Diagnosis and Therapy. CRC Press, 1st edition edition.

[Slopsema et al., 2013] Slopsema, R., Mamalui-Hunter, M., Yeung, D., and Li, Z. (2013). A commercial proton therapy system for the treatment of ocular lesions.

[Sommerer et al., 2006] Sommerer, F., Parodi, K., Ferrari, A., Poljanc, K., Enghardt, W., and Aiginger, H. (2006). Investigating the accuracy of the FLUKA code for transport of therapeutic ion beams in matter. *Physics in Medicine & Biology*, 51(17):4385.

[Sorge et al., 1989] Sorge, H., Stöcker, H., and Greiner, W. (1989). Relativistic quantum molecular dynamics approach to nuclear collisions at ultrarelativistic energies. *Nuclear Physics A*, 498:567–576.

[Stankovskiy et al., 2009] Stankovskiy, A., Kerhoas-Cavata, S., Ferrand, R., Nauraye, C., and Demarzi, L. (2009). Monte Carlo modelling of the treatment line of the Proton Therapy Center in Orsay. *Physics in Medicine and Biology*, 54(8):2377–2394.

[Stolarczyk et al., 2010] Stolarczyk, L., Olko, P., Cywicka-Jakiel, T., Ptaszkiewicz, M., Swakon, J., Dulny, B., Horwacik, T., Obryk, B., and Waligorski, M. P. R. (2010). Assessment of undesirable dose to eye-melanoma patients after proton radiotherapy. *Radiation Measurements*, 45(10):1441–1444.

[Stolarczyk et al., 2018] Stolarczyk, L., Trinkl, S., Romero-Expósito, M., Mojżeszek, N., Ambrozova, I., Domingo, C., Davídková, M., Farah, J., Kłodowska, M., Knežević, Ž., et al. (2018). Dose distribution of secondary radiation in a water phantom for a proton pen-

cil beam-EURADOS WG9 intercomparison exercise. *Physics in Medicine and Biology*, 63(8):085017.

[Strzałkowski et al., 2006] Strzałkowski, A. E., Bakewicz, E., and Taraszkiewicz, R. (2006). Historia krakowskich cyklotronów. In *Polscy twórcy aparatury naukowej. Monografie*. 10.Komisja Historii Nauki PAU.

[Suit et al., 2010] Suit, H., DeLaney, T., Goldberg, S., Paganetti, H., Clasie, B., Gerweck, L., Niemierko, A., Hall, E., Flanz, J., Hallman, J., and Trofimov, A. (2010). Proton vs carbon ion beams in the definitive radiation treatment of cancer patients. *Radiotherapy and Oncology: Journal of the European Society for Therapeutic Radiology and Oncology*, 95(1):3–22.

[Swakon et al., 2010] Swakon, J., Olko, P., Adamczyk, D., Cywicka-Jakiel, T., Dabrowska, J., Dulny, B., Grzanka, L., Horwacik, T., Kajdrowicz, T., Michalec, B., et al. (2010). Facility for proton radiotherapy of eye cancer at IFJ PAN in Krakow. *Radiation Measurements*, 45(10):1469–1471.

[Systems, 2013] Systems, V. M. (2013). Proton Algorithm Reference Guide Eclipse.

[Takada, 1994] Takada, Y. (1994). Dual-Ring Double Scattering Method for Proton Beam Spreading. *Japanese Journal of Applied Physics*, 33(1R):353.

[Tan et al., 2004] Tan, Z., Xia, Y., Zhao, M., Liu, X., Li, F., Huang, B., and Ji, Y. (2004). Electron stopping power and mean free path in organic compounds over the energy range of 20–10,000 eV. *Nuclear Instruments and Methods in Physics Research Section B: Beam Interactions with Materials and Atoms*, 222(1):27–43.

[Tobias et al., 1952] Tobias, C. A., Anger, H. O., and Lawrence, J. H. (1952). Radiological use of high energy deuterons and alpha particles. *The American Journal of Roentgenology, Radium Therapy, and Nuclear Medicine*, 67(1):1–27.

[Tobola-Galus et al., 2018] Tobola-Galus, A., Swakon, J., and Olko, P. (2018). Dosimetric characterization of collimators for spatially fractionated proton therapy of the eye. *Radiation Protection Dosimetry*, 180(1-4):351–354.

[TRS-398, 2001] TRS-398 (2001). Absorbed Dose Determination in External Beam Radiotherapy. (IAEA Report 398).

[TRS-430, 2004] TRS-430 (2004). Commissioning and Quality Assurance of Computerized Planning Systems for Radiation Treatment of Cancer. (IAEA Report 430).

[Ustaw, 2017] Ustaw, D. (2017). Obwieszczenie Ministra Zdrowia z dnia 3 kwietnia 2017 r. w sprawie ogłoszenia jednolitego tekstu rozporządzenia Ministra Zdrowia w sprawie warunków bezpiecznego stosowania promieniowania jonizującego dla wszystkich rodzajów ekspozycji medycznej.

[Vatnitsky et al., 1999] Vatnitsky, S. M., Miller, D. W., Moyers, M. F., Levy, R. P., Schulte, R. W., Slater, J. D., and Slater, J. M. (1999). Dosimetry techniques for narrow proton beam radiosurgery. *Physics in Medicine & Biology*, 44(11):2789.

[Vlachoudis, 2009] Vlachoudis, V. (2009). Flair: A powerful but user friendly graphical interface for FLUKA.

[Waters, 2002] Waters, l. (2002). MCNPX User's Manual.

[Wilson, 2004] Wilson, R. (2004). A Brief History of the Harvard University Cyclotrons — Richard Wilson | Harvard University Press.

[Wilson, 1946] Wilson, R. R. (1946). Radiological Use of Fast Protons. *Radiology*, 47(5):487–491.

[Zazula, 1990] Zazula, J. M. (1990). Implementation of a low energy neutron transport module into a Monte Carlo hadronic shower code and its applications for accelerator shielding problems. *Progress in Nuclear Energy*, 24(1):385–397.

[Zhang et al., 2011] Zhang, X., Liu, W., Li, Y., Li, X., Quan, M., Mohan, R., Anand, A., Sahoo, N., Gillin, M., and Zhu, X. R. (2011). Parameterization of multiple Bragg curves for scanning proton beams using simultaneous fitting of multiple curves. *Physics in Medicine and Biology*, 56(24):7725–7735.